

Three-color Multiparameter Fluorescence Detection with Pulsed Interleaved Excitation

Masterarbeit aus dem Fachgebiet

Physikalische Chemie

von

B.Sc. Anders Barth

geboren am 14.6.1988

in Bad Oldesloe

für die Masterprüfung in Chemie an der

Ludwig-Maximilians-Universität München

Datum der mündlichen Prüfung: 14.11.2012

Beginn der Masterarbeit: 9.1.2013

Masterarbeits beim Prüfungsausschuss eingereicht am: 9.9.2013

Erklärung

Ich versichere, dass ich die vorgelegte Masterarbeit am Department Chemie, Physikalische Chemie der Ludwig-Maximilians-Universität München unter der Anregung und Anleitung von Prof. Don C. Lamb selbständig durchgeführt und keine anderen als die angegebenen Hilfsmittel und Quellen benützt habe.

Der Betreuer dieser Abschlussarbeit darf - unter Angabe der Co-Autorenschaft des Verfassers der Masterarbeit - hieraus Daten verwenden und in wissenschaftlichen Zeitschriften veröffentlichen.

München, den 9.9.2013

Erstgutachter:	Prof. Don C. Lamb
Zweitgutachter:	Prof. Jens Michaelis

Contents

1	Introduction	8
1.1	Single-Molecule Fluorescence Spectroscopy	8
1.2	Multiparameter Fluorescence Detection and Burst Analysis	8
1.3	Multicolor Fluorescence Studies	8
1.4	Advantages of three-color FRET	10
1.5	Advancements and new concepts for quantitative multi-color FRET	12
2	Theory	13
2.1	Fluorescence	13
2.2	Förster Resonance Energy Transfer	16
2.3	Fluorescence Anisotropy	19
2.4	Accurate FRET efficiencies from three-color MFD-PIE data	21
3	Materials and Methods	25
3.1	Experimental Setup	25
3.2	Confocal Microscopy	28
3.3	Fluorescent dyes	29
3.4	Detectors	31
3.5	DNA molecules	32
3.6	Pulsed interleaved excitation	33
3.7	Burst Analysis	35
3.8	Data Analysis	37
3.8.1	The Efficiency-Stoichiometry plot in two-color PIE-MFD	37
3.8.2	Calculation of burstwise fluorescence parameters	38
3.8.3	Separating Subspecies	45
3.8.4	Data filtering	46
3.9	Simulation of multicolor FRET	51
3.10	Background in fluorescence measurements	52
3.10.1	Raman scattering	53
3.10.2	Removal of Raman background	55
4	Results	58
4.1	Duty-cycle optimized PIE (DCO-PIE)	58
4.1.1	Considerations when applying duty-cycle optimized pulse sequences	59
4.1.2	Effect of duty-cycle optimization in burst analysis	63
4.1.3	Realization of optimized pulse sequences	64
4.2	Two case studies: DNA measurements	67
4.2.1	Stepwise three-color FRET	67

4.2.2	Full three-color FRET	72
4.3	Three-color FRET study of the Hsp70 chaperone BiP	75
4.3.1	Specific labeling via unnatural amino acids	76
4.3.2	Comparison of efficiencies from three-color FRET with spFRET	76
4.3.3	Correlated motion in BiP	80
4.3.4	The conformational space of BiP	83
5	Conclusion and Outlook	85
5.1	Three-color MFD studies	85
5.2	Duty-cycle optimized PIE	86
5.3	Accurate Distance Measurements by three-color MFD	86
5.4	Refinement of the burstwise lifetime fitting	87
5.5	Dye choices for three-color FRET	88
5.6	Extension to four colors	91
A	Appendix	95
A.1	Useful relations of FRET related quantities	95
A.2	Correction factors for three-color PIE-MFD	96
A.2.1	Direct excitation and crosstalk	96
A.2.2	Correction factors for the presented measurements	97
A.3	Two-dimensional PDA	97
	References	99

List of Figures

1.1	Applications for three-color FRET	10
1.2	Uncoordinated and coordinated motion	11
2.1	Jablonski scheme for a single fluorophore	13
2.2	Frank-Condon principle	15
2.3	Jablonski scheme for the FRET process	16
2.4	Distance dependence of the FRET efficiency	17
2.5	Illustration of the overlap integral	18
2.6	Relative orientation of the fluorophores and the orientational factor κ^2	19
2.7	Three-color FRET scheme	21
3.1	Scheme of the experimental setup	25
3.2	Electronic triggering scheme	27
3.3	The confocal principle	28
3.4	Absorption spectra of the dyes	30
3.5	Emission spectra of the dyes and transmission of the used filters	30

3.6	Detection efficiencies of the detectors	31
3.7	Sequences of the DNA molecules	32
3.8	Pulsed-interleaved excitation	33
3.9	Experimental realization of PIE	34
3.10	Trace of a three-color burst measurement and burst size distribution	35
3.11	2D histogram of stoichiometry versus FRET efficiency	37
3.12	Stoichiometry-stoichiometry plots	45
3.13	Illustration of data filtering methods for two-color MFD	48
3.14	Illustration of data filtering methods for three-color MFD	49
3.15	Time traces of three-color burst measurements with and without Raman background	52
3.16	Raman spectrum of water	53
3.17	Microtime gating to remove the Raman background	54
3.18	Theoretical decay of the FRET signal	55
3.19	Emission spectra of Atto565 and Atto647N with different emission filters	56
4.1	Duty-cycle optimized pulse sequences	58
4.2	Gain in the blue channel for optimized pulse sequences	59
4.3	Loss in the red channel for optimized pulse sequences	60
4.4	Performance of duty-cycle optimized pulse sequences	61
4.5	Effect of duty-cycle optimization in burst analysis	63
4.6	Experimental realization of duty-cycle optimized pulse sequences	64
4.7	Gain of duty-cycle optimization by increase of the TAC range	66
4.8	Scheme of the cascade DNA	67
4.9	Two-dimensional stoichiometry and efficiency plots for the cascade dye arrangement.	68
4.10	One-dimensional parameter distributions for the cascade dye arrangement.	70
4.11	Scheme of the full three-color FRET DNA	72
4.12	Two-dimensional stoichiometry and efficiency plots for the full three-color FRET dye arrangement.	73
4.13	One-dimensional parameter distributions for the cascade dye arrangement.	74
4.14	Labeling positions within BiP for three-color FRET measurements	75
4.15	FRET analysis of BiP in the absence of nucleotides	77
4.16	FRET analysis of BiP in the presence of ADP	78
4.17	FRET analysis of BiP in the presence of AMP-PNP	79
4.18	Two-dimensional efficiency plots for BiP in the apo-state	80
4.19	Two-dimensional efficiency plots for BiP in the ADP-state	81
4.20	Two-dimensional efficiency plots for BiP in the ATP-state	82
4.21	Two-dimensional efficiency histograms of E_{BG} versus E_{GR} for the the apo-, ADP- and ATP-state of BiP	84

4.22	Comparison of the ADP- and ATP-state of BiP	84
5.1	Applications for four-color FRET	91
5.2	Absorption and emission spectra of near-infrared dyes	93

List of Tables

3.1	List of the fluorescent properties of the used dyes	29
3.2	List of stoichiometry values	46
3.3	Raman scattering for different excitation wavelengths	54
5.1	Comparison of blue fluorophores	89
5.2	Properties of near-infrared dyes	94
A.1	Correction factors used in this work	97

Abstract

Single-pair FRET (spFRET) has become a standard tool to monitor conformational changes in biomolecules in vitro. In solution based burst analysis, the burst of photons emanating from molecules diffusing through the confocal volume gives access to the underlying distribution of the FRET efficiency and other parameters of interest. Extension of spFRET with multiparameter fluorescence detection (MFD) to more colors enables the simultaneous observation of multiple distances. While several three or four color studies have already been performed, quantitative analysis of multicolor single molecule data remains a challenge. Specific labeling of proteins with three or more dyes requires the introduction of unnatural amino acids. Instrumentally, the emission of the different fluorescent dyes has to be detected efficiently while also minimizing spectral crosstalk. This necessitates careful selection of dyes, excitation wavelengths and emission filters. Moreover, Raman scattering may cause significant background signal levels. In addition to the experimental difficulties, the increased complexity of the multicolor FRET system and multiple dimensions measured leads to severe shot-noise broadening of the measured spectra. To maintain high accuracy with this increased complexity, the excitation pulse sequence has been optimized to spend more time probing the donor fluorophores.

To demonstrate the capabilities of three-color PIE-MFD, measurements of two types of dye arrangements on double stranded DNA molecules are presented. Specific labeling of the Hsp70 chaperone BiP has been achieved. FRET efficiencies from three-color measurements of BiP are compared to published results and correlated motions within the protein are elucidated.

1 Introduction

1.1 Single-Molecule Fluorescence Spectroscopy

Fluorescence spectroscopy is a widely applied method in biochemical and biological research. The study of structure, dynamics and interactions of biomolecules is enabled by covalent linking of fluorescent probes. A multitude of fluorescence based approaches have been applied to obtain information about biomolecules in their natural environment. Diffusion and interactions can be studied by fluorescence correlation spectroscopy (FCS, Magde et al., 1972). Fluorescence resonance energy transfer (FRET, Förster, 1948) provides the possibility to measure distances in the range of 2-10 nm via the efficiency of energy transfer between two fluorophores. The anisotropy and fluorescence lifetime can be exploited to study interactions between biomolecules. Observation of single molecules in combination with FRET allows the study of the static and dynamic heterogeneity of biological systems in real time. Single-pair FRET (spFRET) measurements can be performed on freely diffusing molecules in solution or on surface-immobilized molecules (Zander et al., 1996; Ha et al., 1996).

1.2 Multiparameter Fluorescence Detection and Burst Analysis

Identification of single molecules in solution is achieved by combination of the femtoliter sized focal volume of a confocal microscope with picomolar concentrations of the labeled molecule. Bursts of fluorescence are recorded for molecules diffusing through the focus. Multiparameter Fluorescence Detection (MFD), combined with Pulsed-interleaved Excitation (PIE), maximizes the informational content available from the single-molecule events (Widengren et al., 2006; Kudryavtsev et al., 2012). Detected photons are not only split by color, but also by polarization, and their arrival times are measured with picosecond accuracy by time-correlated single photon counting (TCSPC). Every detected photon is characterized by spectral range (color), polarization, macro- and microtime, and excitation source. Based on these information, derived parameters can be calculated: The color information grants access to the FRET efficiency, the polarization information is used to calculate the anisotropy and the timing resolution is used to determine fluorescence lifetimes.

1.3 Multicolor Fluorescence Studies

Single-molecule FRET is a long established method (Ha et al., 1996). The first three-color FRET studies were performed on the ensemble level (Liu and Lu, 2002; Watrob et al., 2003; Ramirez-Carrozzi and Kerppola, 2001; Galperin et al., 2004; Haustein et al., 2003). The initial appeal of three-color FRET was the possibility to increase the accessible range of FRET (Haustein et al., 2003; Heilemann et al., 2004). The first single molecule three-color FRET study was performed by Hohng et al. (2004) using confocal microscopy of immobilized molecules,

studying the correlated motions of a 4-way DNA Holliday junction. A first solution based study was performed by Clamme and Deniz (2005), proving the ability to resolve different subpopulations in a mixture of triple-labeled DNA molecules. Accurate description of the three-color FRET system is dependent on additional information about the spFRET subsystem, which is available via application of Pulsed-interleaved Excitation (PIE, Müller et al., 2005) or Alternating Laser Excitation (ALEX, Kapanidis et al., 2004, 2005). Extension of ALEX for three-color FRET was performed by Lee et al. (2007), showcasing the possibility to sort DNA species based on labeling stoichiometries and to resolve structural heterogeneity by means of three-dimensional FRET efficiency histograms. Furthermore, the translocation of a protein on a DNA molecule was observed from two positions at once. Three-color single molecule FRET with ALEX on immobilized molecules has since been realized by Ross et al. (2007), Person et al. (2009) and Lee et al. (2010b). Further advancement to four colors was achieved by Lee et al. (2010a) and Stein et al. (2011) for both confocal and total internal reflection microscopy (TIRF). Solution-based multicolor studies were performed by Ernst et al. (2012b), studying the rotation of the F_0F_1 -ATP synthase, and by Milles et al. (2012a), presenting the first intramolecular three-color FRET study of a protein and applying novel labeling methods to ensure specific labeling.

1.4 Advantages of three-color FRET

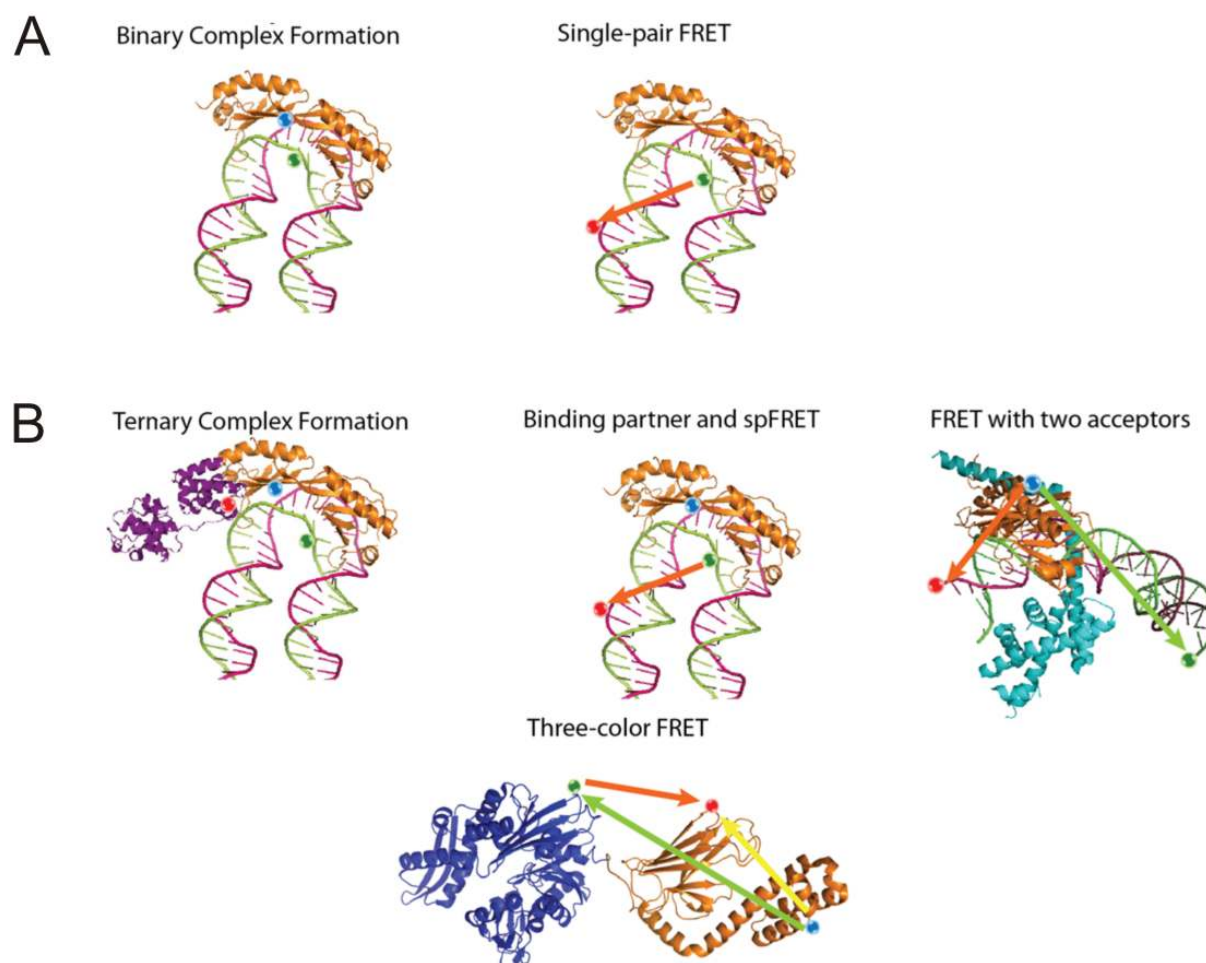


Figure 1.1: Possible application for A) two-color and B) three-color fluorescence spectroscopy. Figure provided by Don Lamb.

Two-color FRET has been used to great success in the past both in fluorescence correlation spectroscopy (FCS) studies and single molecule analysis. Its application is however limited to study binary complex formation e.g. by means of fluorescence cross-correlation spectroscopy (FCCS) or to monitor a single distance within a molecule (figure 1.1, A). Three-color FRET (figure 1.1, B) extends this approach elegantly by monitoring three distances simultaneously. Beyond the obvious capability to study ternary complex formation (Heinze et al., 2004), three-color FRET also enables one to correlate distance changes using spFRET with the presence or absence of binding partners. Obviously, also the simpler approach of monitoring two distances at once is feasible. This can be realized either by using one donor dye with two acceptors (Lee et al., 2010b), or by combining two donor dyes with one acceptor (Milles et al., 2012a). In the first case, the signal of the acceptors can be used as a measure for the proximity of the donor. The second case offers the signal of either donor to measure the two distances. Moreover, using a step-wise arrangement, it is possible to extend the distance range for FRET measurements beyond 10 nm using a mediator dye inbetween (Haustein et al., 2003; Watrob et al., 2003).

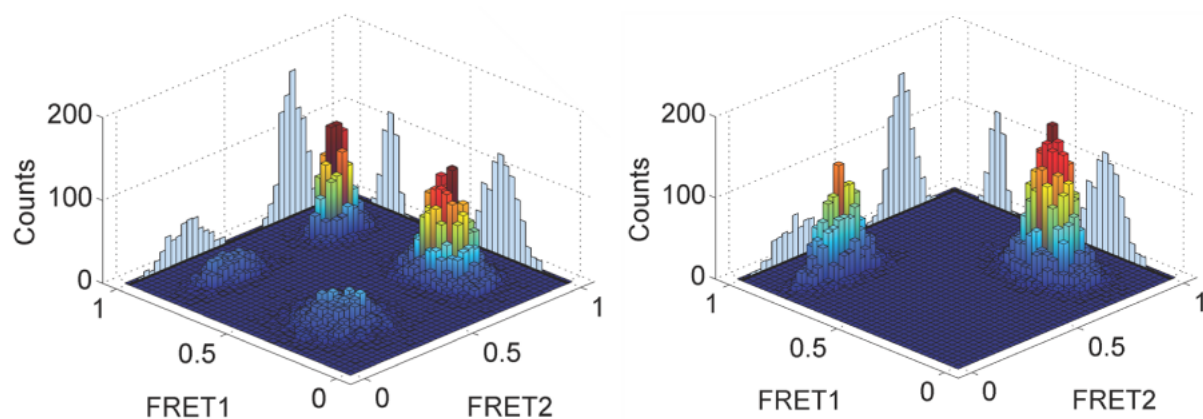


Figure 1.2: Uncoordinated motion versus coordinated motion. The projections, as measured in spFRET, fail to distinguish the two scenarios, while three-color FRET resolves the underlying correlation of the observed states. Figure provided by Don Lamb.

FCS has also recently been extended to three-colors to study multipartner complex formation in more detail (Wobma et al., 2012). A similar approach to monitor multiple distances within a single molecule at once is realized in switchable FRET (Uphoff et al., 2010), where the blinking of multiple acceptors with a single donor is exploited.

The advantage that three-color FRET excels at monitoring multiple distances is somewhat weakened by the notion that in principle spFRET is also capable of doing this, albeit in separate measurements. This approach works well for simple systems. If, however, multiple moving parts are involved, it is not possible to correlate the movements and it is thus not possible to distinguish whether or not movements are coordinated or uncoordinated. Consider the following case: A protein consists of a body and two flexible domains. Single-pair FRET measurements monitor the two domain-body distances separately, and two states are found for either domain, a closed state and an open state (see figure 1.2, one-dimensional projections). What spFRET fails to reveal is whether the domains move cooperatively or not, that is: Does the position of the first domain correlate to the position of the second domain? Identical one-dimensional histograms are obtained for both cases. In three-color FRET, both distances are measured simultaneously, and the question can be answered. Looking at the two-dimensional distance distributions, a total of four states are expected for uncorrelated motion, while correlated motion would only result in two states.

1.5 Advancements and new concepts for quantitative multi-color FRET

Four factors have hampered the widespread application of multi-color FRET.

- Analysis: The increasing complexity of the multi-color systems makes quantitative analysis challenging.
- Sample preparation: Specific labeling of proteins with three different dyes remains a challenge, which is why nearly all reported multi-color studies so far were applied to DNA systems.
- Background and corrections: For multi-color excitation, Raman background limits the spectral range available for fluorescence detection.
- Shot-noise: For multi-color FRET the signal intensity is distributed to three or more channels, severely limiting the number of photons per channel and increasing shot-noise in the measured parameter distributions. Instrumentally, the photon yield is limited by the choice of the objective, filters and detectors.

In this work, two new instrumental advancements have been applied: A 1.27 NA 60x water immersion objective has been used and single photon detection in the blue channels was performed by optimized avalanche photo diodes for the specific spectral range. Furthermore, the excitation pulse sequence is optimized to spend more time exciting the donor dye (duty-cycle optimized PIE, DCO-PIE). The idea of duty-cycle optimized excitation was introduced by Zarrabi et al. (2009) for alternating laser excitation (DCO-ALEX) and applied to three-color FRET measurements of the F_0F_1 -ATP synthase.

2 Theory

2.1 Fluorescence

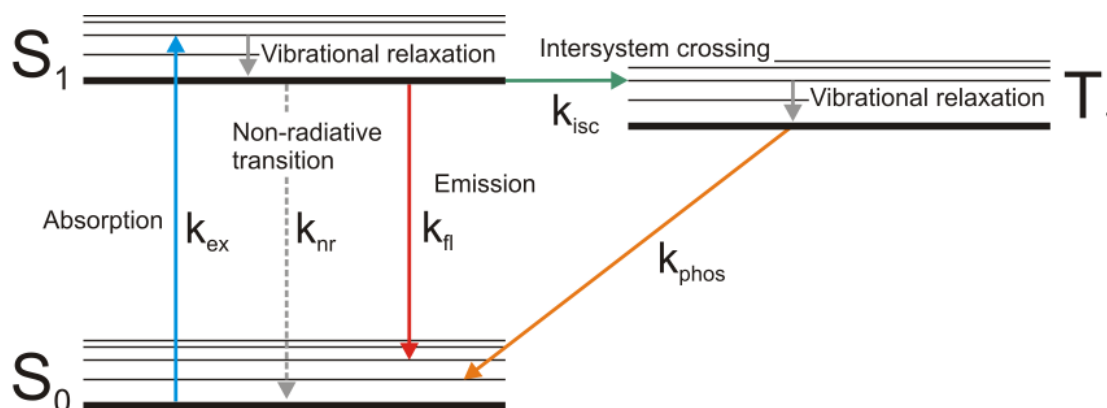


Figure 2.1: Jablonski scheme of a three state system consisting of the ground singlet state, the first excited state and a triplet state.

Fluorescence is the emission of a photon by a molecule after the molecule has been excited by the absorption of a photon. To describe the photophysics of fluorescence, a two-state model is assumed, consisting of a ground state, denoted as S_0 , and a first excited state S_1 (figure 2.1). Because the transition is spin allowed, both states are singlet (hence S). The molecule is excited by incident photons with rate k_{ex} . From S_1 the molecule can either relax by emitting a photon with rate k_{fl} (fluorescence) or relax non-radiatively by dissipating the energy into the solvent with rate k_{nr} . This simple model allows the explanation of two important properties of dyes: the quantum yield Φ , which is the efficiency of energy conversion from excitation to emission of a photon, and the lifetime τ , which is the mean time the fluorophore spends in the excited state. The quantum yield is defined by:

$$\Phi = \frac{k_r}{k_r + k_{nr}} \quad (2.1)$$

The decay of the first excited state, and thus the decay of the fluorescence intensity, is given by:

$$S_1(t) = S_1(0)e^{-t/\tau} \quad (2.2)$$

where:

$$\tau = (k_r + k_{nr})^{-1} \quad (2.3)$$

Quantum yield and lifetime are thus related:

$$\Phi = \frac{\tau}{\Gamma} \quad (2.4)$$

Here, $\Gamma = k_r^{-1}$ is the intrinsic radiative lifetime of the fluorophore.

Additional transitions have to be included for a complete treatment of the photophysical system. Firstly, higher excited states of the dye should be considered. Secondly, a spin forbidden transition to a triplet state is possible from the first excited state via spin conversion (intersystem crossing). Corresponding to the forbidden nature of the transition, the rates associated are lower than for fluorescence. Typical lifetimes for triplet states are of the order of microseconds. The rescue from a triplet state occurs by relaxation of the T_1 state by emission of a photon (phosphorescence) or by interaction with a triplet quencher.

The quantum mechanical description of the dye system uncouples electronic energy levels from vibronic and rotational energy levels, arguing that the movements of the electrons which define the electronic state of the molecule are much faster than the vibrational movements of the nuclei and certainly than rotational movements of the whole molecule (Born-Oppenheimer approximation). Extending this thought to electronic transitions the idea is that the change of the electronic structure is almost instantaneous, while the reorganization of the nuclei positions lags behind. In essence, upon excitation the electronic state of the molecule changes, while the vibronic state remains unchanged (Frank-Condon principle, see figure 2.2, left). What does this imply for fluorescence? Upon absorption of a photon, the molecule gains a discrete amount of energy. If this energy corresponds to the energy difference between the ground state configuration (S_0V_0 , where V denotes the vibronic state) and an excited state configuration S_1V_n , the photon can be absorbed. The probability of absorption is then given by the similarity of the vibronic states (or more technically, by the overlap integral of the vibronic wave functions). As every electronic state has its own set of vibronic sub-states, the transition usually does not occur to the vibronic ground state of the first excited state, but to a higher vibronic state. Subsequent relaxation to the vibronic ground state of the first excited electronic state occurs on the timescale of picoseconds. It is this energy loss which causes the red shift of the emitted light (Stokes shift). The transition back to the ground state is described analogously. The molecule relaxes to an excited vibronic state of the ground state, and the probability of the transition is again given by the overlap of the vibronic wave functions. Since the vibronic states of the ground state and the first excited state are usually very similar, absorption and emission spectra usually look very similar but are mirrored (mirror-image rule, see figure 2.2, right). Another property is that the emission spectrum is independent of the excitation wavelength, since all fluorescent transitions occur from the lowest vibrational level of the excited state (Kasha's rule).

There are three types of spectra to describe the fluorescent properties of a dye, two of which have already been discussed. The absorption spectrum is obtained by varying the excitation wavelength and measuring the loss in intensity of the excitation light. The fluorescence or emission spectrum is obtained by scanning the emission intensities at different wavelengths

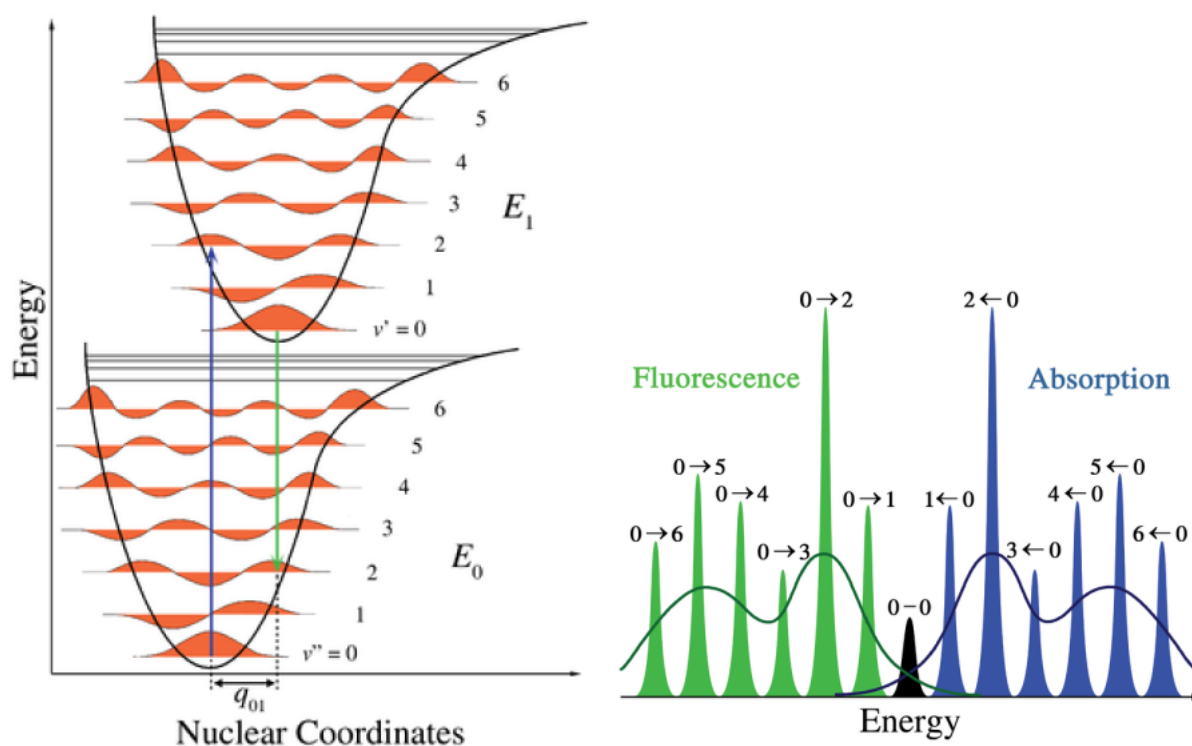


Figure 2.2: (Left) Illustration of the Frank-Condon principle. The potential energy curves of the ground and excited states are approximated by a Morse potential. For every discrete vibronic state the corresponding wave function is shown. The most probable transitions are indicated by arrows. (Right) Schematic of the absorption and fluorescence spectra. Discrete lines are observed for gases, whereas in solution inhomogeneous broadening occurs (black line). Adapted from Wikipedia (2013).

while keeping the excitation wavelength constant. The excitation spectrum can be measured by detecting the fluorescence in a fixed spectral region and altering of the excitation wavelengths.

Fluorescent dyes

There are three types of fluorescent probes used for fluorescence applications. Organic fluorophores are constituted of a large π -electron system. A multitude of different dyes spanning the visible and near-IR spectrum are available, based on different organic frameworks. The dyes can be covalently linked to proteins or nucleic acids via different functional groups. A second fluorescent probe, inorganic quantum dots, has excellent fluorescent properties, but they are usually large and heavy and thus not ideal for sensitive applications. The third class of fluorophores are fluorescent proteins, which are an excellent choice for fluorescence measurements in cells as they can be fused to the protein of interest. Expression of the fusion construct is achieved by transfecting cells with engineered bacterial plasmids. They do however usually exhibit frequent blinking and are not very photostable, and can influence protein function due to their size.

Photophysics and photochemistry of fluorophores

Organic fluorophores or fluorescent proteins exhibit a number of undesired properties. Photobleaching is the irreversible loss of fluorescence by chemical alteration of the fluorophore structure and occurs from higher excited states. The photostability depends on the applied laser power, the solvent and the local environment of the fluorophore. The population of triplet states has already been discussed. The lifetime of these dark states (μs to ms) is dependent on the availability of triplet quenchers. The presence of oxygen in solution experiments helps to quickly revert the fluorophore back to its ground state. However, the population of dark states remains the main contributor to signal saturation. Additionally, photochemical reactions from the triplet state can lead to even longer dark states ($>\text{ms}$). This blinking of fluorescent dyes is again dependent on the local environment. All of the listed processes limit the achievable observation time for single fluorophores.

2.2 Förster Resonance Energy Transfer

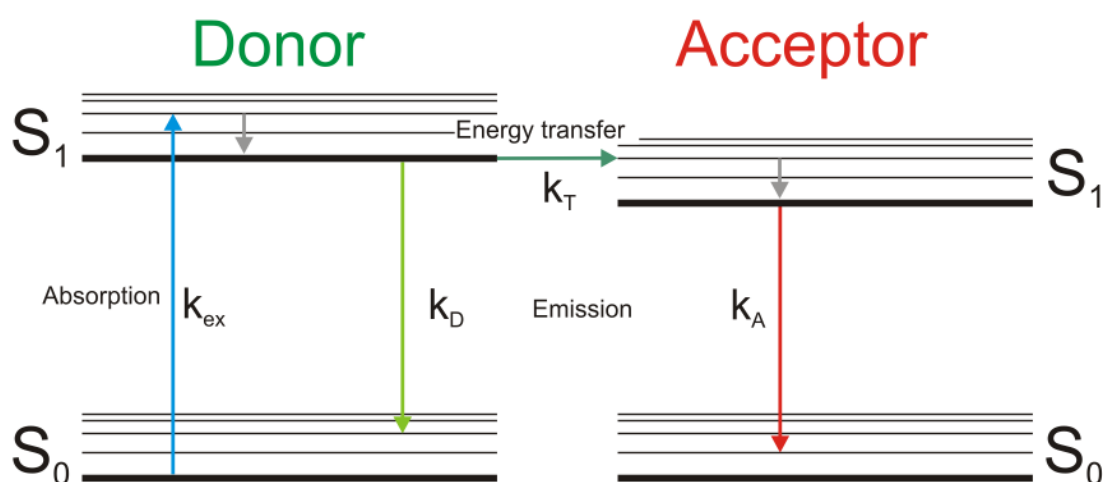


Figure 2.3: Jablonski diagram for the FRET process. k_{ex} : excitation rate; k_D , k_A : rates of fluorescence, k_T : rate of energy transfer.

Förster resonance energy transfer (or sometimes called fluorescence resonance energy transfer or simply resonance energy transfer, RET) is usually classically described by long range dipole-dipole interaction as developed by Förster (1948). The energy transfer occurs from the excited state of a donor molecule D to an acceptor molecule A in the ground state, that is hereby excited (see figure 2.3). It is important to note that this process does not involve emission and reabsorption of a photon. The efficiency of the energy transfer is dependent on the quantum yield of the donor, the spectral overlap between the emission spectrum of the donor and the absorption spectrum of the acceptor and the relative orientation of the donor and acceptor transition dipoles as well as their distance. The rate of transfer k_T is given by:

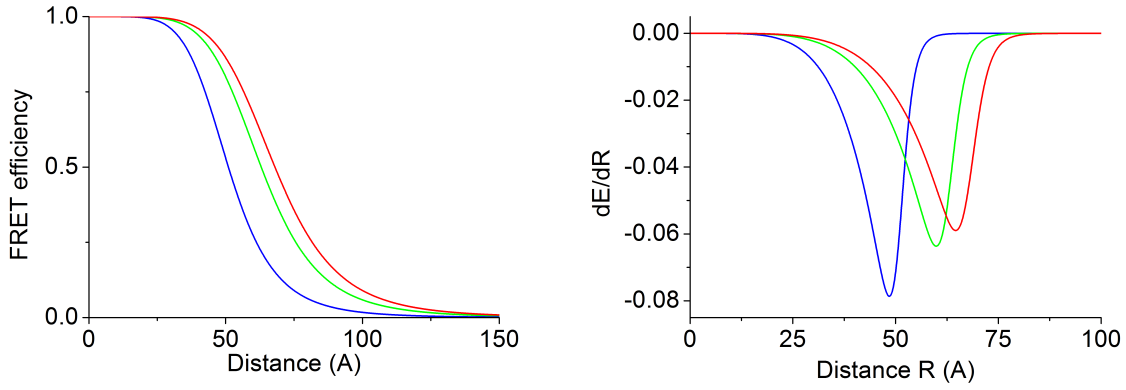


Figure 2.4: Dependence of the FRET efficiency on the interdye distance given in units of the Förster radius. The three curves correspond to the dye pairs used in this work with Förster radii of 51 Å (Atto488-Atto647N, blue), 63 Å (Atto488-Atto565, green), 68 Å (Atto565-Atto647N, red).

$$k_T = \frac{1}{\tau_D} \left(\frac{R_0}{R} \right)^6 \quad (2.5)$$

Here, τ_D is the lifetime of the donor in the absence of the acceptor, R is the interdye distance and R_0 is the Förster radius that combines the factors determining the transfer rate:

$$R_0^6 = \frac{9000 (\ln 10)}{128 \pi^5 N_A n^4} J \kappa^2 Q_D \quad (2.6)$$

N_A is Avogadro's number, n is the refractive index of the medium, κ^2 is a factor describing the relative orientation of the fluorophores, Q_D is the donor quantum yield and $J(\lambda)$ is the overlap integral given by:

$$J = \int_0^\infty F_D(\lambda) \epsilon_A(\lambda) \lambda^4 d\lambda \quad (2.7)$$

where $F_D(\lambda)$ is the area normalized emission spectrum of the donor and $\epsilon_A(\lambda)$ is the absorption spectrum of the acceptor in units of $\text{M}^{-1}\text{cm}^{-1}$ (see figure 2.5 for a visualization of J). κ^2 is dependent on the angle of the donor and acceptor transition dipoles relative to each other (θ_T) and the angles of the donor and acceptor dipoles relative to the distance vector (θ_D and θ_A), as seen in figure 2.6:

$$\kappa^2 = (\cos \theta_T - 3 \cos \theta_D \cos \theta_A)^2 \quad (2.8)$$

For most applications, κ^2 can be assumed to be $2/3$, if sufficient rotational averaging of the relative dye positions occurs within the donor lifetime.

To calculate the efficiency of the energy transfer, the rate of energy transfer is related to the competing pathways of relaxation of the excited donor dye, that is fluorescence and non-radiative transitions. The FRET efficiency E is then given by:

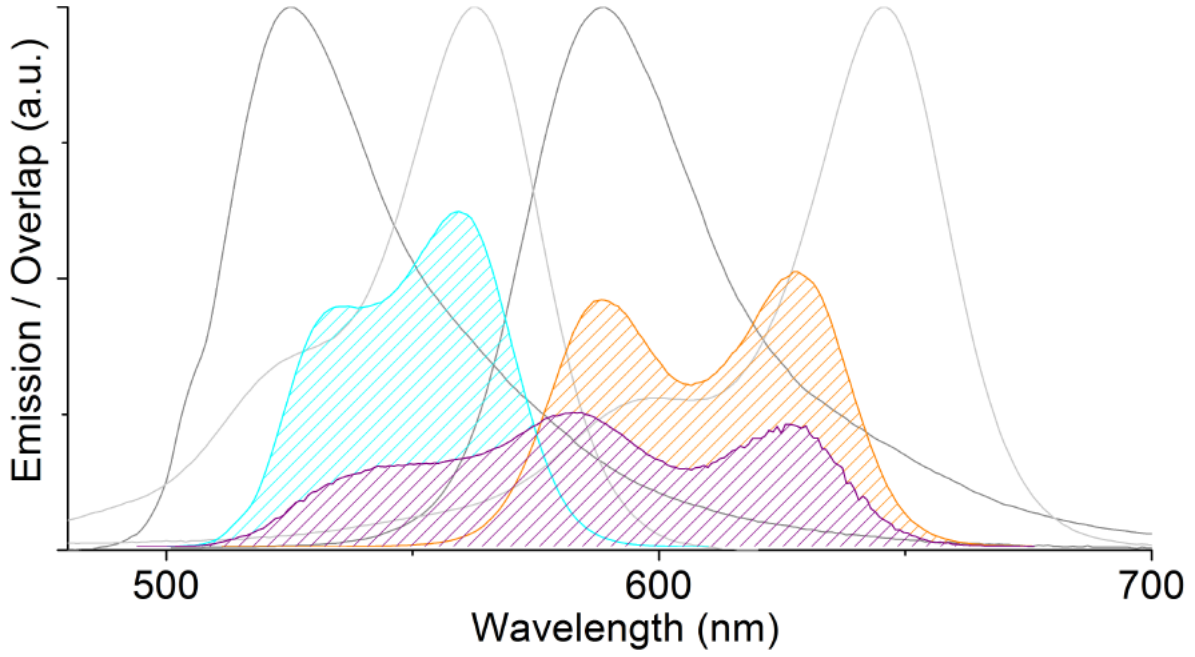


Figure 2.5: Overlap between the absorption and emission spectra of the different dye combinations (Atto488-Atto565: cyan, Atto488-Atto647N: purple, Atto565-Atto647N: orange). The shaded areas are proportional to the respective Förster radii. Additionally, absorption spectra of Atto565 and Atto647N are plotted in dark gray, and emission spectra of Atto488 and Atto565 are plotted in light gray.

$$E = \frac{k_T}{k_T + k_{fl} + k_{nr}} = \frac{k_T}{k_T + \tau_D^{-1}} \quad (2.9)$$

Thus, the distance dependence of E is given by:

$$E(R) = \frac{R_0^6}{R_0^6 + R^6} = \frac{1}{1 + \left(\frac{R}{R_0}\right)^6} \quad (2.10)$$

This relation is shown in figure 2.4. A consequence of the dependence of the transfer efficiency on the sixth power of the distance is that E is most sensitive to distance changes in the range of R_0 (see figure 2.4, right). Typical values for R_0 are 40-80 Å, making FRET a powerful tool to measure distances in the range of 2-10 nm and giving it the nickname of a “spectroscopic ruler” (Stryer and Haugland, 1967; Schuler et al., 2005).

In ensemble experiments, when reference data of single labeled species are available, the FRET efficiency can be calculated either from the decrease in donor emission or the increase in acceptor emission. For single-molecule experiments, the FRET efficiency is calculated from the photons collected in the donor and acceptor channels (F_D , F_A) and their respective quantum yields (Φ_D , Φ_A) as:

$$E = \frac{F_A/\Phi_A}{F_A/\Phi_A + F_D/\Phi_D} \quad (2.11)$$

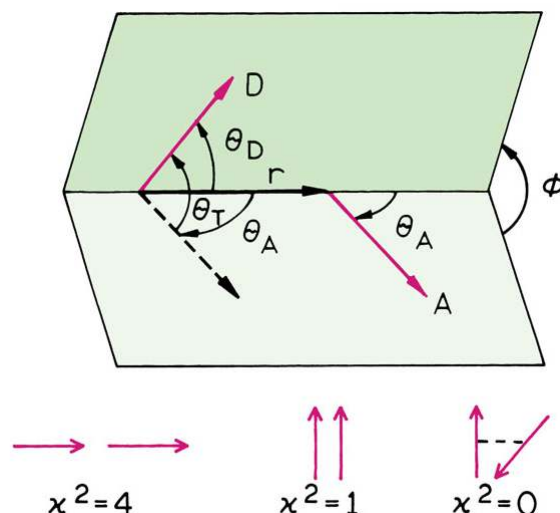


Figure 2.6: Orientation of donor and acceptor dipoles. Additionally, the κ^2 values for collinear, parallel and perpendicular arrangement are shown. Taken from Lakowicz, 2009.

Another way to determine the FRET efficiency is from the quenching of the donor as characterized by the donor lifetime in the presence ($\tau_{D,A}$) and absence ($\tau_{D,0}$) of the acceptor. From equation 2.9 it follows that:

$$E = 1 - \frac{\tau_{D,A}}{\tau_{D,0}} \quad (2.12)$$

2.3 Fluorescence Anisotropy

The fluorescence anisotropy, r , describes the polarization of the fluorescence signal. To measure the anisotropy, polarized excitation has to be applied and the emitted light is split into parallel (I_{\parallel}) and perpendicular (I_{\perp}) components relative to the polarization of the excitation light. The fluorescence anisotropy is given by the intensity difference between the intensities of the two measured polarizations, normalized by the total signal intensity:

$$r = \frac{I_{\parallel} - I_{\perp}}{I_{\parallel} + 2I_{\perp}} \quad (2.13)$$

Theoretically, the anisotropy can assume any value between -0.5 and 1. For molecules in solution, the orientation is random. The probability of absorption is highest for molecules with their absorption dipole oriented parallel to the polarization of the incident light, however also molecules that deviate from this orientation are excited (photoselection). The averaging due to this effect reduces the resulting fundamental (or maximal possible) anisotropy, denoted as r_0 , by a factor of $2/5$, so that $-0.2 \leq r_0 \leq 0.4$. For real fluorophores the anisotropy is further lowered due to the fact that absorption and emission dipoles are usually not collinear. The additional depolarization is dependent on the angle β between absorption and emission dipole:

$$r_0 = \frac{2}{5} \left(\frac{3 \cos^2 \beta - 1}{2} \right) \quad (2.14)$$

The value for β is dependent on the fluorophore as well as on the excitation wavelength. Usually, the fundamental anisotropy can be assumed to be close to 0.4. Fluorescence anisotropy allows one to measure rotational diffusion. For a spherical rotator, the anisotropy decay is given by:

$$r(t) = r_0 \exp\left(-\frac{t}{\rho}\right) \quad (2.15)$$

Here, ρ is the rotational correlation time. For a spherical molecule, it is related to the viscosity of the medium η and the volume of the sphere V by: $\rho = \frac{\eta V}{RT}$, where R is the gas constant and T is the absolute temperature. The measured or steady-state anisotropy r is given by:

$$r = \frac{\int_0^{\infty} I(t)r(t) dt}{\int_0^{\infty} I(t) dt} \quad (2.16)$$

Assuming single exponential decays for both the intensity and anisotropy, the Perrin equation is obtained:

$$\frac{r_0}{r} = 1 + \frac{\tau}{\rho} \quad (2.17)$$

This equation enables the determination of rotational correlation times from anisotropy and lifetime. The anisotropy information can also be used to distinguish complexes of different sizes. For a fluorophore labeled biomolecule, usually the anisotropy decay is described by two components. The dye is, to some degree, flexible in orientation, which leads to an initial anisotropy decay (ρ_1). The slower rotation of the whole complex (ρ_2) then causes the decay of the residual anisotropy r_2 :

$$r(t) = \left((r_0 - r_2)e^{-\frac{t}{\rho_1}} + r_2 \right) e^{-\frac{t}{\rho_2}} \quad (2.18)$$

If the rotation of the complex is much slower the lifetime of the fluorophore ($\rho_2 \gg \tau$), the second exponential can be neglected.

2.4 Accurate FRET efficiencies from three-color MFD-PIE data

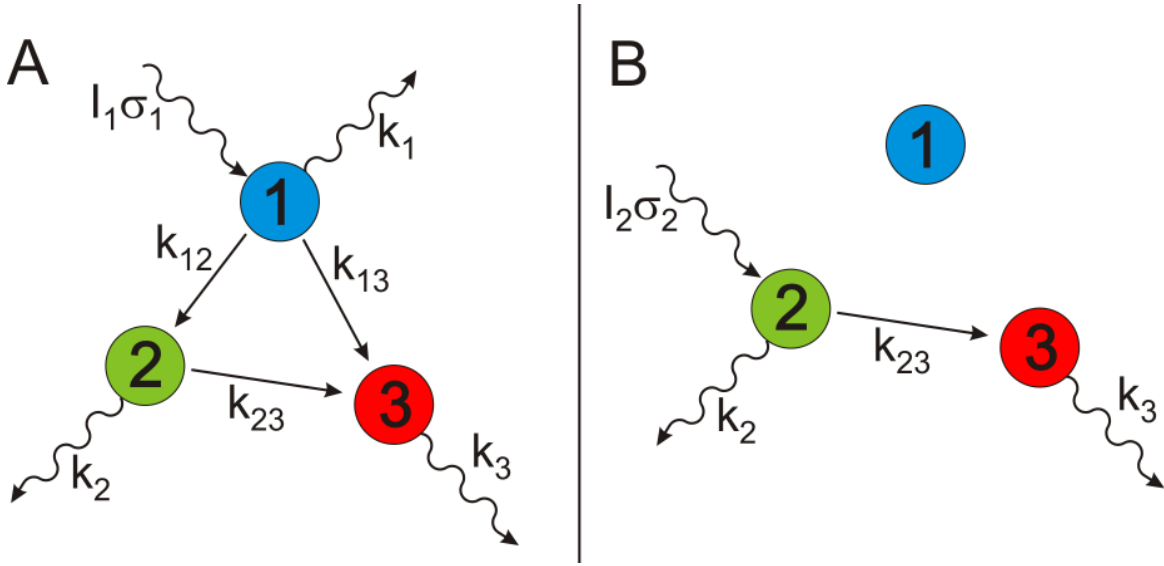


Figure 2.7: FRET scheme with possible transitions and associated rate constants for (A) excitation of the blue dye and (B) excitation of the green by applying PIE.

Extension of the simple donor-acceptor FRET pair (DA) to a system with one donor and two acceptors (DA₁A₂) complicates the determination of actual FRET efficiencies. Analogous to the two-dye system, apparent FRET efficiencies (or proximity ratios) can be defined:

$$\epsilon_{23} = \frac{F_{3,2}}{F_{2,2} + F_{3,2}}; \quad \epsilon_{12} = \frac{F_{2,1}}{F_{1,1} + F_{2,1}}; \quad \epsilon_{13} = \frac{F_{3,1}}{F_{1,1} + F_{3,1}} \quad (2.19)$$

Here, $F_{x,y}$ denotes the fluorescence signal of dye x after excitation of y . Although these quantities are related to the actual FRET efficiencies, they do not follow the previously discussed distance dependence for FRET (see equation 2.10 on page 18).

Figure 2.7 depicts the system of three dyes for (A) the case of excitation of dye 1, and (B) for excitation of dye 2, as is the case for PIE. The probing of the third dye is not discussed, as no FRET can occur in this case; it is, however, important to obtain the stoichiometry parameter, as will be discussed later (see section 3.8.1). Dyes are excited with rate $I_x\sigma_x$, that is their excitation rate is proportional to their absorption cross section at the excitation wavelength and the excitation power. Excited dyes can then either relax by fluorescing with radiative rates k_x or by resonance energy transfer from x to y with rate k_{xy} . Other pathways that depopulate the excited state of dye x , that is non-radiative relaxation, quenching processes, as well as possible transitions to triplet states, are summarized in a single rate constant $k_x^{nr} = \sum_{nr} k_i$. The FRET efficiency from dye x to dye y , as defined by the rate constants, is given by:

$$E_{xy} = \frac{k_{xy}}{k_x + k_{xy} + k_x^{nr}} \quad (2.20)$$

For the case of excitation of dye 2, the system can be described by the following set of

differential equations, where $[X]$ denotes the population of the ground state of dye X and a star denotes the first excited state:

$$\frac{d[2^*]}{dt} = I_2\sigma_2[2] - k_2[2^*] - k_{23}[2^*] - k_2^{nr}[2^*] \quad (2.21)$$

$$\frac{d[3^*]}{dt} = k_{23}[2^*] - k_3[3^*] - k_3^{nr}[3^*] \quad (2.22)$$

The fluorescence intensities $F_{x,y}$ are then proportional to the population of the first excited state:

$$F_{x,y} \propto k_x[X^*] \quad (2.23)$$

Solving these equations for the steady-state case yields for the fluorescence intensities:

$$F_{2,2} = \frac{k_2}{I_2\sigma_2 + k_2 + k_2^{nr} + k_{23}} I_2\sigma_2 \quad (2.24)$$

$$F_{3,2} = \frac{k_{23}}{I_2\sigma_2 + k_2 + k_2^{nr} + k_{23}} I_2\sigma_2 \quad (2.25)$$

With the definition of the FRET efficiency, this yields:

$$E_{23} = \frac{k_{23}}{k_2 + k_{23} + k_2^{nr}} = \frac{F_{3,2}}{F_{2,2} + F_{3,2}} \quad (2.26)$$

Neglecting correction factors, this result coincides with the previous definition of the proximity ratio. Note here that additional quenching processes effecting the donor fluorophore (e.g. the presence of a second acceptor dye as in three-color FRET) do not alter the calculation of the FRET efficiency from photon counts. The respective rates of the quenching processes will be added to the denominators of equations 2.24 and 2.25, but cancel in equation 2.26.

For the case of excitation of the first dye, the rate equations read as follows:

$$\frac{d[1^*]}{dt} = I_1\sigma_1[1] - k_1[1^*] - k_{12}[1^*] - k_{13}[1^*] - k_1^{nr}[1^*] \quad (2.27)$$

$$\frac{d[2^*]}{dt} = k_{12}[1^*] - k_2[2^*] - k_{23}[2^*] - k_2^{nr}[2^*] \quad (2.28)$$

$$\frac{d[3^*]}{dt} = k_{13}[1^*] + k_{23}[2^*] - k_3[3^*] - k_3^{nr}[3^*] \quad (2.29)$$

Solving again for the steady-state case yields:

$$F_{1,1} = \frac{k_1}{I_1\sigma_1 + k_1 + k_1^{nr} + k_{12} + k_{13}} I_1\sigma_1 \quad (2.30)$$

$$F_{2,1} = \left(\frac{k_2}{k_2 + k_{23}} \right) \left(\frac{k_{12}}{I_1 \sigma_1 + k_1 + k_1^{nr} + k_{12} + k_{13}} \right) I_1 \sigma_1 \quad (2.31)$$

$$F_{3,1} = \left(\frac{k_{13}}{I_1 \sigma_1 + k_1 + k_1^{nr} + k_{12} + k_{13}} + \left(\frac{k_{23}}{k_2 + k_{23} + k_2^{nr}} \right) \left(\frac{k_{12}}{I_1 \sigma_1 + k_1 + k_1^{nr} + k_{12} + k_{13}} \right) \right) I_1 \sigma_1 \quad (2.32)$$

The correct FRET efficiencies are, according to equation 2.20, given by:

$$E_{12} = \frac{k_{12}}{k_1 + k_{12} + k_1^{nr}} \quad (2.33)$$

$$E_{13} = \frac{k_{13}}{k_1 + k_{13} + k_1^{nr}} \quad (2.34)$$

Additionally, we can define the total FRET efficiency from dye 1 to both acceptors, which is related to the quenching of the donor as measured by the lifetime:

$$E_{1A} = \frac{k_{12} + k_{13}}{k_1 + k_{12} + k_{13} + k_1^{nr}} = \frac{k_{12}}{k_1 + k_{12} + k_{13} + k_1^{nr}} + \frac{k_{13}}{k_1 + k_{12} + k_{13} + k_1^{nr}} = E_{12,3} + E_{13,2} \quad (2.35)$$

$$E_{1A} = 1 - \frac{\tau_{D,23}}{\tau_{D,0}} \quad (2.36)$$

Here, the efficiencies $E_{12,3}$ and $E_{13,2}$ are defined, representing the apparent FRET efficiency from dye 1 to dye 2 and 1 to 3 in the presence of the third dye, that is when the donor is quenched by the competing FRET process. $\tau_{D,23}$ and $\tau_{D,0}$ are the lifetimes of the donor in the presence and absence of the acceptor dyes, respectively.

The fluorescence intensities can now be expressed by means of the defined FRET related quantities:

$$F_{1,1} = (1 - E_{1A}) I_1 \sigma_1 \quad (2.37)$$

$$F_{2,1} = E_{12,3} (1 - E_{23}) I_1 \sigma_1 \quad (2.38)$$

$$F_{3,1} = (E_{13,2} + E_{12,3} E_{23}) I_1 \sigma_1 \quad (2.39)$$

Using equations 2.30 to 2.32, 2.33 and 2.34, the FRET efficiencies can be calculated from the photon counts after blue excitation:

$$E_{12} = \frac{F_{2,1}}{F_{1,1} (1 - E_{23}) + F_{2,1}} \quad (2.40)$$

$$E_{13} = \frac{F_{3,1} - E_{23}(F_{2,1} + F_{3,1})}{F_{1,1} + F_{3,1} - E_{23}(F_{1,1} + F_{2,1} + F_{3,1})} \quad (2.41)$$

The FRET efficiency E_{23} has to be available by other means, that may be a separate measurement or, more elegantly, E_{23} can be made available on the single molecule basis by applying PIE or ALEX and directly exciting the green dye. Note that since both E_{12} and E_{13} depend on the knowledge of the efficiency E_{23} , the accuracy of the former is strongly dependent on the accuracy of E_{23} . Good care should thus be taken to minimize the shot-noise broadening of E_{23} .

Although these formulas seem complex, they can be understood intuitively. First, consider that additional quenching of the donor does not alter the calculation of the FRET efficiency from photon counts, as is the case for the red dye when calculating E_{12} and for the green dye when calculating E_{13} . This is why the signal from the blue dye does not need to be corrected in any way. The only correction that has to be performed is to redistribute the photons from the green and red dyes to reverse the FRET between them. Equations 2.40 and 2.41 can be arranged to read as:

$$E_{12} = \frac{F_{2,1}/(1-E_{23})}{F_{1,1} + F_{2,1}/(1-E_{23})} \quad (2.42)$$

$$E_{13} = \frac{F_{3,1} - E_{23}(F_{2,1}/(1-E_{23}))}{F_{1,1} + F_{3,1} - E_{23}(F_{2,1}/(1-E_{23}))} \quad (2.43)$$

In the case of E_{12} , the correction reduces to adding back the FRET from green to red by dividing by $(1 - E_{23})$. For E_{13} we have to subtract from the red signal the photons that originate from the green dye. For this, first the green signal is corrected as before and subsequently multiplied by E_{23} to obtain the number of FRET photons from the green dye. This number is then subtracted from the total signal in the red channel.

3 Materials and Methods

3.1 Experimental Setup

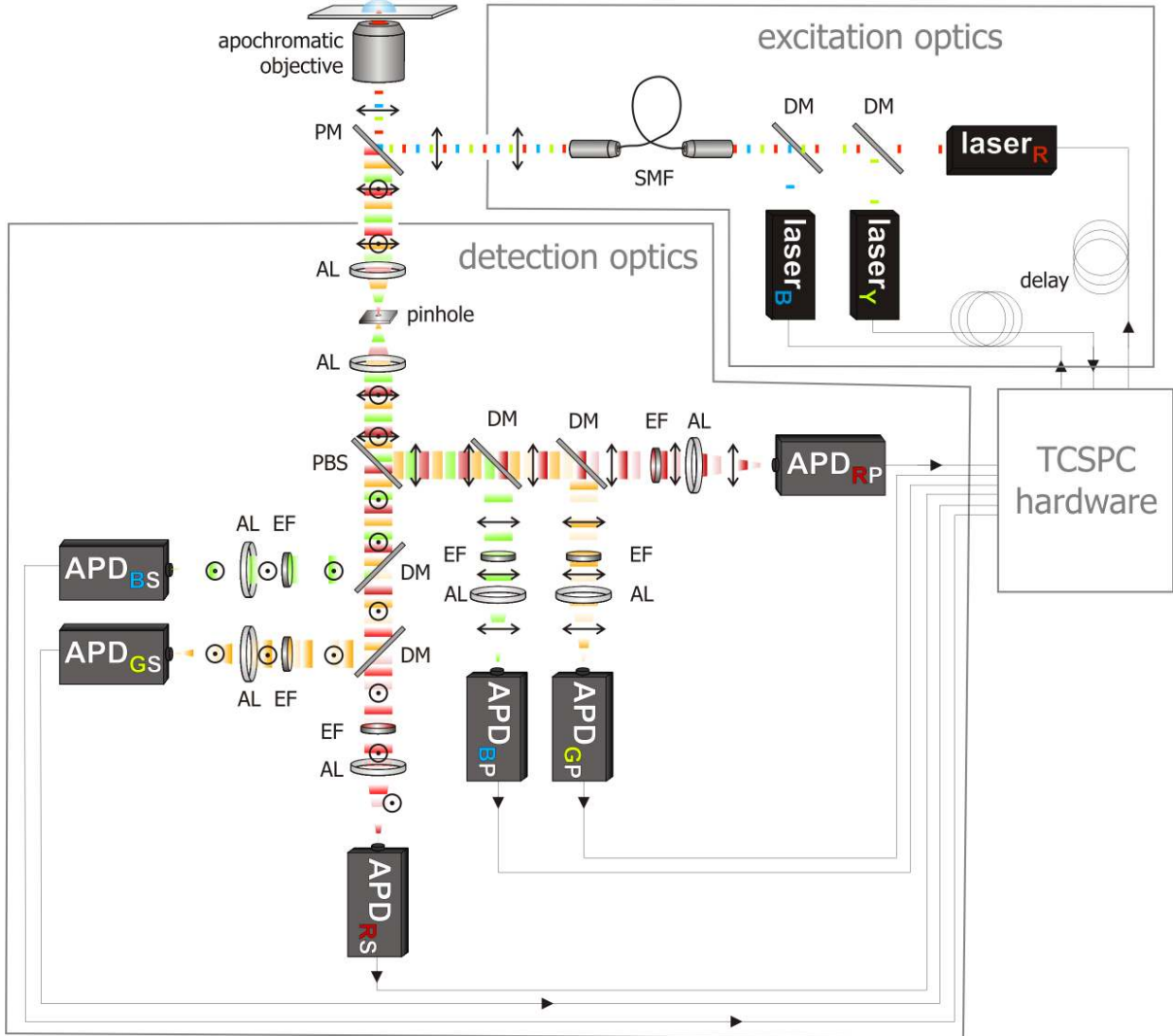


Figure 3.1: Experimental setup for three-color MFD-PIE measurements. The six-channel confocal microscope allows for parallel detection of spectral range, polarization and arrival time of photons. The microtime information additionally enables the determination of the excitation source. TCSPC: Time-correlated single photon counting, DM: Dichroic mirror, PM: Polychroic mirror, AL: Achromatic lens, PBS: Polarizing beamsplitter, EF: Emission filter, APD: Avalanche photodiode. Adapted from Hendrix and Lamb (2013).

Three-color FRET measurements are performed on a home-built confocal three-color dual polarization detection setup with three-color pulsed interleaved excitation (PIE). This setup combines PIE (Müller et al., 2005) with multiparameter fluorescence detection (Eggeling et al., 2001) and extends these concepts to three colors (see figure 3.1). The setup is based on a Nikon Eclipse Ti-DH inverted microscope. The blue and red excitation light is provided by picosecond pulsed diode lasers at 480 nm and 641 nm (LDH-D-C-485 and LDH-D-C-640, PicoQuant). For

the green/yellow excitation light, a tunable frequency-doubled fiber-based femtosecond pulsed laser (FemtoFiber and SHG, Toptica Photonics) is operated at 565 nm at a fixed frequency of ~ 27.4 MHz. The lasers are coupled into a polarization maintaining single-mode fiber (PM-488PM-FC-5, Thorlabs), collimated (Schäfter und Kirchhoff) and focused into the sample by a 60x 1.27 NA water immersion objective (Plan Apo IR 60x 1.27 WI, Nikon). Laser powers as measured before the objective were usually 110 μW for the blue laser, 80 μW for the green laser and 100 μW for the red laser, whereat the blue laser power is limited by the applied pulse sequence (see section 4.1). Fluorescence is collected by the same objective, separated from excitation light by a polychroic mirror (zt405/488/561/633, AHF Analysentechnik) and focused through a 50 μm pinhole. Photons are subsequently separated by polarization using a polarizing beamsplitter (PBS251, 420-680 nm, Thorlabs) and distributed on the three detection channels by two dichroic mirrors (BS560 imaging and 640DCXR, AHF Analysentechnik). Fluorescence is additionally filtered by emission filters in the three channels (red: ET670/30; green: ET607/36; blue: ET525/50, AHF Analysentechnik). Single photons are detected using 6 single photon counting avalanche photodiodes (green: 2x SPCM-AQR-14; red: 2x SPCM-AQRH-14, Perkin Elmer, and blue: 2x COUNT-100B, LaserComponents) and registered by four TCSPC data collection cards (SPC-150, Becker&Hickl). The channels red parallel, green parallel, and green perpendicular are combined onto one TCSPC card using a router (HRT-82, Becker&Hickl). Synchronization of lasers and TCSPC cards is performed by the diode laser driver (SepiaII, PicoQuant) at the fixed frequency of the yellow laser of ~ 27.4 MHz.

Triggering and synchronization of three setups with one master clock and two laser drivers

A total of three setups are driven by the sync pulse of the yellow laser at ~ 27.4 MHz. As the yellow laser is used in both the three-color MFD setup and the three-color confocal scanning setup, both setups need to be supplied with the sync from the yellow laser. Furthermore, only one diode laser driver is available for the two MFD setups. To be able to adjust the pulse sequences for the three-color MFD setup (see section 4.1), triggering of both setups needs to be independent. The triggering scheme is shown in figure 3.2. The sync output of the yellow laser is amplified and split to feed the sync frequency to the oscillator modules of both diode laser drivers. The sync pulse from the laser is a TTL type pulse (Transistor-Transistor Logic), while the rest of the pulses are of the NIM type (Nuclear Instrumentation Module). The oscillator module of the top diode laser driver is used to trigger the three-color MFD lasers using variable pulse schemes (blue and red arrows) and the TCSPC hardware of this setup is synchronized using the sync out of the oscillator module. Likewise, the oscillator module of the bottom diode laser driver is used to trigger the lasers of the three-color confocal scanning setup, and the sync output of the oscillator module is used to synchronized the TCSPC hardware. Since the red and blue lasers of this setup are exclusively operated at the repetition rate of the yellow laser and no variation of the pulse sequences is needed, the third trigger output channel of the

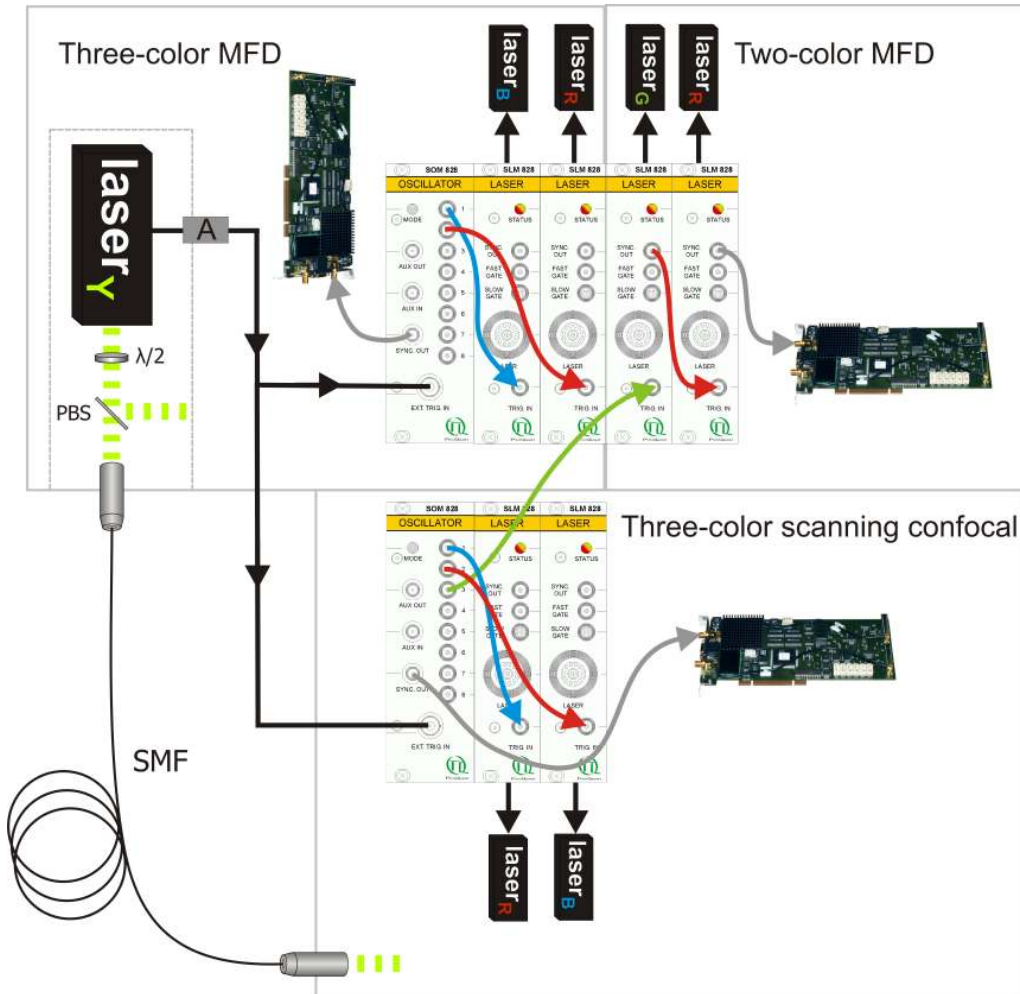


Figure 3.2: Triggering scheme used to drive the three setup with the sync output of the yellow laser. Black: TTL pulse from the laser to trigger the two SepiaII laser drivers. Colored: NIM signals from the burst out of the oscillator modules to trigger the respective lasers. gray: NIM signal from sync out channels to trigger the TCSPC cards. A: Pulse amplifier, $\lambda/2$: half-waveplate, PBS: Polarizing beamsplitter, SMF: Single-mode fiber.

oscillator module is used to trigger the green laser of the two-color MFD setup (green arrow). Subsequently, the sync output of this laser module is used to trigger the red laser at the same frequency (red arrow). Finally, the TCSPC hardware of this setup is synchronized using the sync out of the red laser module (gray arrow). The splitting of the yellow laser to supply both setups simultaneously is achieved by variably turning the polarization with a half-waveplate and splitting with a polarizing beamsplitter. Since the three-color confocal scanning setup is located in another room, the laser is coupled into a single-mode polarization-maintaining fiber of 30 m length.

3.2 Confocal Microscopy

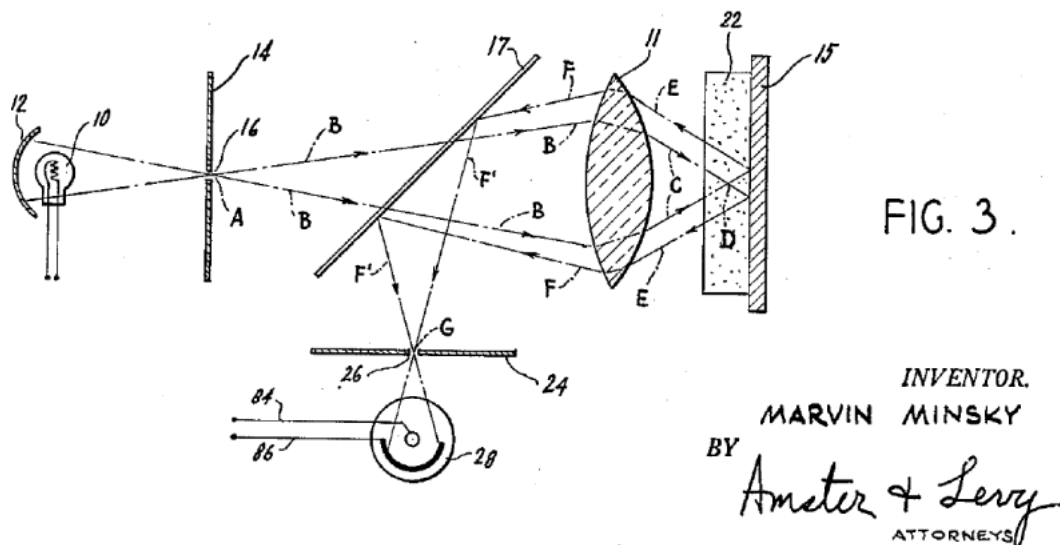


Figure 3.3: Scheme of the confocal principle from the original patent (Minsky, 1957).

Confocal microscopy combines point illumination by an objective lens with an aperture (pinhole) in the optically conjugate plane in the detection pathway. The excitation light is focused into the sample by the objective lens, reaching diffraction limited size in the focal plane. Although the light is focused by the objective, excitation of molecules occurs throughout the entire illuminated volume. The pinhole restricts the detection volume to the focal plane of the objective, thus discarding all out-of-focus light. The convolution of excitation and detection volumes results in a limited measurement volume or point spread function (PSF). The PSF describes how a point source is imaged by the optical system. It is usually described by a three-dimensional Gaussian:

$$PSF(r) = e^{-2\frac{x^2+y^2}{\omega_r^2}} - 2\frac{z^2}{\omega_z^2} \quad (3.1)$$

The radial size of the volume ω_r is of the order of 200-400 nm, depending on the wavelength of the excitation light, while the axial size ω_z is about 5 times larger. If the objective lens is not entirely filled with excitation light, the focus size will increase. Systematic underfilling of the objective, as applied in this work, increases ω_r to values of 500-600 nm (as determined by FCS).

3.3 Fluorescent dyes

The dyes used in this work are Atto488, Atto565 and Atto647N (ATTO-TEC). Their properties are listed in table 3.1 and the absorption spectra are shown in figure 3.4. Several points have to be considered when choosing dyes for three-color FRET applications. First, it should be possible to clearly separate the dyes spectrally to record their fluorescence in independent detection channels. On the contrary, for reasonable FRET to occur, the dyes must exhibit significant spectral overlap. The choice of suitable dyes for quantitative FRET is also limited by the properties of the dyes. Near-infrared dyes usually suffer from low quantum yield, while blue dyes have low extinction coefficients. For a detailed discussion of dye choices for multicolor FRET applications, see sections 5.5 and 5.6.

Dye	QY	τ	λ_{abs}^{max}	$\varepsilon(\lambda_{abs}^{max})$	λ_{em}^{max}	λ_{ex}	$\varepsilon_{rel}(\lambda_{ex})$
Atto488	0.8	4.1 ns	501 nm	$9.0 \cdot 10^4 \text{ M}^{-1}\text{cm}^{-1}$	523 nm	480 nm	47.6%
Atto565	0.9	4.0 ns	563 nm	$1.2 \cdot 10^5 \text{ M}^{-1}\text{cm}^{-1}$	592 nm	565 nm	98.5%
Atto647N	0.65	3.5 ns	644 nm	$1.5 \cdot 10^5 \text{ M}^{-1}\text{cm}^{-1}$	669 nm	641 nm	94.3%

Table 3.1: Fluorescence properties of the dyes. QY: Quantum yield, τ : fluorescence lifetime, λ_{abs}^{max} : Wavelength at maximum absorption, $\varepsilon(\lambda_{abs}^{max})$: Maximum absorption coefficient, λ_{em}^{max} : Maximum emission wavelength, λ_{ex} : Excitation wavelength, $\varepsilon_{rel}(\lambda_{ex})$: Relative extinction at the excitation wavelength.

Calculated purely from the overlap between the emission spectra and the emission filters (see figure 3.5), the detection efficiencies are 58% for Atto488, 45% for Atto565 and 38% for Atto647N. The theoretical crosstalk or bleedthrough is calculated as 11% for Atto488 into the green channel, 9% for Atto565 into the red channel and 0.8% for Atto488 into the red channel. These values match with the experimentally determined values for the crosstalk of the blue dye, however the experimental crosstalk from the green dye into the red channel is unexpectedly high at ~15%.

The Förster radii for the dye pairs are 51 Å for Atto488-Atto647N, 63 Å for Atto488-Atto565 and 68 Å for Atto565-Atto647N, assuming $\kappa^2 = 2/3$.

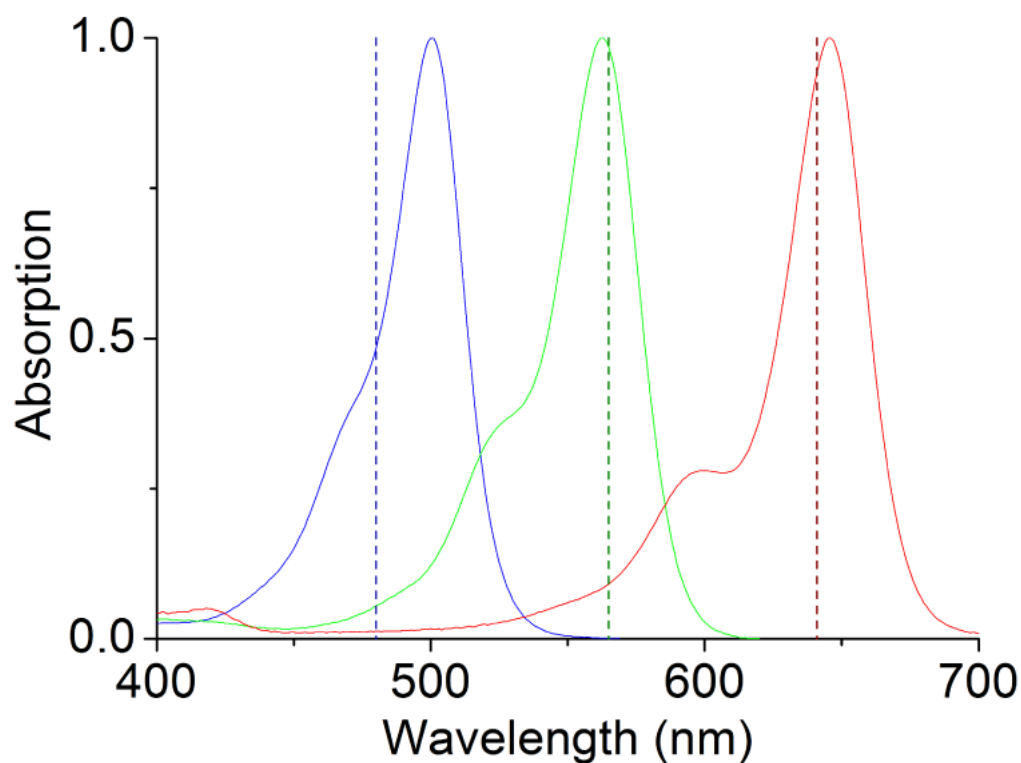


Figure 3.4: Normalized absorption spectra of Atto488 (blue), Atto565 (green) and Atto647N (red). The excitation wavelengths are shown by dashed lines.

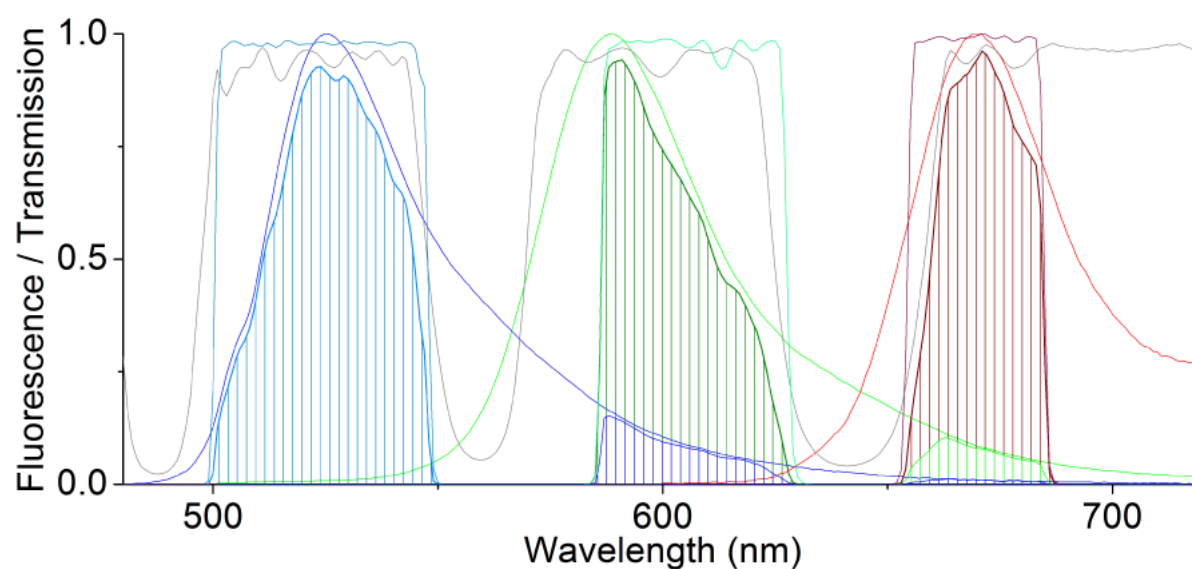


Figure 3.5: Emission spectra of Atto488, Atto565 and Atto647N and transmission spectra of the used filters (color coded) and the polychroic (gray). The shaded regions are the detected parts of the spectra.

3.4 Detectors

Single-photon avalanche photodiodes (APDs) are used to detect single photons. Different modules have different detection probabilities depending on the wavelength of the incident photons. The red channels are equipped with APDs of type SPCM-AQRH-14 and the green channels with modules of type SPCM-AQR-14 (Perkin Elmer). These modules have good detection efficiencies of more than 60% from 550-800 nm, but low efficiency for wavelengths of 500 nm and below. The blue detection channels are equipped with modules specifically optimized for this wavelength region (COUNT blue, LaserComponents), with more than 70% detection efficiency for the spectral region of interest. The detection efficiencies of the different detectors are shown in figure 3.6.

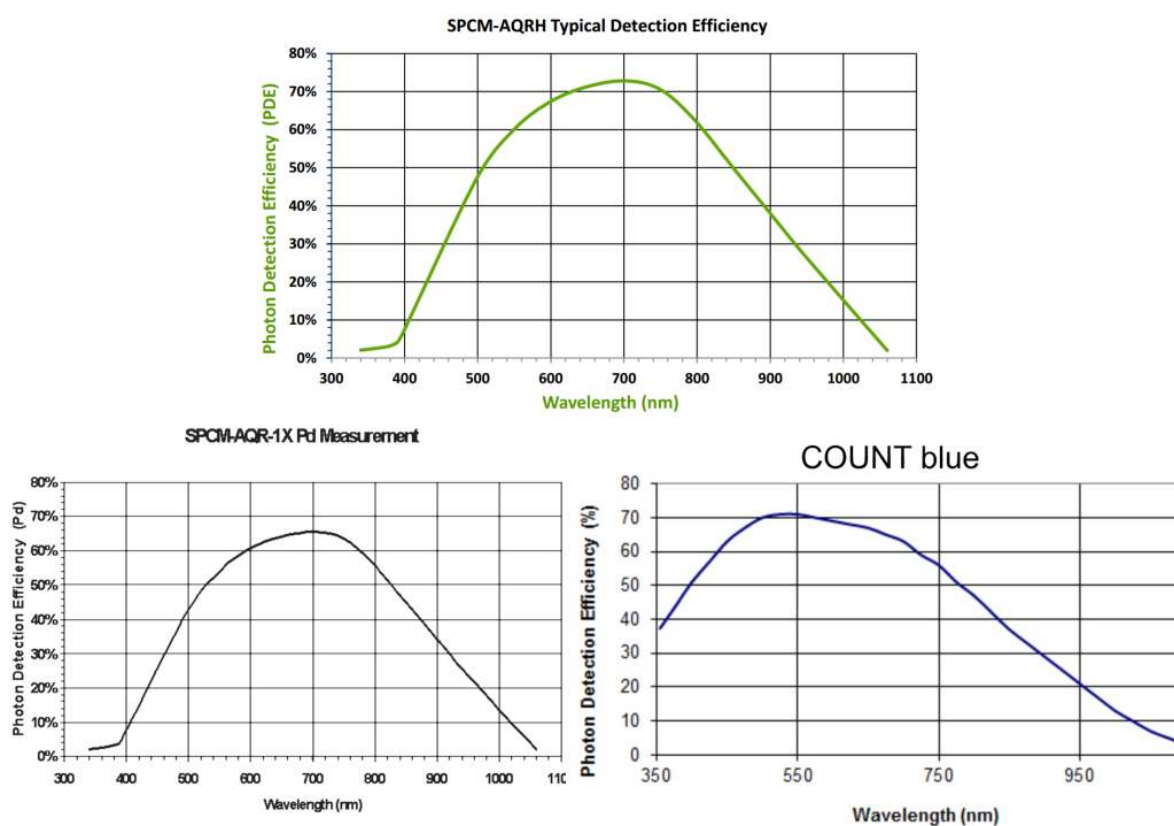


Figure 3.6: Detection efficiencies of the different APDs used in this work as a function of wavelength. Taken from ExcelitasTechnologies (2005); PerkinElmer (2005); LaserComponents (2013).

3.5 DNA molecules

```
5'-GGC TCG CCT GGT AAG TGT TGT ATG ATG TAT TCG GTG CGG G  
3'-CCG AGC GGA CCA TTC ACA ACA TAC TAC ATA AGC CAC GCC C-biotin
```

```
5'-GGC TCG CCT GGT AAG TGT TGT ATG ATG TAT TCG GTG CGG G  
3'-CCG AGC GGA CCA TTC ACA ACA TAC TAC ATA AGC CAC GCC C-biotin
```

Figure 3.7: Sequences of the two DNA molecules used in this work. The labeled nucleotides are colored.

The sequences of the used DNA molecules are shown in figure 3.7. The sequence of the double strand was chosen such that the formation of secondary structure elements (e.g. hairpins) is unlikely. The first and the third dye are located on the same side of the double helix, while the second dye is positioned at equal distance to the two terminal dyes on the other side.

3.6 Pulsed interleaved excitation

Pulsed interleaved excitation (PIE, Müller et al., 2005) extends on the idea of alternating laser excitation (ALEX, Kapanidis et al., 2004) for multicolor fluorescence spectroscopy. Instead of alternating continuous wave (cw) lasers on the microsecond timescale by acousto-optical modulators (AOM), PIE utilizes alternating excitation by pulsed lasers (figure 3.8, A). The alternating excitation within one microtime range defines four PIE channels, i.e. GG, GR, RG and RR, where the first letter denotes the excitation source and the second letter is the detection channel (figure 3.8, B). Hereby, information about the excitation source is obtained from the respective microtime ranges (0-20 ns for green excitation, 20-40 ns for red excitation). The PIE channel GG contains the photons originating from the green dye after green excitation. FRET photons are detected in the channel GR, however also other contributions have to be considered: Crosstalk of the green emission and direct excitation of the red dye by the green laser will likewise be detected in this channel. The green dye is not excited by the red laser and crosstalk of the red dye into the green channel is usually non-existent, thus the channel RG is empty. Lastly, the channel RR contains red photons after red excitation from the direct probing of the acceptor dye. PIE brings many advantages for fluorescence correlation spectroscopy (FCS), mainly crosstalk-free fluorescence cross-correlation spectroscopy (FCCS) and the ability to determine absolute FRET efficiencies without calibration. For burst analysis, the advantage of PIE over single laser excitation is that due to probing of the red dye the analysis can be limited to double-labeled molecules (see section 3.8.1). The advantage of PIE over ALEX is that due to the pulsed excitation also the lifetime of the acceptor dye is accessible, which further allows to distinguish FRET changes from photophysical artifacts or changes in the local environment.

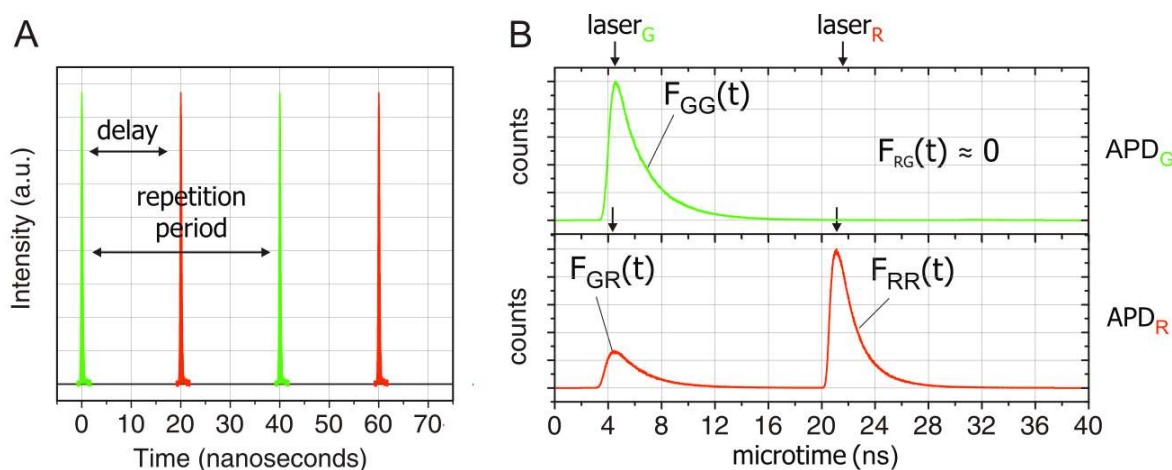


Figure 3.8: Illustration of the principle of PIE. A) Pulse sequence for two-color PIE. Alternative excitation by a green and red laser operated at equal repetition rate is achieved by delaying the red laser. B) Microtime histogram of the two detection channels. Adapted from Hendrix and Lamb (2013).

The experimental realization of PIE by time-correlated single photon counting (TCSPC) is depicted in figure 3.9. Both lasers are triggered at the same sync rate, and the red laser is

electronically delayed by half of the repetition period. Three different events are shown: green excitation, green detection; green excitation, red detection; and red excitation, red detection. Every photon detection event is described by two parameters: the macrotime (or laboratory time) and the microtime. The macrotime is given by the time passed since the start of the measurement, as determined by the number of sync pulses registered prior to detection. The microtime is given relative to the previous sync pulse. Experimentally, microtimes are recorded by using a time-to-amplitude converter (TAC) that is triggered by the detection event. The TAC is then charged linearly with time and stopped by the next sync pulse (reverse start-stop). The amplitude of the accumulated voltage is proportional to the time between the detection event and the subsequent sync pulse.

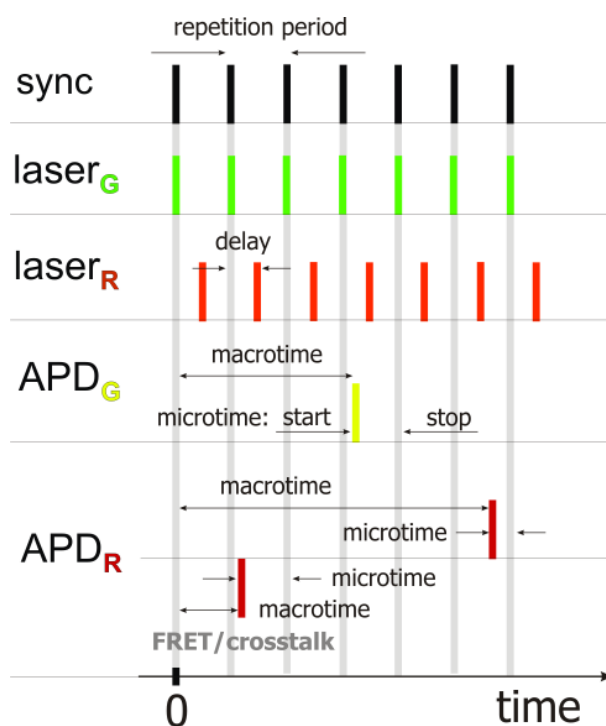


Figure 3.9: Experimental realization of two-color PIE. Adapted from Hendrix and Lamb (2013).

3.7 Burst Analysis

Burst analysis is based on the idea of observing single molecules in solution by combining low concentrations with the small observation volume of a confocal microscope (Zander et al., 1996). Usually, picomolar concentrations are applied and observation volumes are approximately femtoliter sized, achieving an average number of molecules far below one ($\langle N \rangle < 0.05$). A representative signal trace is shown in figure 3.10, left, exhibiting occasional bursts of fluorescence when a molecule diffuses through the focus. Depending on the diffusion properties of the molecule and the viscosity of the medium, burst durations are usually on the order of a few milliseconds and show log-normal distribution (Eggeling et al., 2001, see figure 3.10, right). For burst analysis, a large confocal volume is desirable to increase the observation time, achieved by underfilling of the objective back aperture. Significantly longer burst durations of hundreds of milliseconds can be achieved e.g. by increasing the viscosity of the medium or by trapping the molecules inside of vesicles (Ernst et al., 2012a). When selecting bursts, one has to consider that individual events will differ in brightness because every molecule takes a random path through the focus and that less bright species will be less likely detected. This inherent bias is not avoidable and will depend on the specific algorithm applied.

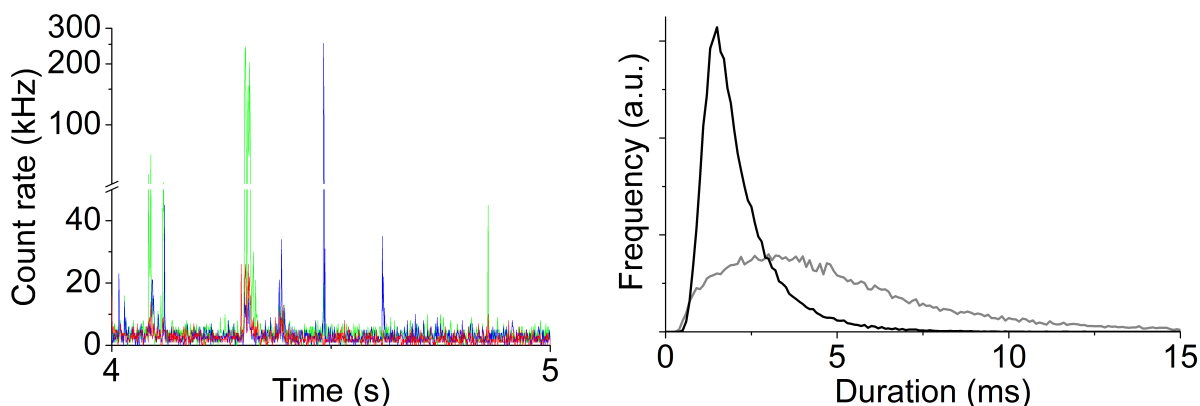


Figure 3.10: (Left) Time trace of a three-color burst measurement. The colors correspond to the respective detection channels. (Right) Burst size distribution for DNA (black) and the protein BiP (gray).

Burst search algorithms

Different criteria to distinguish bursts from background have been proposed based on binning of the time trace (Deniz et al., 2001) or smoothing of interphoton times by applying a Lee-filter (Enderlein et al., 1997; Eggeling et al., 2001; Fries et al., 1998), and subsequent thresholding. In this work, burst selection is performed as proposed by Nir et al. (2006), in what is called an all-photon burst search (APBS). In the first step, a total photon time trace is generated by combining all available detection channels. Then a sliding time window is applied to probe the local count rate around each individual photon. If a given threshold is exceeded, the photon is

considered to belong to a burst. Every train of valid photons is considered as a burst when a lower threshold for the photon number is surpassed. The three parameters, that is photons per burst (L), time window length (T) and photons per timewindow (M), can be adjusted according to the situation. Setting the minimum number of photons per burst high will reduce shot noise, but also biases the selection towards brighter species in general. The timing resolution given by the time window length defines how well the edges of bursts are detected. A smaller timing window will detect the rise of signal more accurately and will be more sensitive for short-lived fluctuations. The window should, however, not be chosen too small so that the local count rate can still be realistically estimated (a count rate of 100 kHz equals to 1 photon every 10 μ s on average). Additionally, consider the case that a molecule diffuses to the edges of the confocal volume and back into the center of the focus. If the time window is set too small, the short-lived decrease in count rate will be significant and the burst will be split into two. The same applies for blinking of the dyes. Essentially, the burst size distribution will be artificially shifted to shorter burst durations. Lastly, if the ratio M/T , which is an estimate for the local count rate, is chosen too small, only those molecules that diffuse through the center of the focus will be detected, whereas smaller values will also allow detection of molecules diffusing along the edges. The usual parameters used in this work were $T = 500 \mu$ s, $L = 100$ and $M = 5 - 30$, depending on the expected brightness of the molecules, corresponding to threshold count rates of 10-60 kHz. Note that filtering for the total number of photons per burst can also be done retroactively.

Nir et al. (2006) introduced dual-channel burst search (DCBS). In DCBS, the additional information available by PIE is used to identify only those bursts that show activity on all channels. Separate burst searches are performed on the combined channel of photons after green excitation ($GX = GG + GR$) and the red channel after red excitation (RR). Then only those photons that are detected during active periods in both channels are considered valid. Applying this burst search method naturally removes incompletely labeled molecules. FRET values obtained from APBS are usually corrupted by blinking and multi-molecule events. This is rectified in DCBS. First, consider the case of acceptor photoblinking during a burst that was selected via APBS. The blinking period will be included and the FRET value will be skewed to smaller values. DCBS however will report two bursts of accurate FRET efficiency, although the burst size distribution will be altered. Second, consider the event that a donor only molecule enters the focus during a burst. APBS will find the ending of the burst when the donor only molecule leaves the focus, and will report a lower FRET efficiency. DCBS will stop the burst the moment the double-labeled molecule leaves the focus, and, while still essentially reporting a wrong FRET efficiency, it will be closer to the correct value.

DCBS has been extended to three colors (TCBS, triple-channel burst search). For three-color measurements, it can be difficult to separate the triple-labeled species from double-labeled species by stoichiometries if these are shot-noise broadened. TCBS naturally removes single or double-labeled molecules and makes this selection obsolete (see section 3.8.4 for a detailed

discussion of filters and burst search algorithms).

3.8 Data Analysis

3.8.1 The Efficiency-Stoichiometry plot in two-color PIE-MFD

For two-color experiments, one of the advantages of PIE-MFD is direct access to the labeling stoichiometry of every recorded single molecule event. The stoichiometry is hereby defined as the ratio of signal after green excitation to the total signal detected:

$$S = \frac{GG + GR}{GG + GR + RR} \quad (3.2)$$

The stoichiometry allows to separate incompletely labeled molecules (donor-only, acceptor-only) from relevant double-labeled molecules. Especially the presence of donor-only molecules is easily misinterpreted as a low FRET species if PIE is not applied. In a plot of stoichiometry versus FRET efficiency (see figure 3.11), all four species of a spFRET measurement can be identified. double-labeled molecules will have a stoichiometry value S that is close to 0.5. Donor-only species are defined by $E \approx 0$ and $S \approx 1$, while acceptor-only molecules have undefined FRET values and a stoichiometry close to zero.

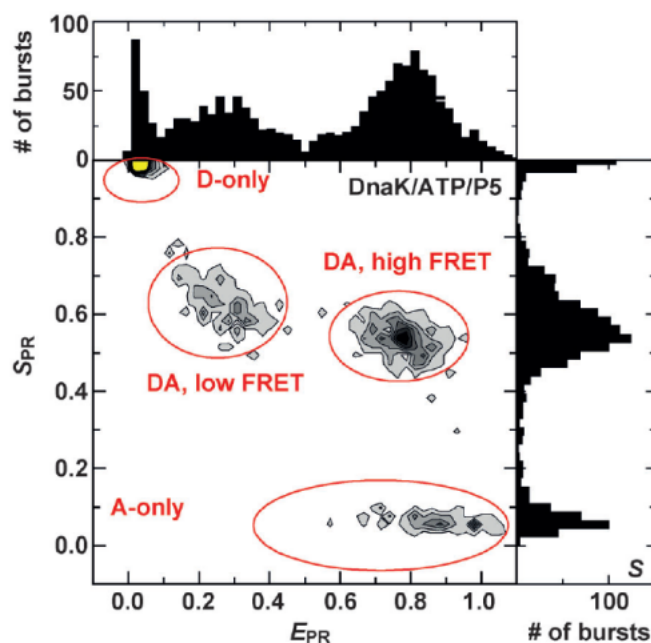


Figure 3.11: 2D histogram of the stoichiometry versus the FRET efficiency of a spFRET measurement of the protein DnaK. Both parameters are uncorrected. Taken from Kudryavtsev et al. (2012).

3.8.2 Calculation of burstwise fluorescence parameters

Corrections

Different corrections to the recorded raw photon counts have to be considered. The corrections presented here are according to Kudryavtsev et al. (2012) and extended to three-colors when needed. A list of the used correction factors for the different measurements presented in this work can be found in the appendix.

Background correction The photons count in every channel have to be corrected for randomly distributed background counts occurring in the channel according to:

$$F_X = N_X - \langle B_X \rangle T \quad (3.3)$$

Here F is the corrected signal, N is the raw number of counts, $\langle B_X \rangle$ is the average background signal as determined from a buffer only measurement and T is the duration of the individual burst. Usually, background count rates are below 1 kHz, averaging to 1 background photon per ms.

Crosstalk and direct excitation For the FRET channels, two corrections have to be considered: Crosstalk describes the probability that a photon originating from the donor is falsely detected in the acceptor channel due to overlap of the emission spectrum of the donor and the emission filter of the acceptor. Direct excitation describes the probability that the acceptor is directly excited by the donor excitation laser as theoretically given by the extinction coefficient of the acceptor at the donor excitation wavelength, $\epsilon_A(\lambda_{ex}^D)$. The signal in the acceptor channel after donor excitation, corrected for direct excitation α and crosstalk β , is given by:

$$F_{GR}^{cor} = F_{GR} - \alpha_{GR} F_{RR} - \beta_{GR} F_{GG} \quad (3.4)$$

The correction factors are defined as follows, with I_X being the excitation intensity of the donor or acceptor excitation laser and $\eta_X^{\lambda_{em}^Y}$ being the detection efficiency in channel X for the fluorescence from dye Y :

$$\alpha_{XY} = \frac{\epsilon_Y(\lambda_{ex}^X) I_X}{\epsilon_Y(\lambda_{ex}^Y) I_Y} \quad (3.5)$$

$$\beta_{XY} = \frac{\eta_X^{\lambda_{em}^Y}}{\eta_X^{\lambda_{em}^X}} \quad (3.6)$$

For the two-color case, these formulas can be expressed using the signals in the respective PIE channels for acceptor or donor only molecules:

$$\alpha_{GR} = \frac{\varepsilon_A(\lambda_{ex}^D)I_D}{\varepsilon_A(\lambda_{ex}^A)I_A} = \frac{F_{GR}^{A-only}}{F_{RR}^{A-only}} \quad (3.7)$$

$$\beta_{GR} = \frac{\eta_G^{\lambda_{em}(A)}}{\eta_G^{\lambda_{em}(G)}} = \frac{F_{GR}^{D-only}}{F_{GG}^{D-only}} \quad (3.8)$$

For correction of photon counts in the three-color case, correction of the channels GR and BG are analogous to the correction described for spFRET:

$$F_{BG}^{cor} = F_{BG} - \alpha_{BG}F_{GG} - \beta_{BG}F_{BB} \quad (3.9)$$

Note that the term correcting for the direct excitation by the blue laser actually reads $\alpha_{BG} \frac{F_{GG}}{1-E_{GR}}(1-E_{GR})$, considering that the direct excitation is proportional to the total number of excitation events and thus the correct counts in the green channel after green excitation ($\frac{F_{GG}}{1-E_{GR}}$), however the number of green photons detected is again reduced by FRET. In this case, the FRET correction cancels out.

For the red photons after blue excitation, two additional corrections have to be considered. The crosstalk of green signal is given by the green signal detected after blue excitation, corrected for the crosstalk of the blue signal, and multiplied by the crosstalk of green to red:

$$(F_{BG} - \beta_{BG}F_{BB})\beta_{GR}$$

Direct excitation of the green dye by the blue laser, and subsequent FRET from the green to the red dye can be calculated as follows: The amount of direct excitation is given by the FRET corrected photon counts in the green channel after green excitation, multiplied by the direct excitation factor. A fraction of these excitation events will be detected in the red channel, given by the FRET efficiency E_{GR} .

$$\left(\alpha_{BG} \frac{F_{GG}}{1-E_{GR}} \right) E_{GR}$$

Combining all these corrections yields:

$$F_{BR}^{cor} = F_{BR} - \alpha_{BR}F_{RR} - \beta_{BR}F_{BB} - \beta_{GR}(F_{BG} - \beta_{BG}F_{BB}) - \alpha_{BG} \frac{E_{GR}}{1-E_{GR}} F_{GG} \quad (3.10)$$

The correction factors for direct excitation and crosstalk can be determined from additional measurements of the free dyes from equation 3.7 and 3.8. More elegantly, they can be determined from the actual measurement if substantial amount of single labeled species are present. Using the donor and acceptor only species from the measurement, one can use the fact that a) for accurate correction of crosstalk the efficiency of the donor only species should be zero and b) for accurate correction of direct excitation the stoichiometry of the acceptor only species should be zero. The correction factors can be calculated from the uncorrected efficiency and

stoichiometry of the single labeled species (E_{raw}^{D-only} , S_{raw}^{A-only} , Kudryavtsev et al., 2012), that is for $\alpha = \beta = 0$ and $\gamma = 1$, whose mean values can be determined by applying a Gaussian fit, as:

$$\alpha = \frac{S_{raw}^{A-only}}{1 - S_{raw}^{A-only}} \quad (3.11)$$

$$\beta = \frac{E_{raw}^{D-only}}{1 - E_{raw}^{D-only}} \quad (3.12)$$

This methodology is extended to three colors by using the proximity ratios as defined before instead of the corrected FRET efficiencies (see A.2.1 for details).

γ -factor The γ -factor corrects for the fact that excitation events of different dyes will be detected with different probabilities, determined by intrinsic dye properties (quantum yield ϕ) and the experimental setup (detection efficiency η). It is defined as:

$$\gamma_{XY} = \frac{\phi_Y \eta_Y^{\lambda_{em}^Y}}{\phi_X \eta_X^{\lambda_{em}^X}} \quad (3.13)$$

For three-color MFD, this reads as:

$$\gamma_{BG} = \frac{\phi_G \eta_G^{\lambda_{em}^G}}{\phi_B \eta_B^{\lambda_{em}^B}}, \quad \gamma_{BR} = \frac{\phi_R \eta_R^{\lambda_{em}^R}}{\phi_B \eta_B^{\lambda_{em}^B}}, \quad \gamma_{GR} = \frac{\phi_R \eta_R^{\lambda_{em}^R}}{\phi_G \eta_G^{\lambda_{em}^G}} \quad (3.14)$$

It follows by definition:

$$\gamma_{BR} = \gamma_{BG} \gamma_{GR} \quad (3.15)$$

One important thing to note regarding the γ -factor is the fact that essentially, the signal of e.g. the blue dye would also have to be corrected for crosstalk to either of the other channels, that is:

$$F_{BB}^{cor} = (1 + \sum \beta_i) \gamma F_{BB}$$

However, this crosstalk correction is just another factor. In other words: The γ -factor that is defined in burst analysis is actually given by:

$$\gamma^* = \gamma (1 + \sum \beta_i) \quad (3.16)$$

For spFRET measurements, the γ -factor can be determined by comparing FRET efficiencies determined from either lifetime or photon counts (see section 3.8.2). The relation between efficiency and lifetime (see 2.12 on page 19) defines a static FRET line. Using a measurement with two species of different FRET efficiencies in the absence of dynamics, the γ -factor is adjusted so that in a plot of E vs. τ both species fall onto the theoretical curve. For three-color

FRET, first the PIE information has to be used to determine γ_{GR} . Then, the total FRET from the donor to both acceptors E_{1A} (see equation 2.36 on page 23) is used to determine the missing γ -factors:

$$E_{1A} = \frac{\gamma_{GR}F_{BG} + F_{BR}}{\gamma_{BR}F_{BB} + \gamma_{GR}F_{GG} + F_{BR}} = \frac{F_{BG} + F_{BR}/\gamma_{GR}}{\gamma_{BG}F_{BB} + F_{GG} + F_{BR}/\gamma_{GR}} \quad (3.17)$$

Here, the validity of equation 3.15 is assumed. For this method to work, two triple-labeled species have to be available that differ significantly in both E_{GR} and E_{1A} at the same time.

An alternative way to determine the γ -factor is proposed by Lee et al. (2005). The γ -factor corrected stoichiometry is independent of the FRET efficiency. If two double-labeled species with different FRET efficiencies are available, the γ -factor must be chosen such that both species have the same stoichiometry. In practice a linear fit is applied to a plot of $\frac{1}{S_{\gamma=1}}$ vs $E_{\gamma=1}$ (while still correcting the photon counts for crosstalk and direct excitation beforehand). γ is then given by the intercept Ω and the slope Σ as:

$$\gamma = \frac{\Omega - 1}{\Omega + \Sigma - 1} \quad (3.18)$$

This method is limited by the requirement that the quantum yield of both dyes is unchanged in the two species. If this is not fulfilled, a reference measurement of species with known quantum yield can be used to determine γ as discussed here, and the ratio of detection efficiencies can be calculated. Then, knowledge of the quantum yields for arbitrary species enables the direct calculation of γ according to equation 3.14.

Consequently, for three-color MFD three separate measurements are needed to determine all three γ -factors, each of a mixture of double-labeled molecules with different FRET efficiencies. A different approach is proposed here when sub-labeled species are not accessible in a pure form. If two triple-labeled species with different FRET efficiencies between the dyes are available, the same linear relationship between S and E can be reproduced by effectively reducing the three dye system to a two dye system. The photon counts are first corrected for the FRET occurring between the green and the red dye as discussed before (see section 2.4 on page 21):

$$F_{BG}^* = \frac{F_{BG}}{1 - E_{GR}} \quad (3.19)$$

$$F_{BR}^* = F_{BR} - \frac{E_{GR}}{1 - E_{GR}} F_{BG} \quad (3.20)$$

Based on these corrected photon counts, efficiencies (which equal the corrected efficiencies defined before) and sub-stoichiometries S^* are calculated, for which the linear relationship is preserved:

$$S_{BG}^* = \frac{F_{BB} + F_{BG}^*}{F_{BB} + F_{BG}^* + F_{GG} + \frac{1}{\gamma_{GR}} F_{GR}} \quad (3.21)$$

$$S_{BR}^* = \frac{F_{BB} + F_{BR}^*}{F_{BB} + F_{BR}^* + F_{RR}} \quad (3.22)$$

Prior to the calculation of S_{BG}^* , γ_{GR} has to be determined. Note that both definitions require the use of the proximity ratio, that is the respective γ -factor is assumed to be equal to 1. Then again a plot of $\frac{1}{S^*}$ vs E will recover the linear relationship.

Person et al. (2009) discuss that the relation presented in equation 3.15, while theoretically true, will not hold under experimental setup conditions due to excitation and detection volume mismatch between the different excitation wavelengths caused by chromatic aberrations. They propose to alter the definitions of the γ -factors from equation 3.14 by replacing the detection efficiency $\eta_X^{\lambda_Y}$ (that is the detection efficiency of dye X in detection channel Y) with the detection efficiency of dye X in detection channel Y upon excitation by laser Z , ${}^Z\eta_X^{\lambda_Y}$:

$$\gamma_{BG} = \frac{\phi_G^B \eta_G^{\lambda_{em}^G}}{\phi_B \eta_B^{\lambda_{em}^B}}, \quad \gamma_{BR} = \frac{\phi_R^B \eta_R^{\lambda_{em}^R}}{\phi_B \eta_B^{\lambda_{em}^B}}, \quad \gamma_{GR} = \frac{\phi_R^G \eta_R^{\lambda_{em}^R}}{\phi_G \eta_G^{\lambda_{em}^G}} \quad (3.23)$$

Then, the relation $\gamma_{BR} = \gamma_{BG} \gamma_{GR}$ does not hold anymore. Recalling the remark about the interpretation of the γ -factor before (see equation 3.16), another obvious reason is given why experimentally the theoretical relation between the different γ -factors is not reproduced.

An estimate for the different γ -factors can be obtained by combining the data for quantum yield, transmission of filters and detection efficiencies of the detectors. This way, $\gamma_{BG} = 0.74$, $\gamma_{GR} = 0.73$ and $\gamma_{BR} = 0.54$ is calculated for the discussed setup.

Anisotropy corrections Regarding anisotropy calculations, two corrections have to be considered. Different detection efficiencies in the parallel and perpendicular channels are accounted for by the factor G :

$$G_X = \frac{\eta_{X,\perp}^{\lambda_{em}^X}}{\eta_{X,\parallel}^{\lambda_{em}^X}} \quad (3.24)$$

Additionally, polarization mixing due to optical imperfections (i.e. due to refraction in the objective) is accounted for by the factors l_1 and l_2 (Koshioka et al., 1995; Schaffer et al., 1999). The corrected steady-state anisotropy for PIE channel XY is then given by:

$$r_{XY} = \frac{G_Y F_{XY,\parallel} - F_{XY,\perp}}{(1 - 3l_2) G_Y F_{XY,\parallel} + (2 - 3l_1) F_{XY,\perp}} \quad (3.25)$$

The G -factor can be determined from a dye measurement. Assuming accurate corrections, the residual anisotropy r_∞ for such a measurement should vanish. The measured residual

anisotropy is related to G by:

$$G = \frac{1 - r_\infty}{2r_\infty + 1} \quad (3.26)$$

The factors l_1 and l_2 can be determined from a dye measurement if lifetime and rotational correlation time are of similar magnitude. This can be achieved either by increasing the viscosity of the medium or by using a large molecule such as fluorescent proteins (see Koshioka et al., 1995).

FRET efficiency

The FRET efficiency definitions from section 2.4 have to be adjusted by inclusion of the γ -factors as follows, using the corrected photon counts defined before:

$$E_{GR} = \frac{F_{GR}}{F_{GR} + \gamma_{GR}F_{GG}} \quad (3.27)$$

$$E_{BG} = \frac{F_{BG}}{\gamma_{BG}F_{BB}(1 - E_{GR}) + F_{BG}} = \frac{\gamma_{GR}F_{BG}}{\gamma_{BR}F_{BB}(1 - E_{GR}) + \gamma_{BR}F_{BG}} \quad (3.28)$$

$$E_{BR} = \frac{F_{BR} - E_{GR}(\gamma_{GR}F_{BG} + F_{BR})}{\gamma_{BR}F_{BB} + F_{BR} - E_{GR}(\gamma_{BR}F_{BB} + \gamma_{GR}F_{BG} + F_{BR})} \quad (3.29)$$

Stoichiometry

The stoichiometry is a measure for the ratio of dyes within a molecule. For spFRET, the stoichiometry is defined as follows:

$$S_{GR} = \frac{F_{I,G}}{F_{I,G} + F_{I,R}} = \frac{\gamma_{GR}F_{GG} + F_{GR}}{\gamma_{GR}F_{GG} + F_{GR} + F_{RR}} \quad (3.30)$$

Here, $F_{I,X}$ denotes the total photon counts in all channels after excitation of dye X . For the three-color case, this definition is extended accordingly:

$$S_{BG} = \frac{F_{I,B}}{F_{I,B} + F_{I,G}} = \frac{\gamma_{BR}F_{BB} + \gamma_{GR}F_{BG} + F_{BR}}{\gamma_{BR}F_{BB} + \gamma_{GR}F_{BG} + F_{BR} + \gamma_{GR}F_{GG} + F_{GR}} \quad (3.31)$$

$$S_{BR} = \frac{F_{I,B}}{F_{I,B} + F_{I,R}} = \frac{\gamma_{BR}F_{BB} + \gamma_{GR}F_{BG} + F_{BR}}{\gamma_{BR}F_{BB} + \gamma_{GR}F_{BG} + F_{BR} + F_{RR}} \quad (3.32)$$

The three stoichiometries are related by the following equation:

$$1 - \frac{1}{S_{BR}} = \left(1 - \frac{1}{S_{BG}}\right) \left(1 - \frac{1}{S_{GR}}\right) \quad (3.33)$$

The stoichiometry is, when corrected by γ , only dependent on the absorption properties of the dyes as given by:

$$S_{XY} = \left(1 + \frac{\sigma_Y(\lambda_{ex}^Y)I_Y}{\sigma_X(\lambda_{ex}^X)I_X} \right)^{-1} \quad (3.34)$$

From the absorption properties of the dyes (see section 3.3) expected stoichiometry values can be calculated when equal excitation intensities are assumed: $S_{BG} = 0.27$, $S_{BR} = 0.23$ and $S_{GR} = 0.46$. The low value of S_{BG} was usually experimentally adjusted by maximizing the blue laser intensity (about 115 μW) while reducing the green laser intensity to 80 μW , which shifts the theoretical value to $S_{BG} = 0.34$. For optimized pulse sequences the stoichiometry S_{BR} is expected to be higher than the theoretical value presented here due to the already large photon loss in the red channel after red excitation (see section 4.1).

Fluorescence lifetime

Burstwise lifetime fitting has been shown to be most effective when applying a maximum likelihood estimator as opposed to the non-linear least-squares fitting method (Maus et al., 2001). In this work, only lifetimes of the channels BB, GG and RR were determined, as the fluorescence decay for the FRET channels is more complicated and doesn't contain additional information. However, implementation of a global lifetime of all PIE channels simultaneously has been shown to greatly improve the accuracy (Kudryavtsev et al., 2012). A single exponential model with a constant background fraction ξ is applied:

$$M(t; \tau, \xi) = (1 - \xi) \left[IRF(t) \otimes \exp\left(-\frac{t}{\tau}\right) \right] + \xi \quad (3.35)$$

Here, $IRF(t)$ is the instrument response function, γ is given by the background count rate and \otimes denotes the operation of convolution.

As stated before, the lifetime is related to the FRET efficiency by:

$$E = 1 - \frac{\tau_{D,A}}{\tau_{D,0}}$$

where $\tau_{D,A}$ and $\tau_{D,0}$ are the quenched and unquenched lifetimes of the donor. $\tau_{D,0}$ is accessible from the experiment as the lifetime of the donor-only species. This relation holds true only for static dye positions. Due to the flexibility of the linker however the relation has to be modified. Fast fluctuations of the dye position lead to sampling of different FRET states during a burst. Low FRET states will contribute more to the determined lifetime, because the obtained lifetimes from the MLE fit are not species weighted, but intensity weighted (Gansen et al., 2009). Usually, an empirical polynomial is used to convert species weighted lifetimes to intensity weighted lifetimes. For the dye pair Atto532-Atto647N, the relation then reads as:

$$E = 1 - \frac{-0.0421 + 0.5080\tau_{D,A} + 0.2691\tau_{D,A}^2 - 0.03589\tau_{D,A}^3}{\tau_{D,0}} \quad (3.36)$$

according to Kudryavtsev et al. (2012). However, the exact relation has to be reevaluated

for the specific dye pair used.

3.8.3 Separating Subspecies

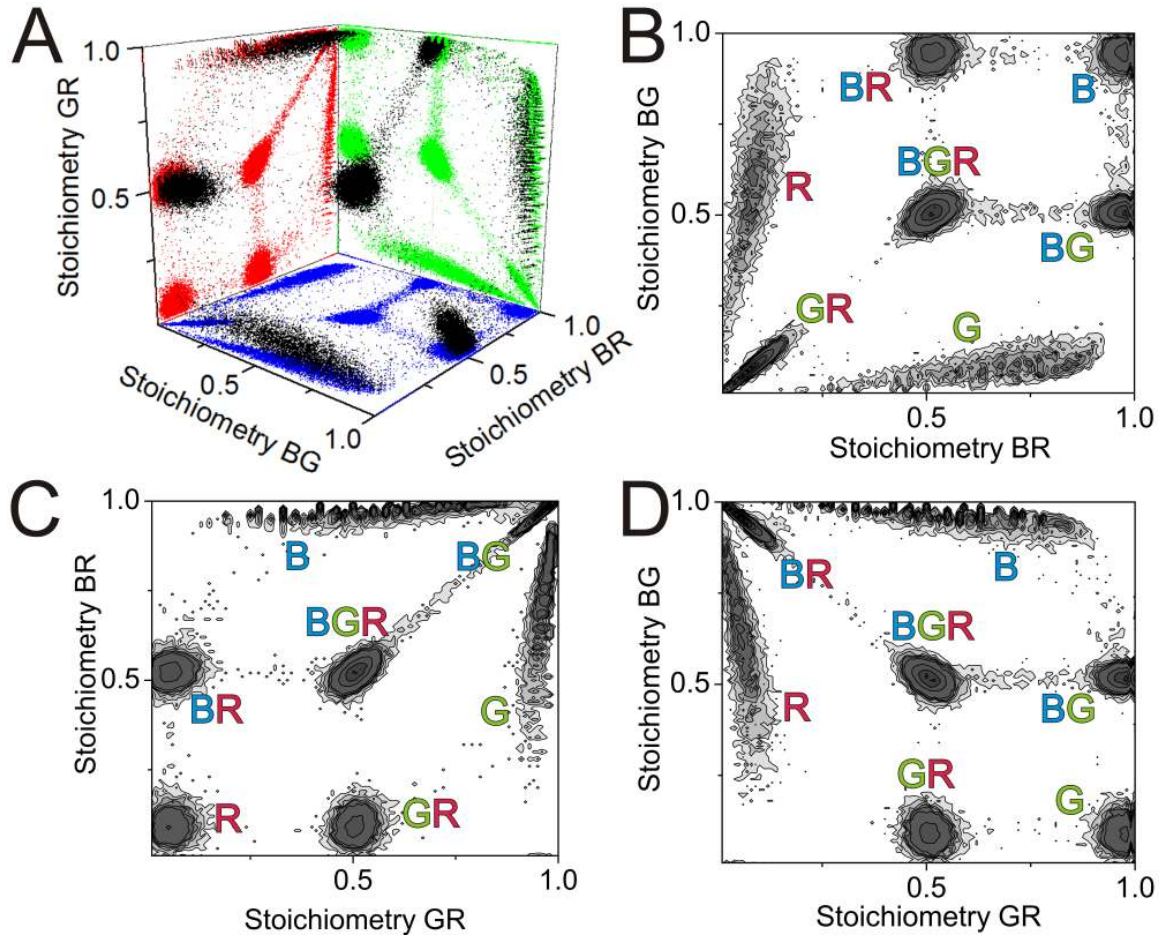


Figure 3.12: Monte-Carlo simulation of a three-color MFD experiment and corresponding 3D (A) and 2D (B-D) stoichiometry plots.

There are a total of 7 possible subspecies that can be distinguished on either 2D plot of two stoichiometries, as seen in figure 3.12. The theoretical stoichiometry values for each possible species are listed in table 3.2. The triple-labeled species is, ideally, located in the middle of every S-S-plot. double-labeled species always have a defined stoichiometry in every parameter space. Single labeled species, however, exhibit stochastically distributed values for those stoichiometries that are undefined for the respective dye. The slightly different positions for these wide distributions originate from the definitions of the stoichiometries as seen in equations 3.30 to 3.32. Assuming equal background levels in all PIE channels, the expected values are $S_{BG}^{R-only} = 0.8$, $S_{BR}^{G-only} = 0.75$ and $S_{GR}^{B-only} = 0.67$. Note that for every single labeled species, there is one S-S-plot where both stoichiometries are defined. Although double-labeled species always exhibit defined values for every stoichiometry parameter, they are best selected using the S-S-plot of the two stoichiometries that relate to the missing dye. Suppose the species GR

Species	Stoichiometry		
	BG	BR	GR
BGR	0.5	0.5	0.5
BG	0.5	1	1
BR	1	0.5	0
GR	0	0	0.5
B	1	1	/
G	0	/	1
R	/	0	0

Table 3.2: Stoichiometry values for the different species. “/” denotes that the stoichiometry is not defined in this case.

is of interest. Theoretically, the values for S_{GR} is expected to be 0.5. Experimentally, however, the width of the stoichiometry distribution may be large or the mean may be shifted to smaller or larger values, making accurate selection difficult. This is avoided if the plot of S_{BG} against S_{BR} is used to select the species, as here GR will be found at $S_{BG} = S_{BR} = 0$.

3.8.4 Data filtering

Careful and thorough filtering of the data obtained by MFD experiments is a necessity. In addition to separating the species of interest from incompletely labeled molecules or other contaminations by means of the stoichiometry, acceptor photobleaching as well as the occurrence of multi-molecule events will lower the quality of the obtained parameter distributions markedly. One approach to solve this problem has already been discussed in section 3.7 by refining the burst search algorithm. The extension of the APBS approach to each available channel in a PIE experiment (D/TCBS) has the natural advantage of only selecting those burst with all active fluorophores. However, photobleaching and multi-molecule events are, while reduced, not completely filtered out. Consider also that in a multitude of applications the sublabeled species are equally of interest.

Additional filters have been proposed. Eggeling et al. (2006) utilize the difference in the mean arrival time of photons in different channels. At single laser excitation, acceptor bleaching events can be identified by setting a maximum threshold on the time difference between the burstwise mean arrival times of the photons in the green channel and the FRET channel, $|T_{GG} - T_{GR}|$. While the described filter will remove bursts that contained bleaching events, it will also unwantedly remove FRET dynamics. This approach has been extended by Kudryavtsev et al. (2012) to the application of PIE-MFD. With the additional information of the presence of the red dye in PIE and ALEX, the same rationale can be applied to the difference in the mean arrival time between the photons after green excitation (that is donor and FRET photons) and the photons after red excitation $|T_{GX} - T_{RR}|$, allowing to distinguish bleaching events from FRET dynamics. Multi-molecule events are also detected by this filter if donor or acceptor only labeled species enter the volume. It will however fail if another double-labeled molecule

enters the volume, although, depending on the FRET state of the second molecule, the apparent FRET dynamics will be detected via $|T_{GG} - T_{GR}|$.

Another approach, introduced by Tomov et al. (2012), uses kernel density estimators to probe local photon densities and utilizes this statistical approach to detect FRET and brightness changes within single molecule bursts, in what they call two-channel kernel-density estimator (2CDE). Briefly, photon densities are estimated around each photon in a certain channel with respect to another channel by applying an exponential weight based on the difference in the arrival times. This way the FRET efficiency can be estimated around each individual photon of a burst for each channel (that is GG or GR) from the density of FRET photons and the density of donor photons. Consider the estimated FRET efficiency around donor photons, and a change from a high FRET state to a low FRET state within a burst. Periods of low FRET then have higher donor photon densities. When averaging the estimated FRET values around donor photons for the burst, the mean will then be biased towards low FRET values, or E will be underestimated. Similarly, if $(1 - E)$ is estimated based on the acceptor channel, periods of high FRET will contribute more to the average. Thus, the calculated value for $(1 - E)$ will also be underestimated. Consequently, for static FRET the two estimated efficiencies will sum up to one, but the sum will be less than one if dynamic changes happened during the burst ($FRET_{2CDE}$). Likewise, a distinction can be achieved for brightness variations within a burst ($ALEX_{2CDE}$). Average brightness ratios are estimated for the channels GX and RR, again based on photon densities around each individual photon. The static case converges to a fixed value, while a systematic deviation follows when brightness changes occurred within a burst. For convenience the obtained values are rescaled such that for the static case $FRET_{2CDE} = 10$, scaled to a maximum of 110, and such that $ALEX_{2CDE} = 0$ for the static case, scaling up to 100.

A comparison of the discussed filters for two-color MFD is given in figure 3.13. The raw data (A) shows significant amount of acceptor photobleaching and multi-molecule events which form a “bridge” between the double-labeled species and the donor only population. The individual filter parameters have been chosen such that the remaining number of double-labeled bursts (defined by $0.2 < S < 0.8$) after filtering is equivalent to the number of bursts detected using DCBS (about 16.000 events). Application of either filter (B-D) reduces the number of bridge events by a comparable amount. The advantage (or disadvantage, depending on the type of application) of 2CDE and DCBS is that donor-only and acceptor-only bursts are automatically removed. While in the presented example separation of the species of interest by means of stoichiometry is trivial, there may arise situations where the stoichiometry is shifted to higher or lower values and thus closer to donor-only or acceptor-only populations. This may be caused either by large difference in the excitation properties of the dyes, or occur naturally when complexes with higher order stoichiometries are studied. The dual-channel burst search algorithm additionally reveals a low-FRET species, which is partly removed by application of either filter.

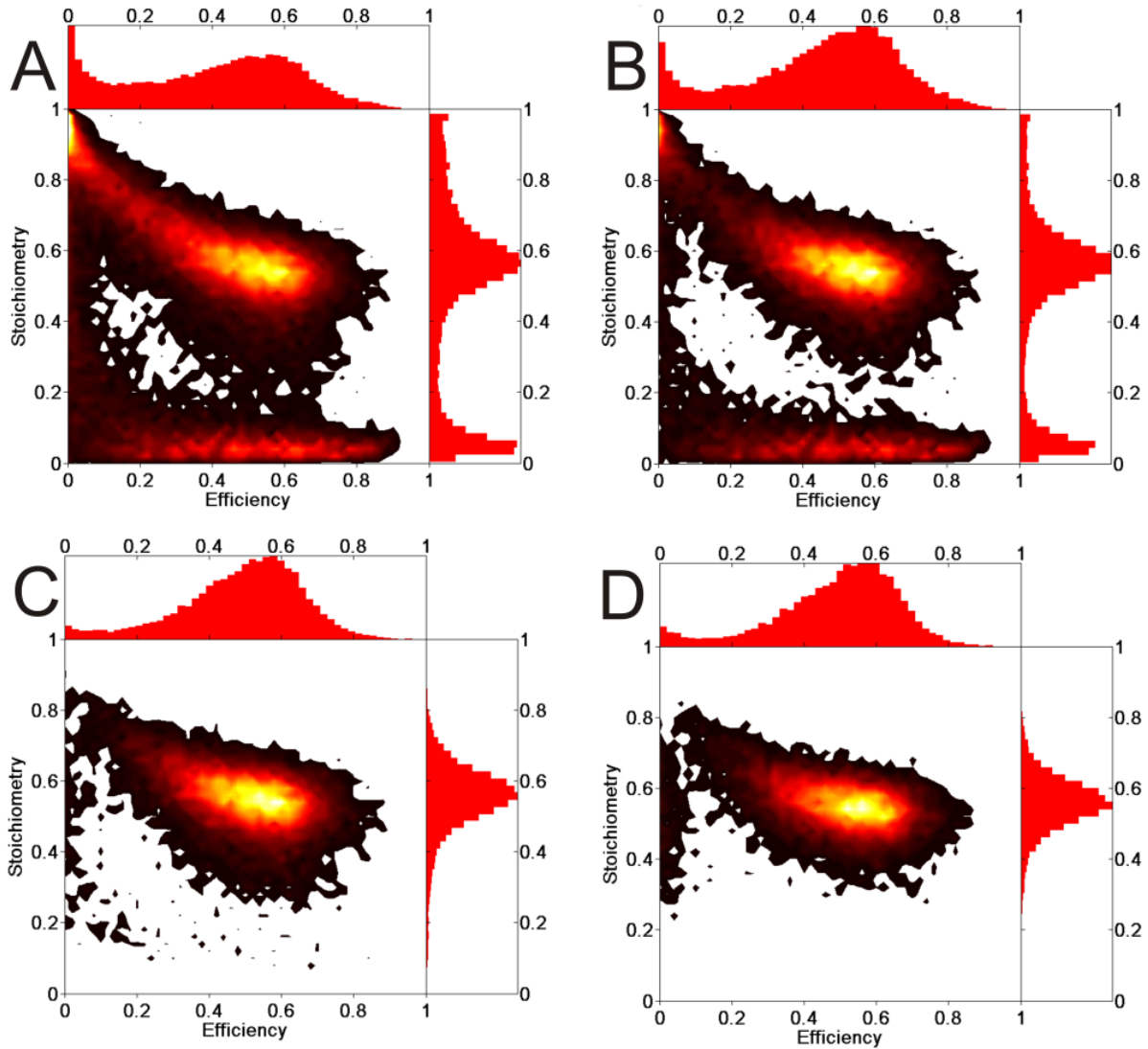


Figure 3.13: Comparison of different filters to remove photobleaching and multi-molecule events. A) APBS with parameters $L=100$, $M=20$ and $T=500 \mu\text{s}$. A total number of 32761 bursts was collected. B) Same data after $|T_{GX} - T_{RR}| < 0.2 \text{ ms}$ has been applied. The total number of bursts is reduced to 22729. For $0.2 < S < 0.8$ the number of bursts is 16088. C) Same data as A after applying $ALEX_{2CDE} < 10$. The number of bursts is 16637. D) DCBS with parameters $L=100$, $T = 500 \mu\text{s}$ and $M=10$ for either channel. The number of bursts is 16363.

Extension of data filtering methods for three color PIE-MFD

The rationale for both presented filters can be extended to three colors. The mean macrotime filter can simply be applied to all combinations of the three available channels, that is detection after excitation of each dye ($|T_{BX} - T_{GX}|$, $|T_{BX} - T_{RR}|$ and $|T_{GX} - T_{RR}|$). Filtering by these three parameters allows for efficient removal of all possible bleaching events. Similarly, the detection of brightness variations by the 2CDE filter can also be applied to all combinations of the available channels. To detect FRET dynamics, the proximity ratios can be used to probe variations. These will, however, not exclusively detect dynamics between the two dyes. When only considering the proximity ratio, a FRET change between the green and red dye will be detected

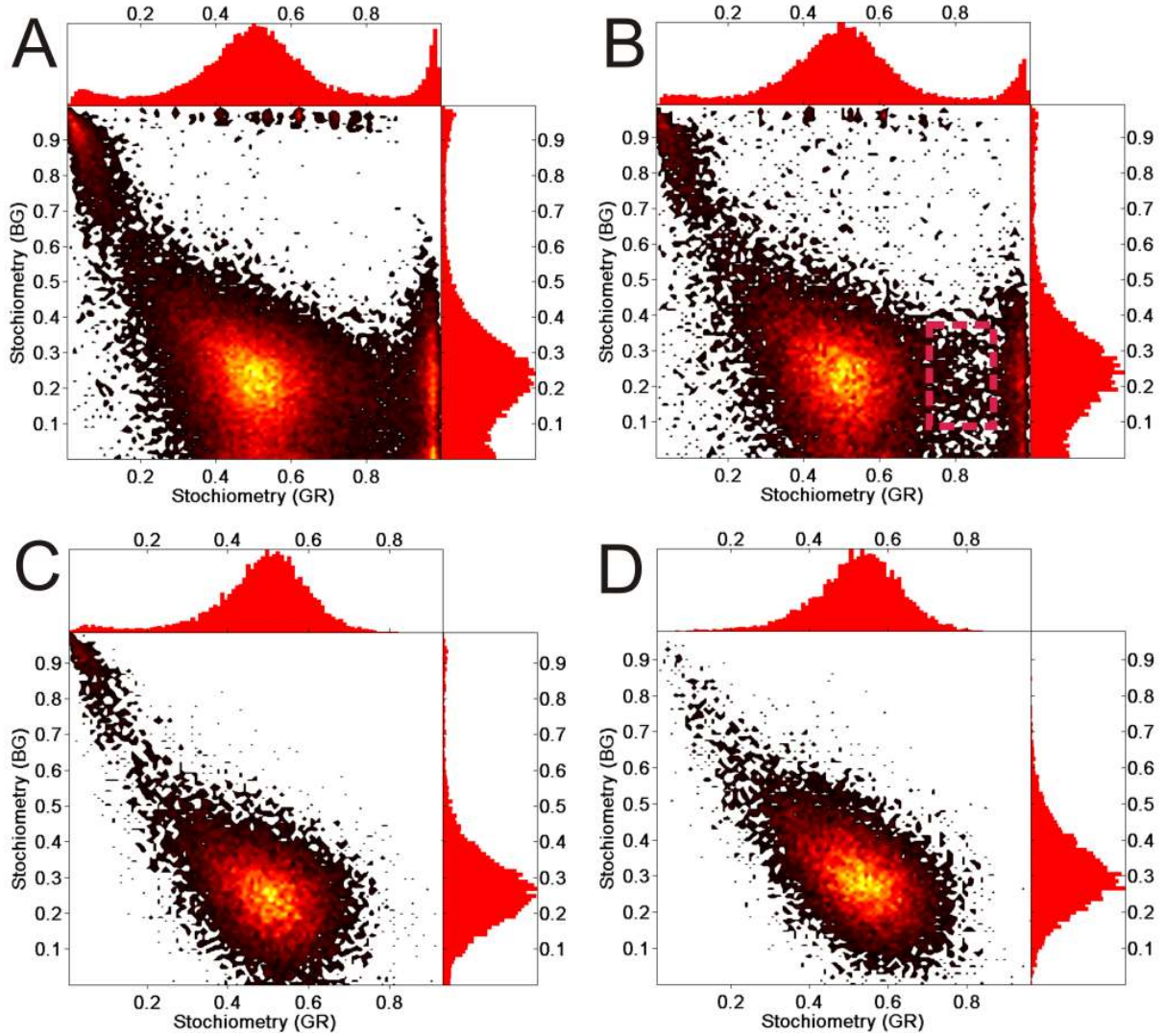


Figure 3.14: Comparison of different filters to remove photobleaching and multi-molecule events for a three-color measurement. Only stoichiometries are compared to show the influence of the different filters in this case. A) APBS with parameters $L=50$, $M=60$ and $T=500 \mu\text{s}$. A total number of 49042 bursts was collected. B) Same data after $|T_{BX} - T_{RR}| < 0.12 \text{ ms}$, $|T_{BX} - T_{GX}| < 0.12 \text{ ms}$ and $|T_{GX} - T_{RR}| < 0.12 \text{ ms}$ has been applied. The total number of bursts is reduced to 19532. For $0.2 < S_{GR} < 0.8$ and $0.1 < S_{BG} < 0.8$ the number of bursts is 13760. The red box highlights the decrease in bridge events. C) Same data as A after applying the $ALEX_{2CDE}^{BG} < 6$, $ALEX_{2CDE}^{BR} < 6$ and $ALEX_{2CDE}^{GR} < 6$. The number of bursts is 12562. D) TCBS with parameters $L=100$, $T = 500 \mu\text{s}$ and $M=20$ for either channel. The number of bursts is 13246.

as FRET dynamics when comparing the blue and red channels, as well as when comparing the blue and green channels. Thus, dynamics of the whole system will be detected by applying the 2CDE methodology to the proximity ratios between the blue dye and either the green or red dye. Likewise, the mean macrotime filter can be applied to detect FRET dynamics of the whole system using the differences in mean macrotime between the respective channels after blue excitation as $|T_{BB} - T_{BG}|$, $|T_{BB} - T_{BR}|$ and, as before, $|T_{GG} - T_{GR}|$. A comparison of the different

filters and the triple channel burst search is shown in figure 3.14 by means of the stoichiometry plot of S_{BG} versus S_{GR} . As for the two-color example discussed before, photobleaching and multi-molecule events again appear between the populations as “bridge” events. In this case, not the removal of acceptor photobleaching and multi-molecule events is addressed, but the influence of the filtering on the SS-plot is compared. The laser intensities have been chosen such that S_{BG} will be low and thus the triple-labeled subspecies will be close to the subspecies which only carries a green and red label. The raw data (A) show the different subspecies as discussed in the previous section. Again, the filter parameters are chosen such that the number of bursts remaining for $0.1 < S_{BG} < 0.8$ and $0.2 < S_{GR} < 0.8$ is comparable to the amount of bursts detected by TCBS. Application of the mean macrotime filter removes photobleaching events as can especially be seen for the decrease in bridge events between the triple-labeled subpopulation and the subpopulation with only a blue and green label (red square). However, clear separation of the species BGR and GR is still not possible. The 2CDE filter efficiently removes sublabeled species, however, a small part of BR labeled molecules still remains (population in the top left), which is easily separated from the triple-labeled population. TCBS only detects triple-labeled species, obtaining a clean SS-plot and enabling FRET analysis that is independent of the exact boundaries set for the selection of species via stoichiometries.

Species selection by the 2CDE methodology

Analogously to the demonstrated possibility to separate the triple-labeled species by use of the $ALEX_{2CDE}$ filter, sublabeled species can be isolated even for the case of considerable overlap between the population in the stoichiometry-stoichiometry plot. For the channel corresponding to the missing dye, large intensity fluctuations will be recorded. Thus, the respective $ALEX_{2CDE}$ values will be large, while the brightness ratio of the present dyes will show little to no fluctuations. Consider that the species BG is of interest. Efficient separation is then achieved by setting the thresholds $ALEX_{2CDE}^{BG} < 10$, $ALEX_{2CDE}^{BR} > min$ and $ALEX_{2CDE}^{GR} > min$, where the value min has to be chosen individually ($min \approx 20 - 40$).

Summary

Of the two filters discussed here, the 2CDE methodology is preferred. It offers equivalent performance and the benefit of donor- and acceptor-only species removal, while being minimally influenced by variations in burst duration, photon number and brightness. Only when sublabeled species are of interest, is the application of the mean macrotime based filter recommended. Even then, subspecies selection in three-color MFD is best performed by the 2CDE filter, which offers removal of artifacts in conjunction with species selection. If sublabeled species are not relevant to the analysis, the advanced burst search algorithms should be used. The advantage of D/TCBS over the filtering methods is that burst exhibiting photobleaching, blinking or multi-molecule events are preserved instead of being discarded. As discussed before

(see section 3.7), in D/TCBS the correct FRET efficiency is retained for both photobleaching and blinking events. Only multi-molecule events result in a distortion of the obtained FRET efficiency distribution. Subsequent application of the 2CDE filter to D/TCBS data will additionally remove this contribution. Thus, the recommended procedure to obtain artifact-free parameter distributions is D/TCBS in combination with filtering by $ALEX_{2CDE}$.

3.9 Simulation of multicolor FRET

A simple Monte-Carlo approach is used for providing the simulated data shown in this work (see figure 3.12 on page 45). The photophysical system is described by means of lifetime and quantum yield of the dyes as well as Förster radii and assumed static distances between the dyes. Additionally, a photobleaching rate is included. Based on these parameters the probabilities for the possible outcomes (no fluorescence, fluorescence of either dye, bleaching of either dye) are calculated and a random number of the interval $[0, 1]$ is drawn to decide the result. For simplicity, the excitation probability is taken as 1. At this moment, a system of a maximum of four dyes can be simulated by this means. For PIE excitation, or for the event of bleaching of one dye, probabilities are recalculated based on the reduced system. To simulate an intensity trace for a single molecule (as for example the case in TIRF or confocal measurements of immobilized single molecules) a fixed time bin is set and a number of excitation cycles, given by the excitation rate and the bin width, is performed. Background counts are added following a Poissonian distribution. For burst experiments a Gaussian distribution of burst durations is generated based on a given mean and standard deviation, determining the number of excitation cycles per burst. Additionally, labeling efficiencies are taken into account and probabilities for every differently labeled species are calculated. The labeling for every burst is again randomly determined. A simulation of stoichiometry distributions for three-color PIE-MFD is shown in figure 3.12 on page 45.

While these simulations describe shot noise limited distributions of parameters and include photobleaching events, other contributions to the broadening of distributions are at this moment not included. Diffusion of molecules through the confocal volume has to be taken into account to accurately simulate real experiments and to allow for the theoretical comparison of different burst search algorithms. Using this approach, also concentration related effects such as multi-molecule events are naturally included in the simulation. Additionally, inclusion of dynamically interchanging FRET states would increase the applicability of the simulations to complex situations. Lastly, accounting for polarization effects and a full simulation of the microtimes of photon arrivals to determine the accuracy of lifetime fitting would ultimately allow for a complete simulation of MFD experiments.

3.10 Background in fluorescence measurements

For sensitive MFD measurements, it is essential that background levels are kept low. There are multiple sources of background. Thermal noise of the detector is specific for the instrument and modules optimized for low dark counts are available. Additional cooling can further reduce the dark counts of the detector. The contribution of thermal noise is usually < 100 counts per second. If the sensitive area of an APD is not effectively shielded from stray light, uncorrelated background noise will be high. Good shielding of the detection pathway from stray light will reduce this contribution. Another source of background is Rayleigh scattering of the laser light from the sample. Scattering is an instantaneous process and the scattered light will be seen at the position of the laser pulse in the microtime histogram. Rayleigh scattering from molecules (e.g. water) is strongest for shorter wavelengths, which is why scatter background is most intense in the blue detection channel. Additionally, reflections in the optical path can be the source of background, which is usually easily identified in the microtime histogram. As an example, the second peak in the microtime histogram shown in figure 3.17, right, at 2.5 ns most likely originates from a reflection of the intense scattering peak between the detector and the backside of the pinhole. Another possible background contribution is auto-fluorescence of dichroics, filters or other optical components. When choosing emission filters for fluorescence measurements, it should always be ensured that the filters block the individual laser lines sufficiently (at least OD 6 is recommended). When using buffers, fluorescent background from impurities also has to be considered. A buffer-only measurement can be used to characterize this background contribution.

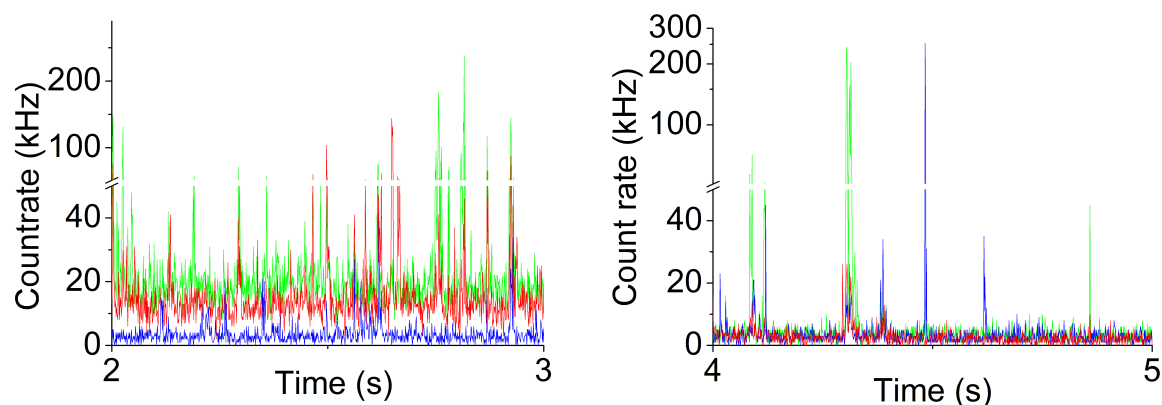


Figure 3.15: Time traces with 1 ms bin width of a three-color burst measurement of triple-labeled DNA with (left) and without (right) Raman scattering. See section 4.2.2 for details on the measurement.

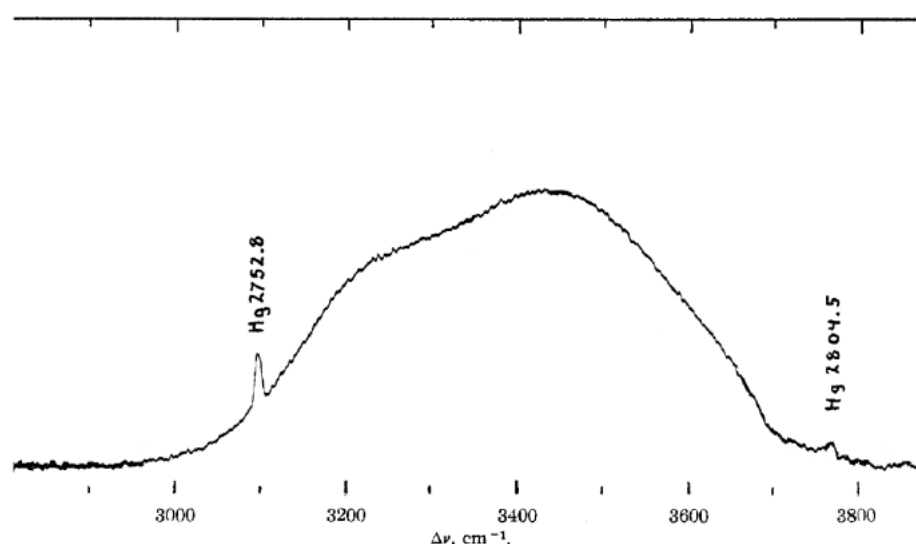


Figure 3.16: Raman spectrum of water at 26 °C. Adapted from Cross et al. (1937).

3.10.1 Raman scattering

Another background contribution that has to be considered is Raman scattering. The process can be understood in a simplified way as follows: A molecule absorbs a photon and is excited into a virtual state. From this state it can either relax back to the ground state by emission of a photon, in which case the wavelength of the emitted photon is unchanged with respect to the absorbed photon (Rayleigh scattering), or relax to an excited vibrational state of the ground state, in which case the wavelength of the emitted photon will be larger (Stokes scattering). Additionally, if the molecule was in an excited vibrational state at the start, relaxation can lead to the emission of a photon with a shorter wavelength (anti-Stokes scattering). This process, however, is rare since higher vibrational states are usually not populated at room temperature. The shift of the Stokes scattering is determined by the vibrational spectrum of water. Figure 3.16 shows the Raman spectrum of water which stretches from 3200–3600 cm^{-1} . As the Raman shift occurs at a fixed energy, both the width and the absolute position of the Raman scattering peak will depend on the excitation wavelength. Because of the inverse relation between energy and wavelength, the Raman peak will be shifted less (in terms of wavelength) and be narrower for lower excitation wavelengths. The position of the Raman scatter as given by the excitation wavelength can be determined, given the excitation wavelength λ_{ex} in nm and the Raman shift $\tilde{\nu}$ in cm^{-1} by:

$$\lambda_R = 10^9 \left(\frac{10^9}{\lambda_{ex}} - 100 \cdot \tilde{\nu} \right)^{-1} \quad (3.37)$$

Table 3.3 lists the position of the Raman scatter signal at relevant excitation wavelengths. It is evident why in conventional spFRET measurements, where usually a green laser (e.g. 532 nm) and a red laser (around 635 nm) is used in conjunction with established dye pairs such

λ_{ex}	Raman scattering
480 nm	570-580 nm
565 nm	690-710 nm
532 nm	640-660 nm

Table 3.3: Position of Raman scattering for a number of excitation wavelengths.

as Cy3-Cy5 or Atto532-Atto647N, Raman scattering is not encountered. Here the emission of the red dye is usually detected from 670 nm upwards and Raman scattering is avoided. In the case of the three-color setup presented here however, it appeared that the Raman lines were not blocked by the filters that were initially chosen. The resulting high background in the green channel after blue excitation, as well as in the red channel after green excitation, exceeds count rates of 10 kHz. Figure 3.15 compares time traces of a three-color burst measurement with and without Raman background. Obviously, burst selection is difficult at such high background levels. Although the spikes are still markedly higher than the constant background, the blue signal can become insignificant compared to background levels for high FRET species as presented here and the burst selection will become insensitive with respect to the blue signal. Adding to this, the background contribution of scatter even during bursts is very large, as can be seen from figure 3.17. Raman scattering intensity is proportional to λ^{-4} , so it is more intense at lower wavelengths.

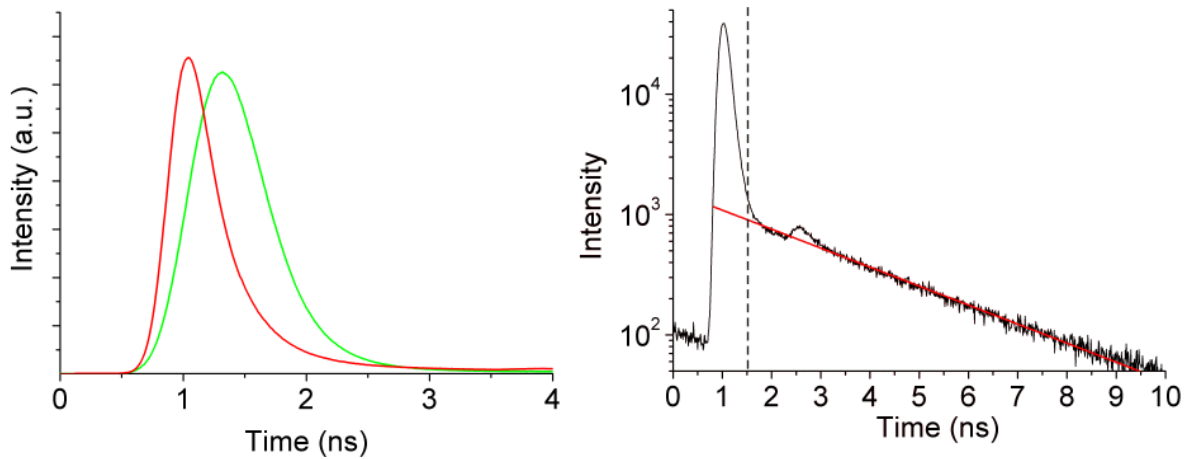


Figure 3.17: (Left) Raman scattering peaks in the green channel after blue excitation (green) and in the red channel after green excitation (red). FWHM is 1 ns for the green channel and 600 ps for the red channel. (Right) Cumulative microtime histogram of channel GR generated from extracted bursts. The red line is a single exponential fit to the tail of the decay. The second peak at 2.5 ns is caused by a reflection of the intense scatter signal in the detection pathway.

3.10.2 Removal of Raman background

Microtime Gating

Since Raman scattering is an instantaneous process, it will appear at quasi zero time delay relative to the laser pulse position in the microtime histogram (figure 3.17, left). Lifetime gating the recorded signal by only counting those photons with higher microtimes than the threshold as indicated by the dashed line, can thus be used to eliminate the scatter contribution (as has been applied by Zarrabi et al. 2009). However, also a good proportion of the fluorescence signal is discarded this way. The Raman scatter peaks are shown in figure 3.17, left. For the red channel the full width at half maximum (FWHM) is approximately 600 ps. Using the parameters extracted from the fluorescence decay as seen in the microtime histogram in figure 3.17 (assuming a mono-exponential decay, red curve), discarding the first 600 ps equals to a loss of about 20% of the fluorescence signal. For the green channel the FWHM is even larger at 1 ns, and the loss will be more severe. Consider also that this photon loss will be biased towards species with small lifetimes, effectively making the detection efficiency dependent on the lifetime. In reality, the decay of the FRET signal will not be mono-exponential. Rather, it is given by (Kudryavtsev et al., 2012):

$$F_{FRET}(t) \propto \frac{E}{\tau_A - \tau_{D,A}} \left[\exp\left(-\frac{t}{\tau_A}\right) - \exp\left(-\frac{t}{\tau_{D,A}}\right) \right] \quad (3.38)$$

Here, τ_A is the acceptor lifetime and $\tau_{D,A}$ is the donor lifetime in the presence of the acceptor. The donor is quenched by the acceptor dye according to:

$$\tau_{D,A} = \tau_{D,0}(1 - E) \quad (3.39)$$

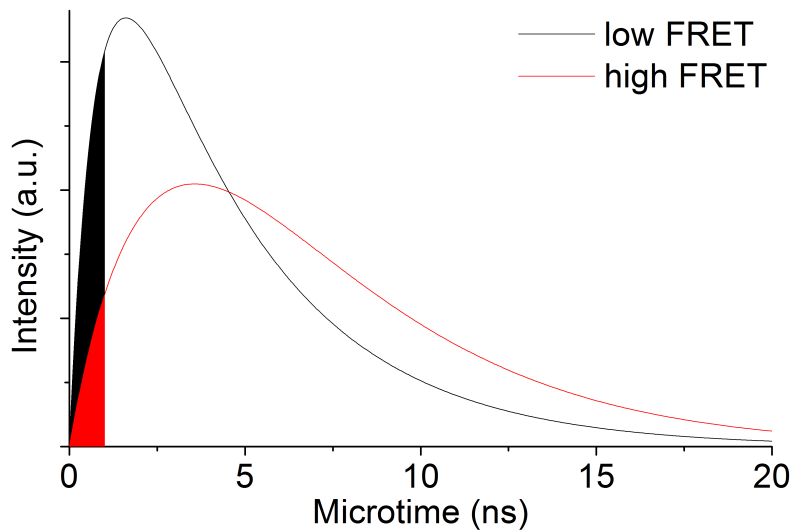


Figure 3.18: Calculated intensity decays of the FRET signal for $E=0.2$ and $E=0.8$. The colored regions indicate the lost signal if the first nanosecond is discarded.

The theoretical decays of the FRET signal are plotted for $E=0.2$ and $E=0.8$ in figure 3.18, assuming equal lifetime of 4 ns for donor and acceptor. For these theoretical decays the signal loss by discarding the first nanosecond is 10.3% for $E=0.8$ and 3.5% for $E=0.2$. The dependence of detection efficiency on the FRET efficiency makes accurate FRET measurements of multiple species difficult.

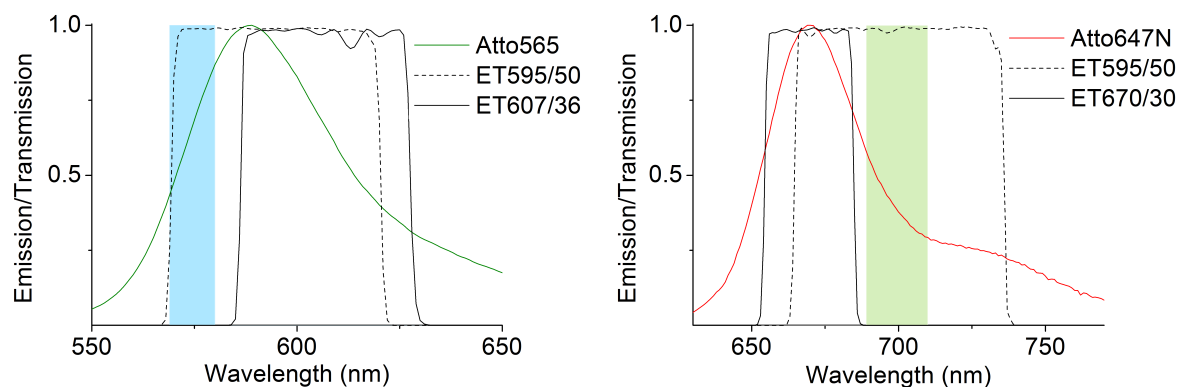


Figure 3.19: Normalized emission spectra of the dyes and transmission spectra of the filters. The shaded range indicates the presumed position of the Raman signal.

Adjusting the emission filters

Initially, emission filters were chosen to optimize the spectral overlap with the emission spectrum of the dyes and the selection was ultimately only limited by the requirement to block the laser lines with at least OD 6. These filters did however not block the Raman scattering (see figure 3.19). For the green channel the Raman scattering occurs at the lower end of the emission spectrum. Thus adjusting the filter to higher wavelengths removes the background contribution, but lowers the signal levels to 80%. For the red channel, the Raman scattering does unfortunately appear in the middle of the emission spectrum, so that the higher part of the emission spectrum has to be discarded. Moving to shorter wavelengths helps to reduce the photon loss, and the resulting signal is reduced to 75%.

Summary

When deciding on how to remove the Raman background, several factors have to be considered. Experimentally, the loss in the fluorescence signal is estimated to be similar for microtime gating versus changing the emission filters. The theoretical calculations of the loss due to microtime gating indicate that the actual loss in fluorescence signal may be quite a bit lower (10% at $E=0.8$ versus a loss of 20% for a change of filter) due to the fact that the FRET signal is significantly delayed with regard to the laser pulse. Thus in principle microtime gating should be the preferred method. It can however not be applied for accurate FRET measurements of multiple species because of the dependence of the detection efficiency on the FRET efficiency.

Furthermore, higher background count rates introduce artifacts related to the detection electronics. The time-to-amplitude converter can only register one photon per cycle. Thus at higher background count rates more fluorescence photons will be missed (see section 4.1.3), resulting in a decreased detection efficiency. Additionally, pile-up of the fluorescence signal occurs for the same reason: If a first photon is recorded at the start of the TAC period, no additional photon can be detected for the rest of the microtime. Since the scatter occurs at the start of the microtime and is intense, the detection efficiency of fluorescence photons is further lowered and will be biased more towards low microtimes, thus also systematically lowering the determined lifetime. Practically, the data size can also be a limiting factor. With count rates of >10 kHz (compared to usual count rates for burst experiments of 1-3 kHz), files quickly reach sizes of 1 GB over the course of an hour. While this limitation can be overcome by splitting files into smaller pieces or by combining subsequent measurements, it still increases the effort to analyze data. Because of these reasons application of narrower emission filters is preferred here.

4 Results

4.1 Duty-cycle optimized PIE (DCO-PIE)

For spFRET PIE-MFD measurements usually a pulse sequence of 1:1 for donor and acceptor excitation pulse is used. Direct extension of this pulse sequence to three colors would apply a pulse sequence $[bgr]_n$. However, the yellow/green laser used in this work operates at a fixed frequency of ~ 27.4 MHz, corresponding to a repetition period of ~ 36.5 ns. Considering fluorescence lifetimes of the unquenched dyes of up to 4 ns, application of this time period would cause temporal crosstalk, that is the fluorescence signal of the dyes would not have decayed sufficiently before the next excitation pulse occurs. Considering the given repetition period and a lifetime of 4 ns for all dyes, the expected amount of temporal crosstalk would be of the order of 5%. Moreover, the exact amount is effected by quenching of the dyes, making accurate corrections difficult. Thus, initially, a pulse sequence of $[bgrg]_n$ as seen in figure 4.1, left, was used. Applying this excitation scheme however reduces the time exciting the blue dye (in the following called “duty time”) to 25%. The blue excitation is most deciding for accurate determination of all FRET efficiencies of the three-dye system. The green excitation pulse probes the FRET between the green and red dye and is also essential to determine the other two FRET efficiencies. As discussed in section 2.4, shot-noise related broadening of the distribution of the FRET efficiency from the green to the red dye should also be kept minimal, as its width propagates to all other determined FRET efficiencies. The direct excitation of the red dye is usually only used to probe its presence. Red photon counts can thus be sacrificed if anisotropy or lifetime of the red fluorophore are not of special interest. Consequently, the excitation scheme was optimized by increasing the ratio of blue to red pulses (see figure 4.1). This way the duty time of the blue excitation is increased at the cost of the red excitation, while the duty time of the green excitation is kept constant due to the instrumental constraint.

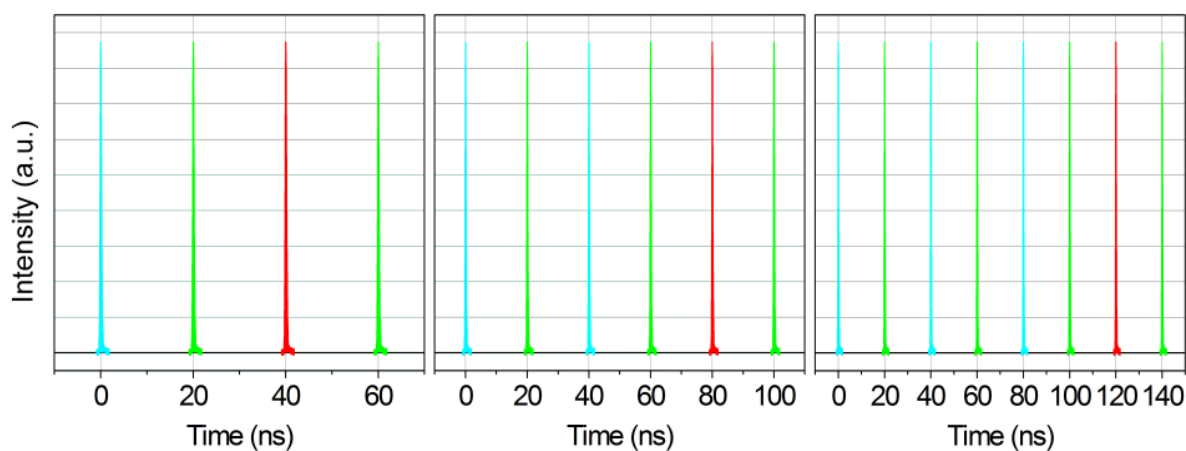


Figure 4.1: Pulse sequences for 1, 2 and 3 blue pulses. Adapted from (Hendrix and Lamb, 2013).

The idea of duty-cycle optimized pulse sequences was originally introduced by Zarrabi et al. (2009), termed DCO-ALEX. Using the fluorescent protein EGFP as the donor dye, the obtained signal was optimized by increasing the duty time of excitation. Considering the fast saturation and overall unfavorable properties of fluorescent proteins for quantitative FRET measurements, this result is expected. In the following, the performance of duty-cycle optimized PIE is evaluated when applied to a system of dyes with already very good fluorescent properties. The optimization will be given as the number of blue pulses within the pulse scheme.

4.1.1 Considerations when applying duty-cycle optimized pulse sequences

Gain in the blue channel

A simple treatment of the effect of the duty-cycle optimized pulse scheme on the detected number of photons may describe the optimization purely due to the increase in intensity, neglecting effects of saturation and photobleaching. At constant energy per pulse, the intensity will scale with the number of blue pulses N in a pulse sequence of $2(N + 1)$ total pulses (N blue, $N + 1$ green and one red pulse). To describe the relative increase, the case $N = 1$ is set as a reference. The relative gain due to the change in intensity is then given by:

$$G(N) = \frac{2N}{N+1} \quad (4.1)$$

This function is plotted in figure 4.2, together with measured relative count rates. The relative gain when increasing the pulse sequence by one blue pulse, as plotted in 4.2 (right), is then given by:

$$G_{rel}(N) = \frac{G(N)}{G(N-1)} - 1 = \frac{1}{(N+1)(N-1)} \quad (4.2)$$

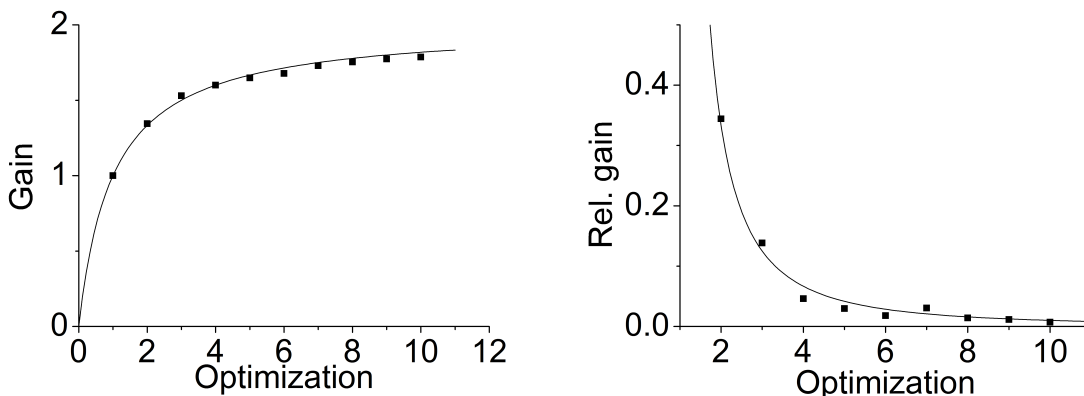


Figure 4.2: Effect of duty-cycle optimization, given as the number of blue pulses per cycle. Measurement on a nM solution of Atto488. (Left) Gain is given as relative count rate for the measured data points. The solid curve is given by equation 4.1. (Right) Relative gain when increasing the number of blue pulses by one.

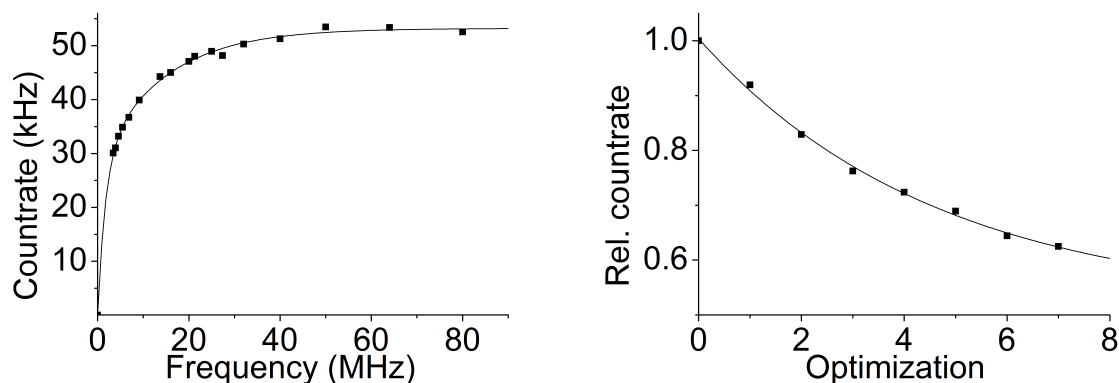


Figure 4.3: Influence of pulse optimization on the signal in the red channel. (Left) Signal from a nM solution of Atto655 at constant laser power and varying excitation rates. (Right) The same data rescaled to the frequencies realized by pulse optimization and normalized to the first data point.

Loss in the red channel

Duty-cycle optimized pulse sequences achieve an increase in signal after blue excitation by sacrificing signal after red excitation. While this loss can partly be reduced by increasing the laser power, the signal levels are ultimately limited by the excitation rate and will decline if the frequency is reduced. Figure 4.3 shows the decrease in signal with decreasing excitation rate. For the case of a pulse sequence with three blue and one red pulse, the frequency of the red laser is reduced to one fourth of the original frequency (27.4 MHz to 6.85 MHz). At this frequency the signal has already dropped by close to 25%.

Choosing the right pulse sequence

When deciding on a pulse sequence, several factors have to be considered. As can be seen from Figure 4.2, right, the relative gain achieved by duty-cycle optimization is significant for low number of blue pulses ($N \leq 4$), but diminishes when moving to higher numbers (relative gain of less than 5% for $N > 4$). In the same manner, the relative loss in the red channel is high first, but decreases when moving to larger numbers of blue pulses (see figure 4.3, right). By multiplying the gain in the blue channel with the loss in the red channel, a measure for the total performance can be defined (figure 4.4, left). A maximum is found for $N = 3$, although for all considered sequences the gain in the blue channel still outweighs the loss in the red channel. Judging from this data, pulse sequences of $N = 3$ and 4 are favorable, whereat the difference is a gain of about 5% in the blue channel and a loss of about 4% in the red channel. In this work, mostly pulse sequences with three blue pulses have been used.

In general, when choosing a pulse sequence, several things have to be considered: If the aim is to determine accurate FRET efficiencies for three-color FRET, the blue and green laser

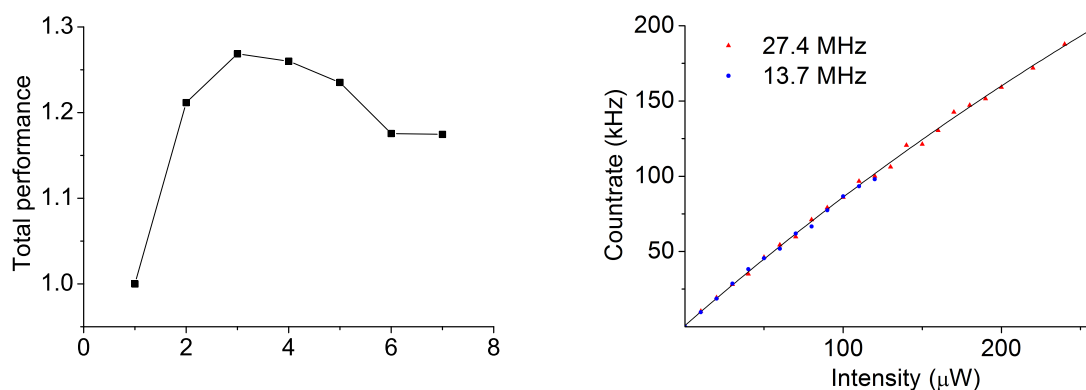


Figure 4.4: (Left) Total performance of pulse sequences, considering both the gain in the blue channel and the loss in the red channel. The optimization is given as the number of blue pulses per cycle. (Right) Saturation curves of a nM solution of Atto488 at the lowest and highest frequency achievable by duty-cycle optimized PIE. The solid line is a fit to the data at 27.4 MHz.

duty times should be optimized at the cost of the red signal. On the contrary, if anisotropy or lifetime of the red dye are of special interest, sufficient signal levels in the red channel should be ensured. If the blue dye is solely used as a reporter for the binding of an interaction partner, while the FRET between the green and red dye is monitored, the pulse sequence can be adjusted accordingly by e.g. applying a sequence of $[bgrg]_n$.

Saturation

At high laser powers saturation occurs. It is important to note here that, while similar in effect, the “classical” saturation observed in ensemble experiments with continuous wave (cw) excitation has to be distinguished from the saturation observed in single molecule experiments with pulsed laser. In the first case, saturation occurs because the excited dyes spend a nonzero time in the excited state. At cw excitation with high laser powers this leads to depletion of the ground state, such that the signal does not increase linearly with power anymore. For pulsed excitation however, there is usually enough time for all the excited molecules to return to their ground state before the next excitation pulse occurs. With increasing intensity per pulse, the probability of excitation per pulse increases as well. Signal rates are however ultimately still limited by the repetition rate of the exciting laser, which again leads to a nonlinear increase of the signal at high laser powers. In both cases, the signal saturates. However, the curves are not identical. Another effect leading to the saturation of the signal is the population of triplet or dark state, which is found to be higher for pulsed excitation (Gregor et al., 2005; Eggeling et al., 2006).

Signal levels with pulsed excitation are thus limited by the frequency of the excitation laser, and lower frequency excitation leads to earlier saturation. In theory, signal levels should be higher when applying optimized pulse sequences (and hereby increasing the excitation fre-

quency). However, for the available blue laser powers this effect was not observed, as seen in figure 4.4, right. Albeit this effect will certainly play a role at higher laser powers (200 μW and more), it is questionable if these laser powers are still suitable for single molecule measurements, as bleaching will be enhanced likewise.

Photobleaching

Photobleaching in single molecule FRET experiments with pulsed excitation has previously been studied by Kong et al. (2007) and Eggeling et al. (2006). Both studies conclude that in SM FRET studies bleaching of the donor fluorophore is usually not a problem. The same applies to direct excitation of the red dye as applied in PIE and ALEX. Kong et al. however show that acceptor bleaching scales both with the laser power of the donor exciting laser and the FRET efficiency between the two dyes for both pulsed and cw excitation. In a pump-probe like experiment where the delay between between the donor and acceptor exciting laser pulse is varied, they find that acceptor photobleaching is strongest if the donor excitation happens shortly (that is relative to the lifetime of the acceptor) after acceptor excitation. If, however, the acceptor exciting pulse is situated after the donor pulse, no increased bleaching is observed. They conclude that bleaching occurs if the acceptor in the excited state absorbs a donor excitation photon. This train of events excites the acceptor to higher singlet or triplet states, where bleaching is likely. For pulsed donor excitation, the reasoning is that (a) shorter pulses and (b) less photon density per pulse should both reduce acceptor photobleaching. While the pulse width is usually fixed, optimized pulse sequences allow to lower the power per pulse for the donor exciting laser, and should thus reduce artifacts due to acceptor photobleaching. However, no experimental evidence can be presented as of yet.

4.1.2 Effect of duty-cycle optimization in burst analysis

In addition to the ensemble dye experiments mentioned in the previous section, the effect of duty-cycle optimization has also been studied by burst analysis. For this, a triple-labeled DNA with FRET between all dyes was measured with different pulse sequences. The power was set to $70 \mu\text{W}$ for the blue laser and to $100 \mu\text{W}$ for the other two lasers at a pulse sequence of bgrg and the power per pulse was kept constant for all measurements. Consequently, the laser power for the different pulse sequences varied with the change in duty time for the respective laser. For a total number of 8 blue pulses per sequence, i.e. $[(\text{bg})_8\text{rg}]_n$, the power is then $124 \mu\text{W}$ for the blue laser and $22 \mu\text{W}$ for the red laser, while the green laser power is unchanged. Figure 4.5 (left) shows the area normalized distribution of photons per burst after blue excitation (BX) for the pulse sequences bgrg (1:1), $[(\text{bg})_2\text{rg}]_n$ (2:1) and $[(\text{bg})_3\text{rg}]_n$ (3:1). triple-labeled species were selected via stoichiometry as described in section 3.8.3 and the minimum number of photons per burst was set to 100. The right graph shows mean values in the PIE channels BB, BG and BR, normalized to the number of photons obtained for a pulse sequence of bgrg, respectively. The dashed line corresponds to the theoretical increase as given by equation 4.1. Both the green photon numbers and the red photon numbers after blue excitation follow the theoretical curve. The gain in the blue channel after blue excitation is higher than expected. This deviation may be attributed to enhanced acceptor bleaching due to the increase in blue laser power. However, no decrease in the other two channels is observed. A normalization error is excluded, as the curve for BB could also not be fit to the theoretical gain curve by inclusion of a free normalization parameter. The total number of photons per burst (gray curve) decreases to 80% for the maximum number of blue pulses considered, which is attributed to the fact that both the decrease in intensity and the decrease in excitation frequency lower the red signal after red excitation (see section 4.1.1).

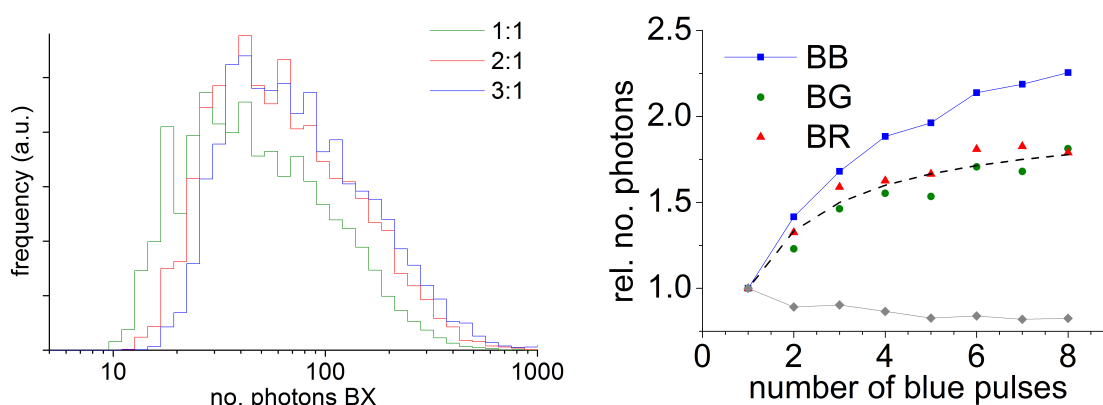


Figure 4.5: Effect of duty-cycle optimization on burstwise photon counts. (Left) Distribution of burstwise number of photons after blue excitation for different duty-cycle optimized pulse sequences. (Right) Mean number of photons per burst in the respective PIE channels. Dashed line: Theoretical gain. Gray squares: Total mean number of photons per burst.

4.1.3 Realization of optimized pulse sequences

Separation by macrotime

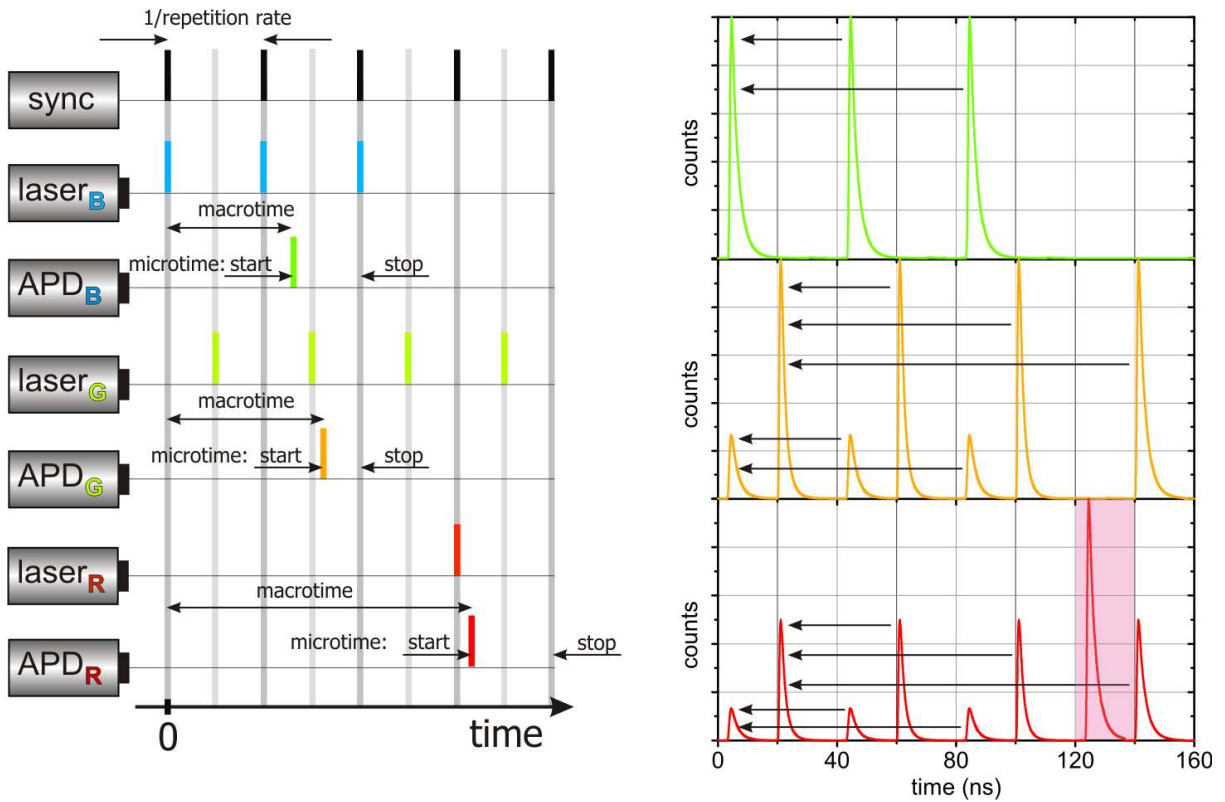


Figure 4.6: Experimental realization of duty-cycle optimized pulse sequences. (Left) Synchronization and excitation sequence for a pulse sequence of $[(bg)_3rg]_n$. Microtimes and macrotimes are obtained as described in section 3.6 on page 33. Adapted from Hendrix and Lamb, 2013. (Right) Respective microtime histogram for the blue (top), green (middle) and red (bottom) detectors. The red photons after red excitation are marked by the shaded region, which have to be distinguished from the red photons after blue excitation by the macrotime.

As described in section 3.1, the pulsed lasers are controlled by a SepiaII laser driver. The frequency for the base oscillator is provided by the sync output of the fixed frequency yellow laser at 27.4 MHz and the blue and red lasers are electronically delayed by cables of variable length. With the SepiaII every combination of blue and red laser pulses can be achieved. The sync output is set to pulse after every trigger (thus mirroring the frequency of the green laser) and is used to trigger the TCSPC cards. The experimental realization of duty-cycle optimized pulse sequences is shown in figure 4.6 for the case of three blue and one red laser pulse. Per complete pulse sequence $[(bg)_3rg]_n$ a total of 4 sync pulses occur. Thus all microtimes from each of the different subsequences are essentially projected into one microtime range. As can be seen from figure 4.6, right, this overlay of the microtimes is not a problem for the blue and green channels, due to the fact that no photons are detected in either channel after red excitation. However for the red channel red photons after blue excitation (BR) and red photons after red excitation (RR) will be overlaid. To distinguish the subsequences of types (bg) and (rg) for

the red channel the macrotime information can be used. For the showcased example with a total of four green pulses, the four different microtime ranges can be identified by the macrotime, of which the fourth is found to be the microtime range associated with the (rg) pulse sequence. Note that for this method to work, it is essential that the TCSPC cards do not miss sync pulses.

To distinguish the different subsequences, the modulo of the macrotimes M of the photons, divided by the number of green pulses per pulse sequence N , is computed. For the first three subsequences (bg), $M \bmod N = 1, 2, \text{ or } 3$. For the last subsequence (rg), however, $M \bmod N = 0$. Photons are then resorted based on the subsequence they originate from. As a last correction, the photons in the channel GR of the subsequence (rg) have to be added back to the channel GR of the other subsequences (bg).

Increasing the TAC range

Apart from the aforementioned method to achieve optimized pulse sequences, a complementary method shall also be discussed. A merit of the macrotime based discrimination of the different pulses is that if sync pulses are missed by the TCSPC card too frequently during the measurement, data analysis, while still possible, is complicated. The time points at which the sync pulse is missed have to be identified for both red TCSPC cards, and the new sync position has to be determined for every time interval. While in general the rate of missed sync pulses was low during the time of this work (ca. once every 24 h of measurement time), there were more erroneous periods during which a sync pulse was missed every 30 min on average. It is not clear what caused these fluctuations.

Thus, an alternative is proposed, that does not split up the pulse sequence, but rather increases the microtime range to contain the whole pulse sequence. This however has the disadvantage that at higher microtime ranges photon loss due to instrumental limitations is increased.

Photon loss due to the time to amplitude converter

The time to amplitude converter (TAC) limits the measured signal because only one photon can be detected per TAC range. Neglecting dead time after photon detection, which is independent of the used TAC range, the TAC induced photon loss can be described as follows: Consider that a photon is detected at time t_1 after the start of the TAC. Then all photons detected from this point in time until the end of the total TAC range T can not be detected. Assuming no background and Poissonian statistics for fluorescence emission, the probability that a second photon arrives at the detector in the remaining time interval $T - t_1$, which is then not detected due to the characteristics of the TAC, is given by:

$$P_{\text{miss}}(t_1; T) = \int_0^{T-t_1} \mu e^{-\mu t} dt = 1 - e^{-\mu(T-t_1)} \quad (4.3)$$

Here μ is the mean signal count rate. Assuming homogeneous distribution of the first photon over the time range T we calculate the total probability to miss a photon:

$$P_{\text{miss}}^{\text{total}}(T) = \frac{1}{T} \int_0^T (1 - e^{-\mu(T-t_1)}) dt_1 = 1 - \frac{1}{\mu T} (1 - e^{-\mu T}) \quad (4.4)$$

The detection probability, neglecting other effects, is then given by:

$$P_{\text{det}}(T) = 1 - P_{\text{miss}}^{\text{total}}(T) = \frac{1}{\mu T} (1 - e^{-\mu T}) \quad (4.5)$$

This reduction in detection probability decreases the gain achieved by duty-cycle optimization for a large number of pulses. The gain of a pulse sequence with N blue pulses is then given by:

$$G(N) = \frac{2N}{N+1} P_{\text{det}}(T_N) \quad (4.6)$$

where T_N is the TAC range associated with a pulse sequence given by N ($T_N = (N+1)k_{\text{sync}}^{-1}$, where k_{sync} is the sync rate). Figure 4.7 shows this relation.

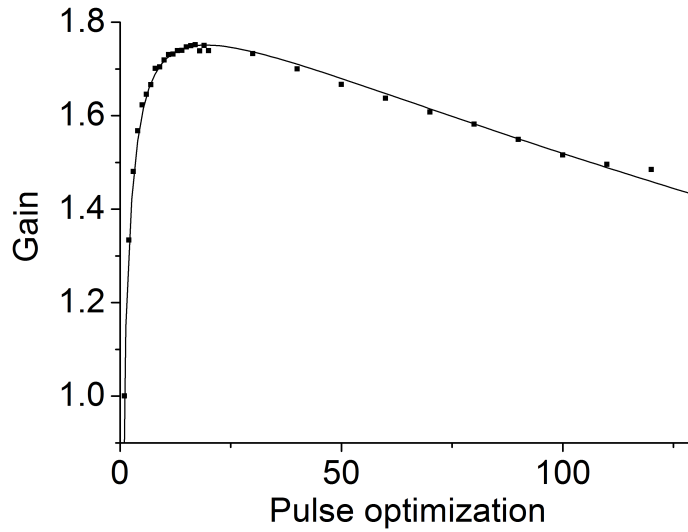


Figure 4.7: Gain of duty-cycle optimization when increasing the TAC range. The solid line is a fit to the data according to equation 4.6.

4.2 Two case studies: DNA measurements

In the following section, two different labeling schemes on triple-labeled DNA molecules are discussed. The double stranded DNA molecule used should not exhibit any dynamics, and the sequence was selected so that the occurrence of secondary structure elements (e.g. hairpin formation) is unlikely. The labeling positions are separated by 12 and 10 bp, respectively, and the middle position is located on the complementary strand (see section 3.5). Based on a rotation of B-DNA of 35.9° per bp, a rise of 3.32 \AA per bp and a diameter of 2 nm, the distances between the first and the second labeling position is estimated to be 4.3 nm, while the distance between the second and third labeling position is expected to be 3.9 nm. The separation between the first and third labeling position is on the order of 7.5 nm. Additionally, the dye linker lengths have to be considered. Thus, measured distances are expected to be slightly larger than the distances between the labeling positions.

Correction factors were determined from the single labeled subspecies as described in section 3.8.2. Only γ_{GR} could be determined from the measurements, as only for E_{GR} there were two species available with a large enough separation of the FRET efficiencies. As the determined value for $\gamma_{GR} = 0.78$ coincides reasonably well with the theoretically calculated value of 0.73, the theoretical values are used for $\gamma_{BG} = 0.74$ and $\gamma_{BR} = 0.54$. Note that in principle the γ -factor can be determined from double-labeled species using the lifetime information, even if only one FRET efficiency is available (see section 3.8.2). However, the γ -factor could not be accurately determined this way, and thus additional FRET species are needed. Due to the uncertainty regarding the correction factors, FRET efficiencies are not converted to actual distances here, although they can be related. Experimentally, a duty-cycle optimized excitation pulse sequence of ratio 3:1 between blue and red excitation has been applied. The laser powers have been adjusted such that all stoichiometries should show values close to 50% (blue laser: $115 \mu\text{W}$, green laser: $80 \mu\text{W}$, red laser: $100 \mu\text{W}$).

4.2.1 Stepwise three-color FRET

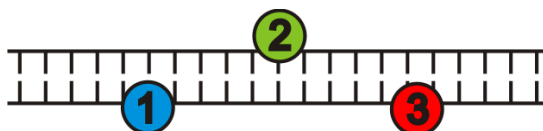


Figure 4.8: Scheme of the cascade dye arrangement on the DNA.

For the first DNA molecule to be discussed, the three dyes are positioned in a cascade arrangement (figure 4.8). The large distance between the blue and red dye, coupled with the already smaller Förster radius, will result in little to no FRET between them. Rather, upon excitation of the blue dye, FRET will occur in a stepwise manner from blue to green and subsequently from green to red. The corrected stoichiometry plot of S_{BG} vs. S_{BR} , as seen in figure 4.9 A, shows a reasonable amount of triple-labeled species ($S_{GR} \approx 0.35$, $S_{BG} \approx 0.4$).

A total of 6 different species are observed. The single labeled subpopulation of the blue dye is found for $S_{BG} > 0.9$ and undefined S_{GR} , while green-only labeled molecules are located at $S_{BG} \approx 0$ and $S_{GR} > 0.9$. A few red-only labeled molecules were measured, which are not visible in the plot ($S_{GR} \approx 0$, S_{BG} undefined), but were sufficient in number to determine the correction factors. The subpopulation BR is seen at $S_{BG} > 0.9$ and $S_{GR} < 0.1$, BG-labeled molecules are found at $S_{GR} > 0.9$ and undefined $S_{BG} \approx 0.4$, while GR-labeled molecules show $S_{GR} \approx 0.35$ and $S_{BG} < 0$. The negative values for S_{BG} of the GR-only species arise due the excessive corrections to the photon counts in the (empty) channels after blue excitation in this case. More precisely, the artifact is caused by the last correction in equation 3.10, in combination with the high efficiency E_{GR} observed for the double-labeled species (see section 3.8.2).

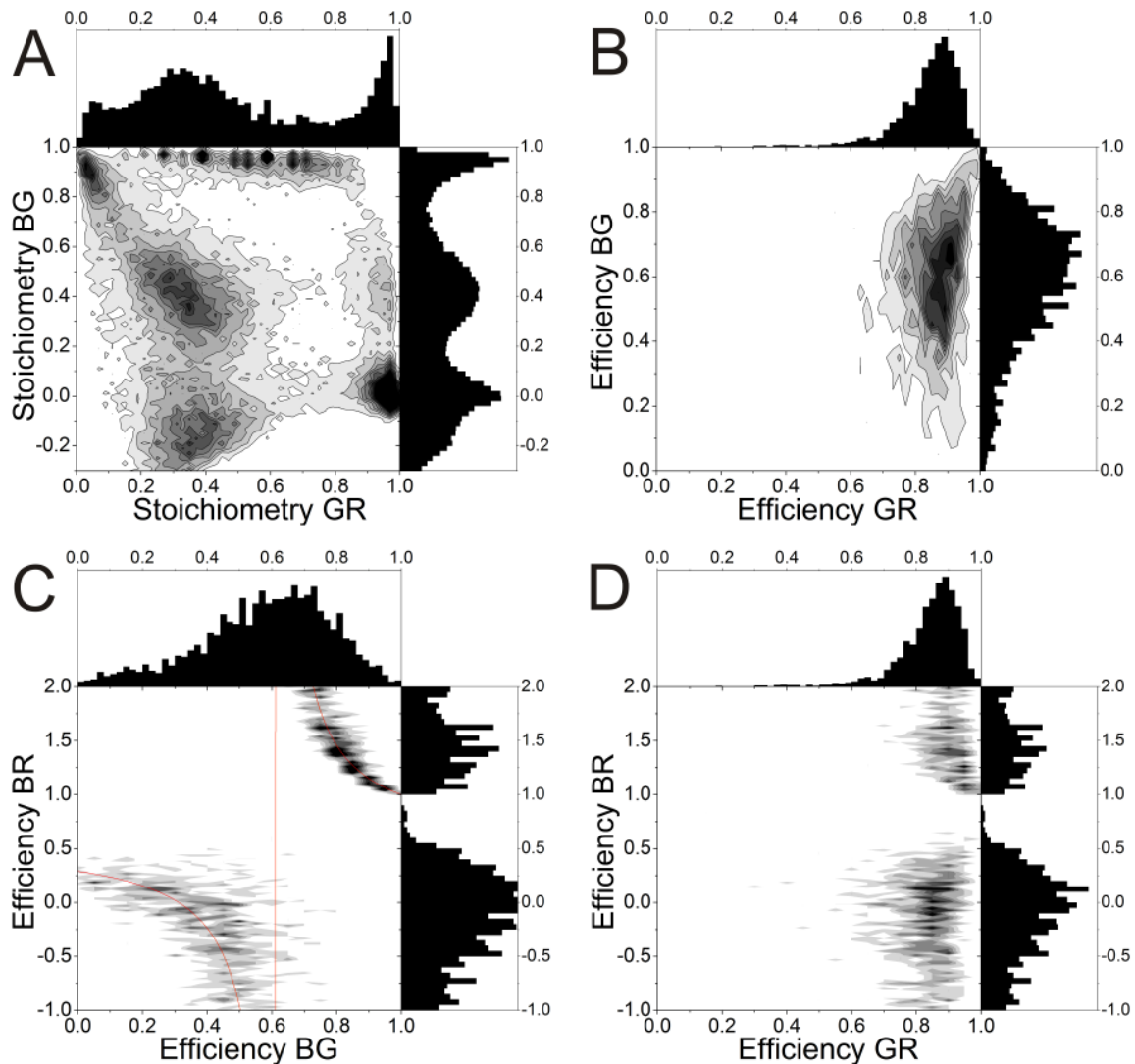


Figure 4.9: Two-dimensional stoichiometry (A) and efficiency (B-D) distributions for the cascade dye arrangement. The red line in C is given by equation 4.7.

The triple-labeled species was selected using the 2CDE-filter ($ALEX_{2CDE} < 10$ for all channels). One dimensional efficiency plots for the triple-labeled species are shown in figure 4.10.

E_{GR} is found to be 0.88 (mode of the distribution). For the efficiencies E_{BG} and E_{BR} calculated from the triple-labeled species (C, E), additionally the proximity ratios are included in the plot to show the effect of the corrections as discussed in section 2.4. Due to high efficiency of E_{GR} , only few counts in the green channel are detected after blue excitation, resulting in a low proximity ratio ϵ_{BG} . After correcting for the FRET from the green to the red dye, the distribution shifts to higher values and E_{BG} is obtained to be approximately 0.7. To ensure the validity of the calculated FRET efficiency distribution, it is compared to E_{BG} obtained from the sub-labeled species BG (4.10, D). A slight deviation of the distribution of $E_{BG}^{BG\text{-only}}$ towards lower values is observed, but both distributions agree reasonably well.

The situation is more complicated for E_{BR} (figure 4.10, E). The proximity ratio indicates a value of 0.25, which in this case, however, almost entirely originates from FRET from the green dye as the distance between the red and the blue dye is very large. The efficiency E_{BR} , as determined from the sub-labeled species BR (see figure 4.10, F) exhibits a value of 0, however also a small high FRET fraction is observed. The corrected FRET efficiency E_{BR} exhibits a seemingly strange distribution. The expected result of $E_{BR} \approx 0$ is evident as the broad distribution is centered around a value of zero. Additionally, however, a significant amount of bursts shows apparent FRET efficiencies greater than one.

The unexpected distribution of E_{BR} can be understood by recalling that the photon counts in the red channel after blue excitation are prone to a large number of corrections. E_{BR} is calculated by:

$$E_{BR} = \frac{F_{BR} - E_{GR}(F_{BG} + F_{BR})}{F_{BB} + F_{BR} - E_{GR}(F_{BB} + F_{BG} + F_{BR})}$$

In theory, the numerator should be zero for the case discussed here. In practice, however, this is seldom the case, because shot-noise effects both F_{BR} and E_{GR} , as well as all performed corrections, which themselves are based on photon counts. The equation can be rewritten as follows:

$$E_{BR} = \frac{F_{BR}(1 - E_{GR}) - E_{GR}F_{BG}}{F_{BR}(1 - E_{GR}) + F_{BB}(1 - E_{GR}) - E_{GR}F_{BG}}$$

Three cases have to be considered:

1. $F_{BR}(1 - E_{GR}) > E_{GR}F_{BG}$: The numerator is positive. Then, also the denominator is greater zero and E_{BR} will be between 0 and 1. With increasing E_{GR} the difference will decrease.
2. $F_{BR}(1 - E_{GR}) < E_{GR}F_{BG}$ but still $F_{BR}(1 - E_{GR}) + F_{BB}(1 - E_{GR}) > E_{GR}F_{BG}$: The numerator is negative, while the denominator is greater than zero. The obtained value will be negative. For larger values of E_{GR} , the absolute value of the numerator will increase while the denominator will be close to zero. Thus the width of the determined distribution for E_{BR} will be large and may reach large negative values.

3. $F_{BR}(1 - E_{GR}) + F_{BB}(1 - E_{GR}) < E_{GR}F_{BG}$: Now also the denominator is smaller than zero. The value for E_{BR} is now positive again. If the denominator is small, large values are obtained. With increasing values for the denominator or increasing E_{GR} , the value for E_{BR} will shift towards 1, but will never be less.

With these considerations in mind, the distribution of E_{BR} and the correlation between E_{BR} and E_{GR} (see figure 4.9, D) are explained. Additionally, the correlation observed between E_{BR} and

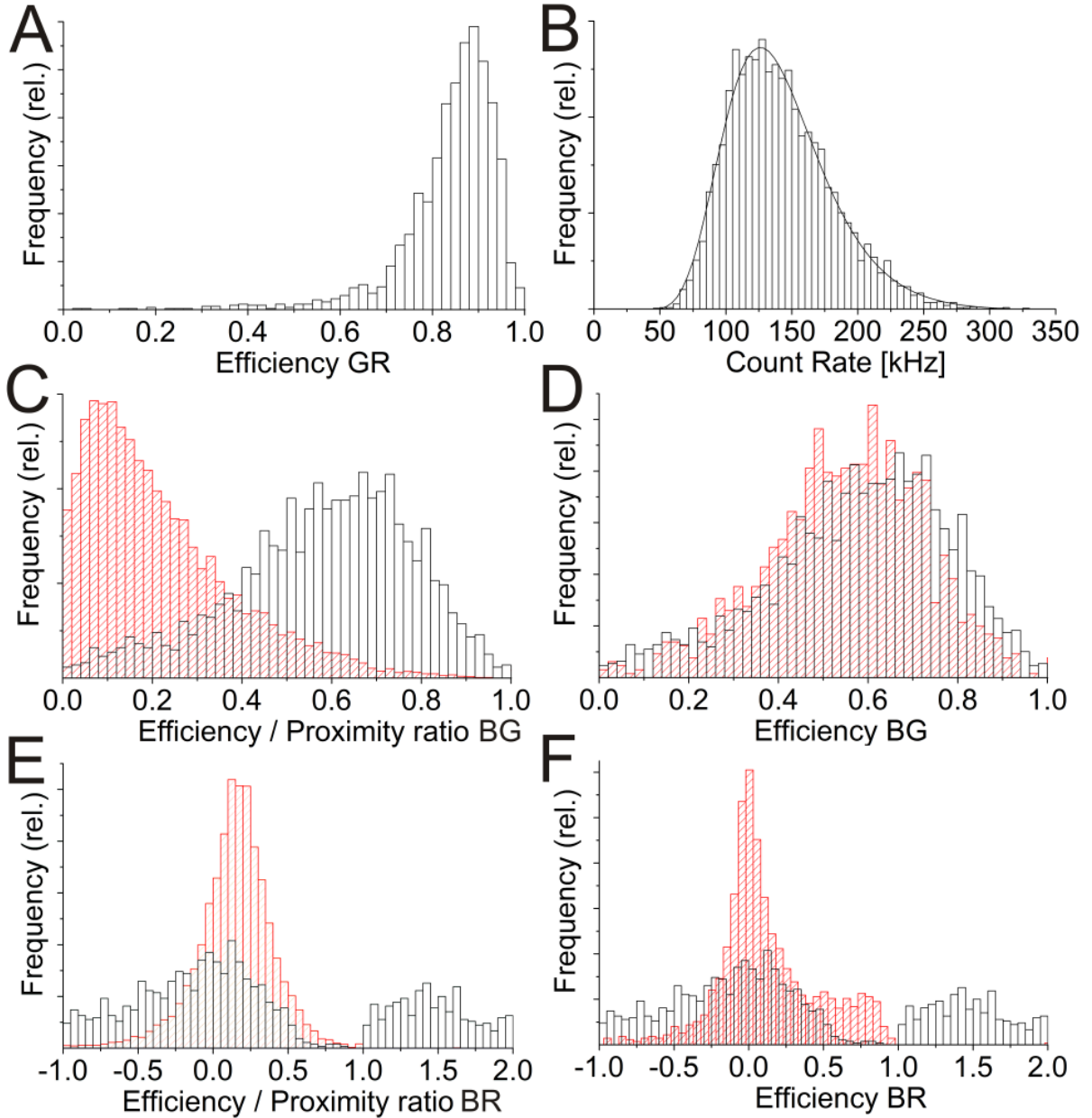


Figure 4.10: One-dimensional parameter distributions for the cascade dye arrangement. A: Distribution of E_{GR} as determined from the direct excitation of the green dye. B: Burstwise count rate. The solid line is a log-normal fit with a center value 136.5 ± 0.5 kHz. C, E: Comparison of efficiencies (black) and corresponding proximity ratios (red). D, F: Comparison of efficiencies from the triple-labeled species (black) and from double-labeled species (red).

E_{BG} is elucidated by deriving the dependence between the two quantities:

$$E_{BR} = \left(\left(\frac{BR}{BB} - E_{GR} \frac{E_{BG}}{1 - E_{BG}} \right)^{-1} + 1 \right)^{-1} \quad (4.7)$$

A good fit to the experimental two-dimensional histogram is found for $\frac{BR}{BB} = 0.6$ and $E_{GR} = 0.88$, as determined from the experimental data (see figure 4.9, C).

The cascade arrangement is best used to monitor long-distance interactions via two-step FRET. In this case, the best parameter to observe distance changes is simply the proximity ratio BR. A general rule is to be careful when looking at parameters which rely on heavy corrections and are expected to be small as artifacts can severely distort the obtained distributions.

Comparison of the obtained values with theoretical efficiencies obtained from the distance estimates and Förster radii yields good agreement for E_{GR} (measured: 0.88, theoretical: 0.96). The theoretical value for E_{BR} is estimated to be 0.09 and thus higher than the measured value of ~ 0 . The deviation may be due to the linker length, which is not incorporated in the distance estimate, or it may arise due to inaccurate correction factors, which weigh heavily for the channel BR if applied to small photon numbers. The efficiency E_{BG} at approximately 0.7 is also lower than the theoretical value of 0.9. The theoretical calculations, however, are based on a simplified model and do not take the exact positions of the dyes with respect to minor and major groove of the double-stranded DNA construct into account.

4.2.2 Full three-color FRET

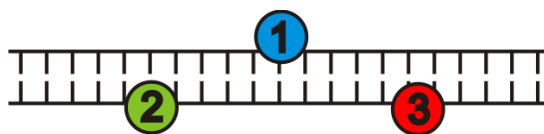


Figure 4.11: Scheme of the full three-color FRET DNA.

For the second DNA molecule, all three dyes are positioned within FRET range to each other, with the blue dye situated in the middle. The FRET efficiency E_{BG} is expected to be unchanged with regards to the previously discussed construct, while E_{GR} is expected to be lower and FRET between the blue and the red dye should be observed. The corrected stoichiometry plot of S_{BG} versus S_{GR} is shown in figure 4.12 together with two-dimensional FRET efficiency histograms. A reasonable amount of triple-labeled molecules was observed. The sample shows a large amount of GR-only labeled molecules, while also a reasonable amount of BR-only and BG-only molecules were detected. Significant amounts of single labeled species are found for the green and red dye, while again the small population of red-only labeled molecules is not resolved by the scale of the graph.

The one dimensional efficiency distributions for the triple-labeled species are shown in figure 4.13, A, C and E. The efficiency E_{GR} indicates two populations: The low FRET population is situated at 0.3, while the high FRET state is found at 0.8. Interestingly, the high FRET state is found to be similar to the FRET efficiency observed for the cascade dye arrangement. E_{BG} is unchanged with regard to the cascade construct at 0.7. The difference between the proximity ratio and efficiency distributions is found to be smaller due to the smaller FRET efficiency GR. A similar distribution as discussed before is observed for E_{BR} , whereat the peak is now found at 0.25. Coincidentally, the proximity ratio distribution is found to be at the same position. Comparison between the efficiency determined from the double-labeled species with those determined from the triple-labeled construct (4.13, D and F) again confirms the validity of the three-color FRET calculations. Very good agreement is found for E_{BG} , while for E_{BR} peak positions coincide, but the underlying distribution differs due to the reasons discussed in the previous section. In the two-dimensional efficiency-efficiency plots (4.12, B-D), correlation is again observed for E_{BR} with regard to the other two efficiencies. For E_{BG} versus E_{GR} , high efficiency E_{GR} correlates with high efficiency E_{BG} .

A closer inspection of the abundant species GR reveals a FRET efficiency E_{GR} of nearly 1 (4.13, A). A 2D-plot of E_{GR} versus S_{BG} for the isolated species BGR and GR (figure 4.12, E) reveals that only few of the GR-only molecules are found in a FRET state similar to the triple-labeled species. Apparently, single stranded DNA molecules of the GR labeled strand assume a condensed structure e.g. due to hairpin formation, bringing the two dyes into close contact.

The theoretical FRET efficiency E_{BR} at 0.84 is much larger than the measured value of 0.25.

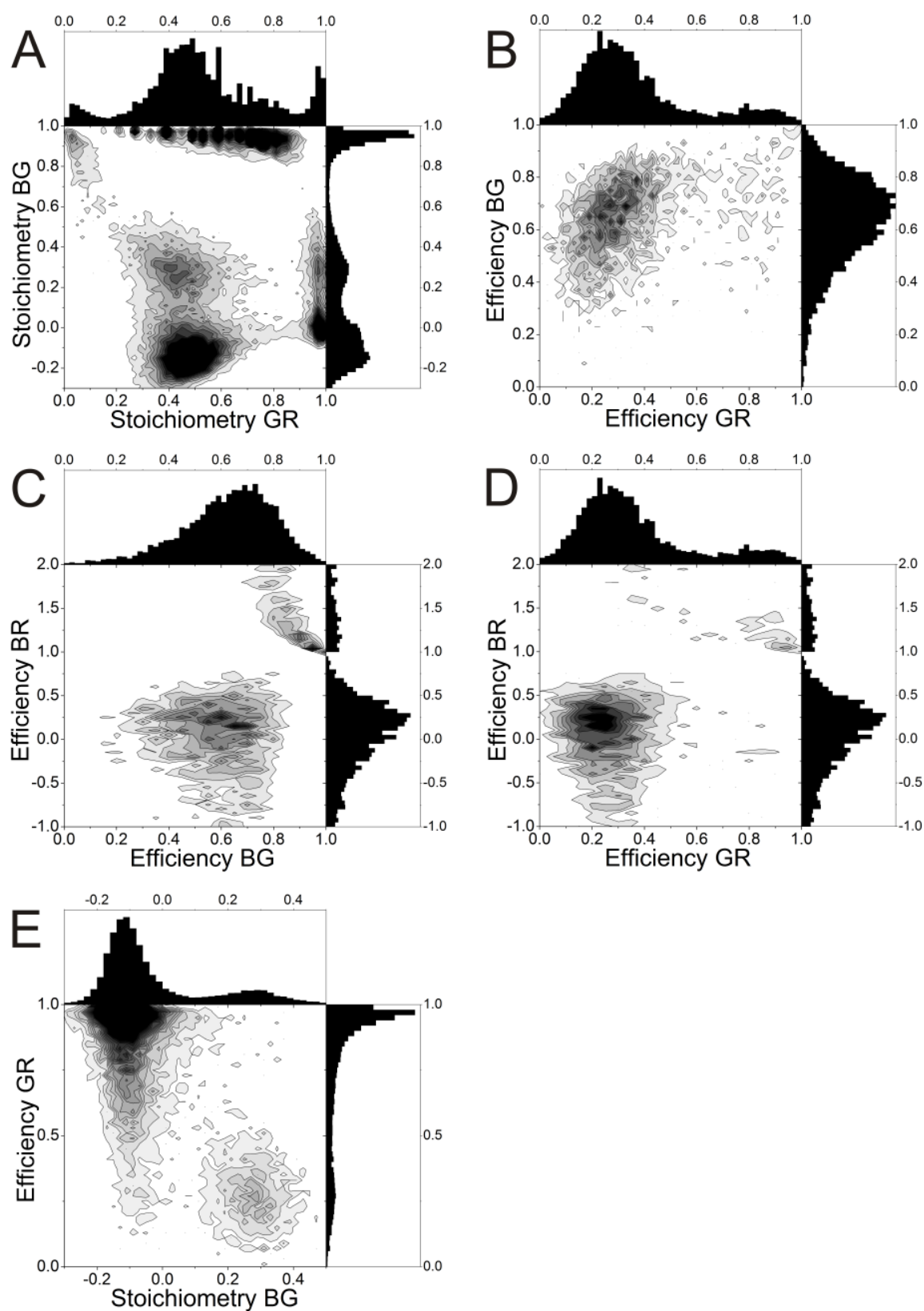


Figure 4.12: Two-dimensional stoichiometry (A) and efficiency (B-D) distributions for the full three-color FRET dye arrangement. E: Two-dimensional histogram of E_{GR} versus S_{BG} for the species BGR and GR. Selection was performed by setting $ALEX_{2CDE}^{GR} < 7$.

However, also for the cascade construct, the theoretical value for the same dye positions was overestimated with respect to the efficiency determined by means of the green and red dye. The lower Förster radius of 5.1 nm for the dye pair blue-red makes it more sensitive in the region of the observed distance of ~ 5 nm. Deviations are thus expected. The efficiency E_{GR} at 0.3 agrees well with the theoretical value of 0.36, is however again slightly underestimated.

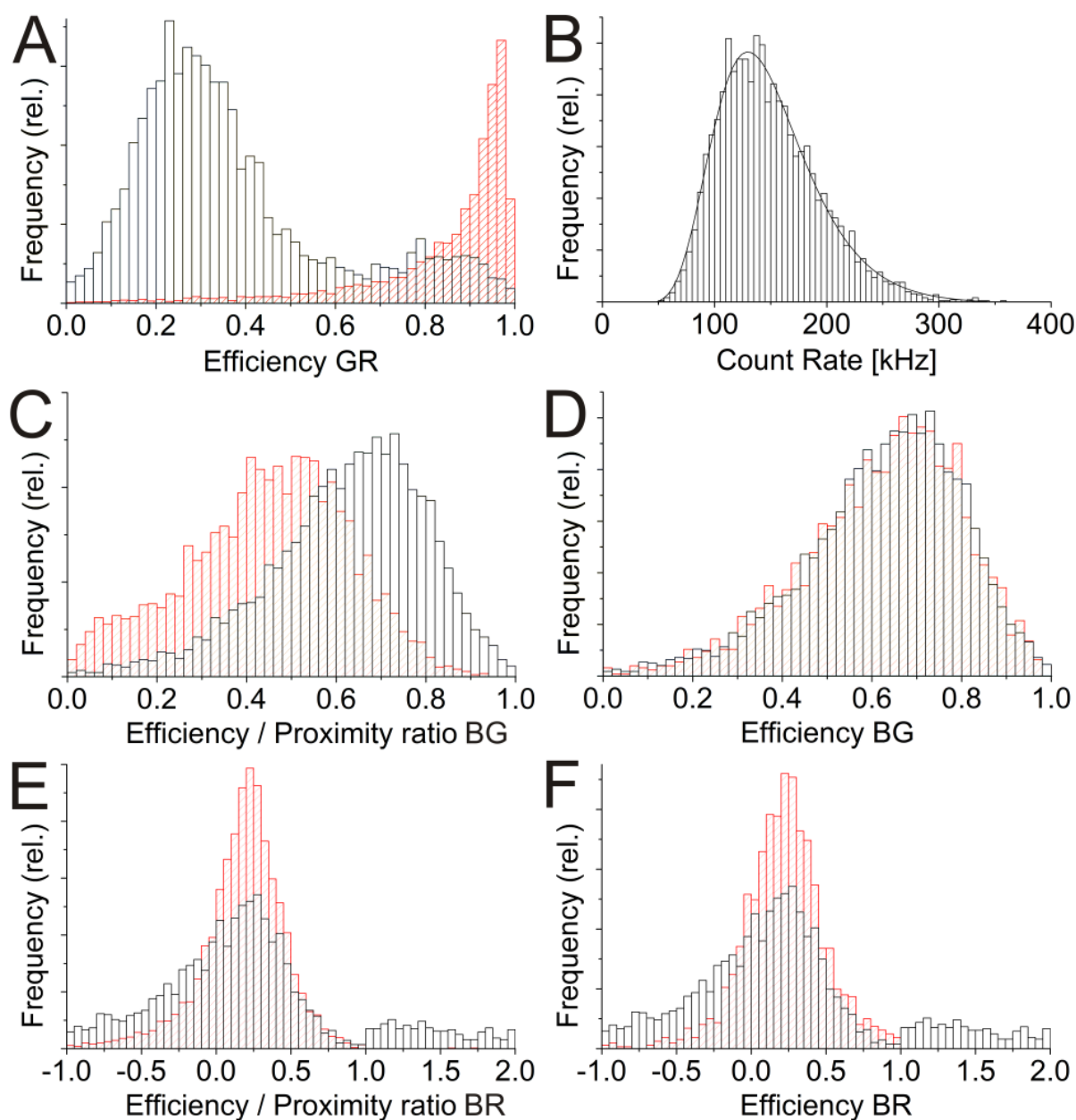


Figure 4.13: One-dimensional parameter distributions for the full three-color FRET dye arrangement. A: E_{GR} as determined from the triple-labeled species (black) and from the double-labeled species (red). The distributions are not area normalized in this case. B: Burstwise count rate. The solid line is a log-normal fit with center value 142.7 ± 0.7 kHz. C, E: Comparison of efficiencies (black) and corresponding proximity ratios (red). D, F: Comparison of efficiencies from the triple-labeled species (black) and from double-labeled species (red).

4.3 Three-color FRET study of the Hsp70 chaperone BiP

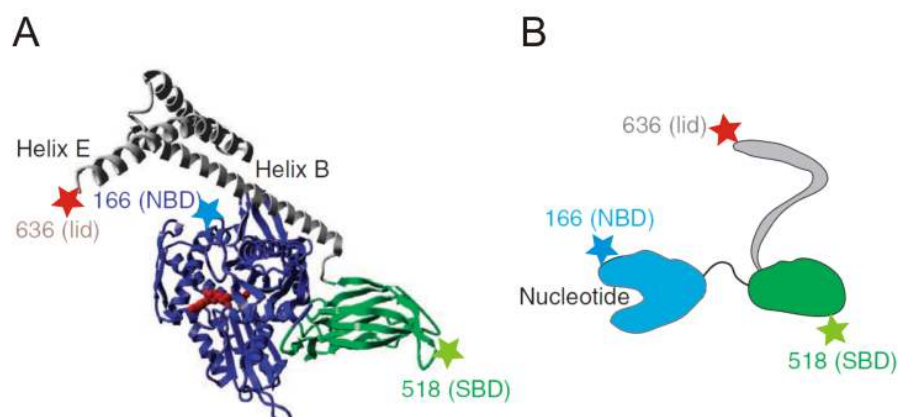


Figure 4.14: Labeling positions within BiP for three-color FRET measurements. The dyes are colored by their emission. Green: Atto488, orange: Atto565, red: Atto647N. A: Labeling positions as highlighted in the crystal structure of the Hsp70 homolog Sse1. B: Scheme of BiP with dye positions. Blue: nucleotide binding domain, green: substrate binding domain with lid (gray). Adapted from Marcinowski et al. (2011).

BiP (Binding Immunoglobulin Protein) is a Hsp70 chaperone found in the endoplasmic reticulum. It is involved in folding, assembly and quality control of proteins of the secretory pathway. The functional cycle of BiP is mediated by ATP to regulate the binding and release of substrates. BiP is constituted of two domains. The N-terminal nucleotide binding domain (NBD) is connected to the substrate binding domain (SBD) by a flexible, hydrophobic linker. The SBD itself consists of a compact β -sandwich domain with a substrate binding site and an extended α -helical domain at the C-terminus (the 'lid'). Hydrolysis of ATP in the NBD provokes structural changes in the SBD that are transmitted via the linker.

Marcinowski et al. (2011) performed spFRET measurements on BiP, exploring a total of four labeling positions: One on the NBD and SBD and two different positions on the lid (see figure 4.14; on the lid only the labeling position discussed here is shown). The conformations of BiP were probed in the presence and absence of nucleotides and with two types of substrates, i.e. a small model peptide and, as an authentic substrate, the C_H1 domain of antibodies. SpFRET data for the apo-, ADP- and ATP-state of BiP are shown in figures 4.15 to 4.17 (B, D, F). Broad FRET efficiency distributions are observed for the NBD-SBD and NBD-lid sensors in the apo-state, whereas the SBD-lid sensor indicates a well-defined closed state at high FRET efficiency. Similar heterogeneity is found in the ADP-bound state for the NBD-SBD and NBD-lid sensors. For the SBD-lid sensor, an additional low-FRET population occurs, indicating an open conformation. In the presence of the non-hydrolyzable ATP analog AMP-PNP (adenylyl imidodiphosphate), two distinct populations are observed for the NBD-SBD sensor and, to some extent, for the NBD-lid sensor. Tighter coupling between the domains is implied by the shift of the efficiency distribution to higher values compared to the ADP-bound state. The SBD-lid sensor is almost exclusively found in a low-FRET state, indicating a complete

opening of the lid upon binding of ATP.

In summary, BiP is found to be flexible with regards to all domains in the apo- and ADP-states, with slightly more defined distributions in the ADP-bound state. ATP-binding brings the two domains into closer contact, resulting in opening of the lid.

4.3.1 Specific labeling via unnatural amino acids¹

Labeling of proteins for spFRET measurements is usually performed by reaction of maleimide-dye conjugates with natural or artificially introduced cysteines. The outcome is a stochastic distribution of labeling stoichiometries, that is donor- and acceptor-only, as well as double-labeled molecules with the donor at labeling site A and the acceptor at labeling site B and vice versa. The interpretation of spFRET data is not effected by the two labeling possibilities (DA and AD), if the local environments of the two labeling sites are similar. Stochastic labeling for three-color MFD, however, yields a total of 6 permutations of dye positions. The complexity of the system is reduced, if at least one position can be specifically labeled. Due to different accessibility of the labeling sites and diverse characteristics of the dyes, e.g. charge or hydrophobicity, pseudo-specific labeling of the remaining two sites can be achieved by adjusting the experimental conditions.

Specific labeling of the protein with Atto488 is performed via introduction of the unnatural amino acid propargyllysine (PrK). The azide-conjugate of the dye is covalently linked to PrK by copper-catalyzed alkyne-azide cycloaddition click chemistry (Milles et al., 2012b; Tyagi and Lemke, 2013). Labeling positions of Atto565 and Atto647N are defined by replacement of the two naturally occurring cysteines by serines and introduction of two artificial cysteines at the desired positions. Labeling of the two artificially introduced cysteine residues was performed simultaneously at a three-fold excess of both maleimide-dye conjugates.

4.3.2 Comparison of efficiencies from three-color FRET with spFRET

FRET efficiencies, determined from the triple-labeled BiP, are shown in figures 4.15 to 4.17 (A, C, E). Measurements were performed with a pulse sequence of $[(bg)_3rg]_n$ at laser powers of 110 μ W for the blue laser, 80 μ W for the yellow laser and 100 μ W for the red laser over the course of 8 h. Burst selection was performed by TCBS with parameters $L = 100$, $T = 500 \mu$ s and $M = 10$ for every channel. No additional data filtering was performed. Because labeling efficiencies for the triple-labeled protein are low, only approximately 2000 bursts were collected for every measurement. The same γ -factors as for the DNA measurements were used.

The different Förster radii of 68 Å for Atto565-Atto647N, 51 Å for Atto488-Atto647N and 63 Å for Atto488-Atto565, with regards to the R_0 of 59 Å for Atto532-Atto647N as used in the publication, have to be considered. Thus, when comparing efficiency from spFRET data

¹The biological and biochemical work associated with this project was performed by Lena Voith von Voithenberg.

with three-color efficiencies, lower efficiencies are expected for E_{BR} , while higher values will result for E_{GR} and E_{BG} . Comparison of the FRET efficiency distributions for E_{BG} and E_{BR} with the spFRET data obtained for the NBD-lid and NBD-SBD sensors indicates good agreement between E_{BG} and the NBD-SBD sensor and E_{BR} and the NBD-lid sensor for all measurements. Based on the similarities of the FRET efficiency distributions, specific labeling is suggested for Atto647N at the lid and Atto565 at the SBD. For the case of stochastic labeling of the two dye positions, the efficiency distribution of E_{BG} and E_{BR} should show a weighted sum of the distributions for the NBD-SBD and NBD-lid sensors, which is not observed. Additionally, evidence for specific labeling can be found from the two-dimensional efficiency histograms

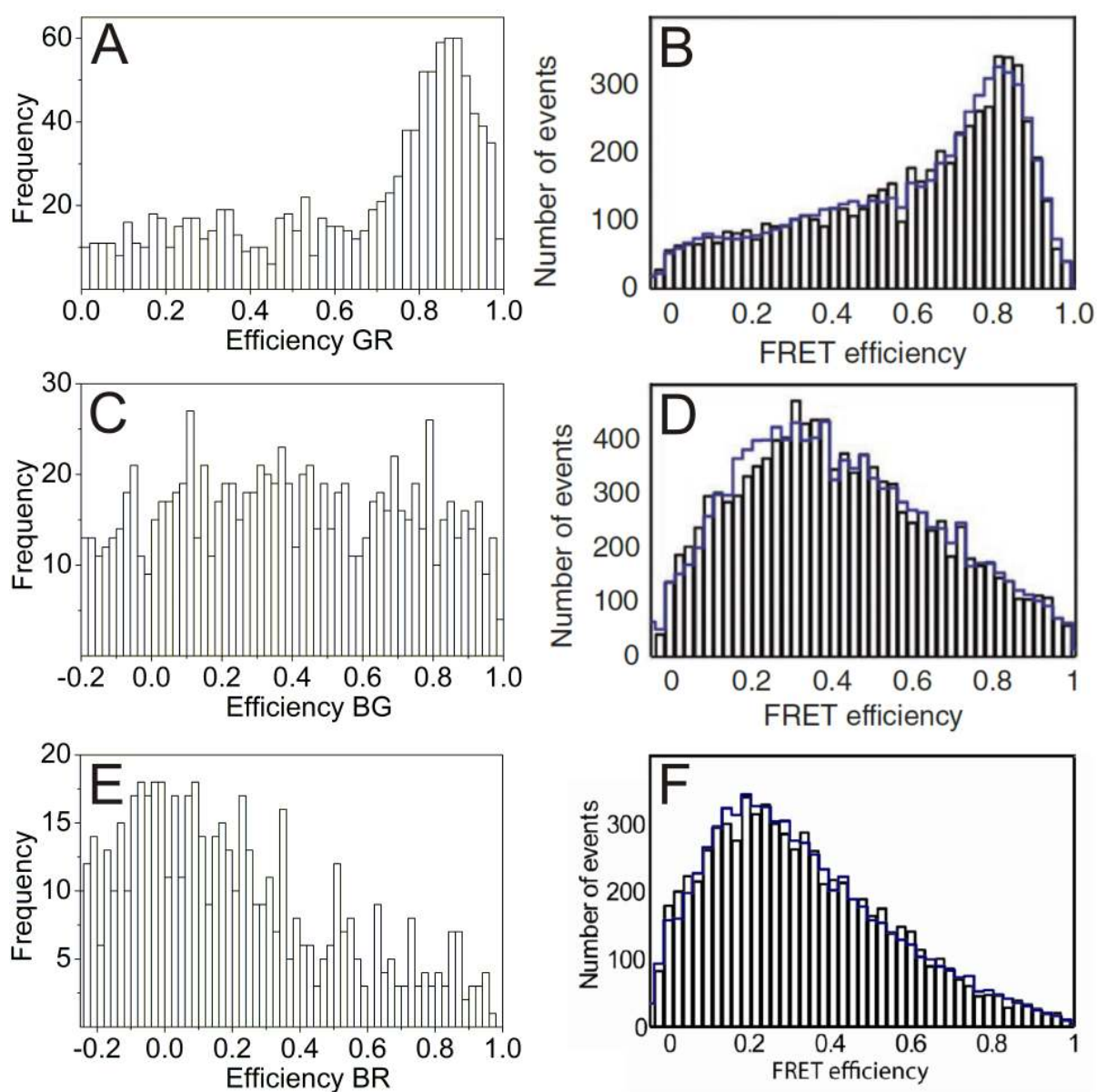


Figure 4.15: FRET analysis of BiP in the absence of nucleotides (apo). Comparison of FRET efficiencies determined from three-color MFD (A, C, E) with spFRET efficiencies from Marciniowski et al. (2011) (B, D, F). B: Lid-SBD sensor. D: NBD-SBD sensor. F: Lid-NBD sensor.

(see figures 4.18 to 4.20). For the case that both labeling possibilities are present, the plot of E_{BR} versus E_{BG} should show anticorrelated behavior if different distances are observed for the NBD-lid and the NBD-SBD sensor (e.g. for the ADP-bound state). Thus, two populations (high E_{BG} / low E_{BR} and low E_{BG} / high E_{BR}) should be observable. Figure 4.19, A, however, rather indicates correlation between the two FRET efficiencies. An argument for specific labeling can also be made based on the dye properties. Atto647N is a highly hydrophobic dye, thus differences in polarity or the presence of charged groups at the two labeling sites may highly bias the labeling.

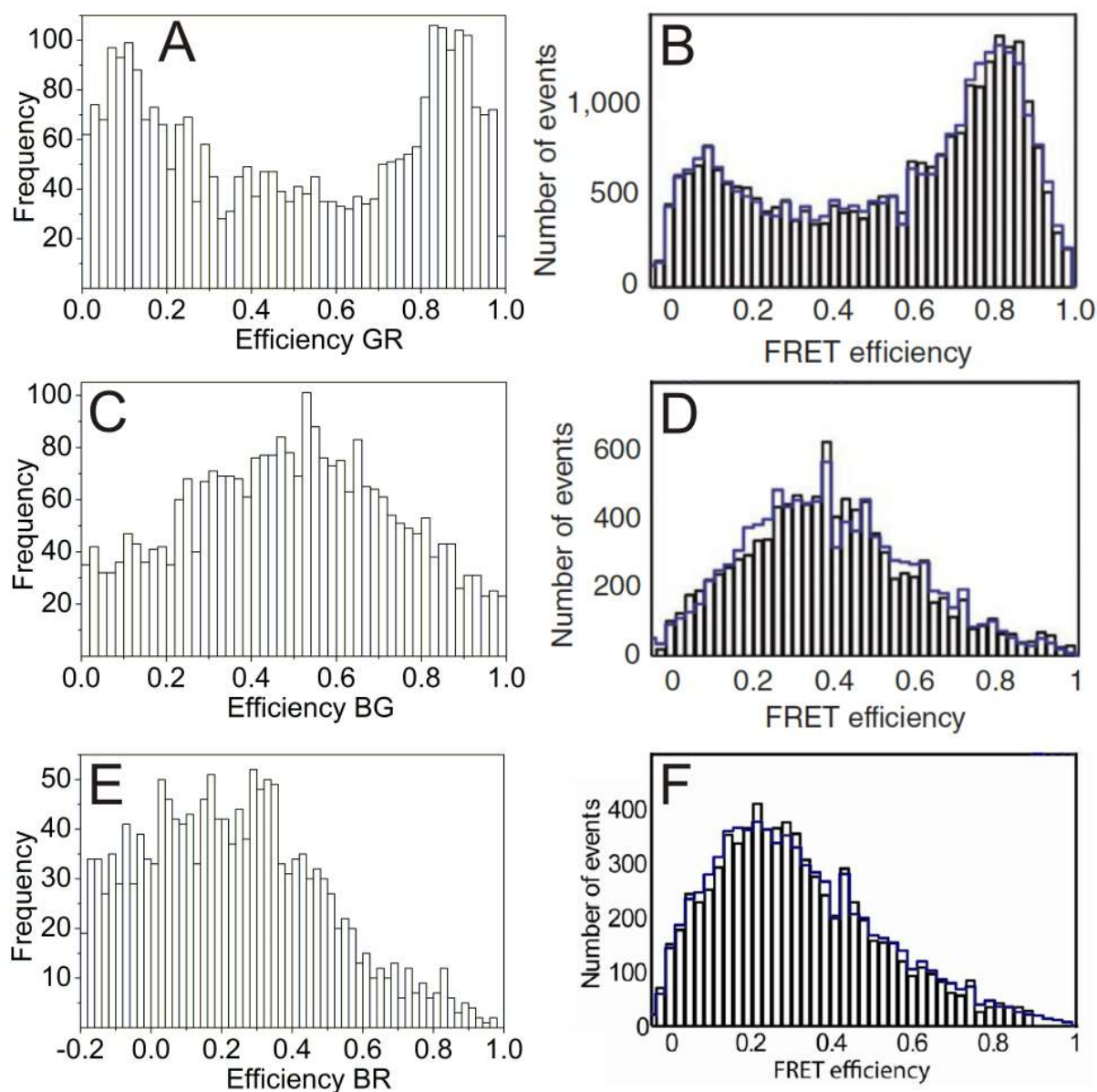


Figure 4.16: FRET analysis of BiP in the presence of ADP. Comparison of FRET efficiencies determined from three-color MFD (A, C, E) with spFRET efficiencies from Marcinowski et al. (2011) (B, D, F). B: Lid-SBD sensor. D: NBD-SBD sensor. F: Lid-NBD sensor.

All in all, the three-color FRET approach is validated by the reproduction of the spFRET results with regard to the shape of the obtained FRET efficiency distributions.

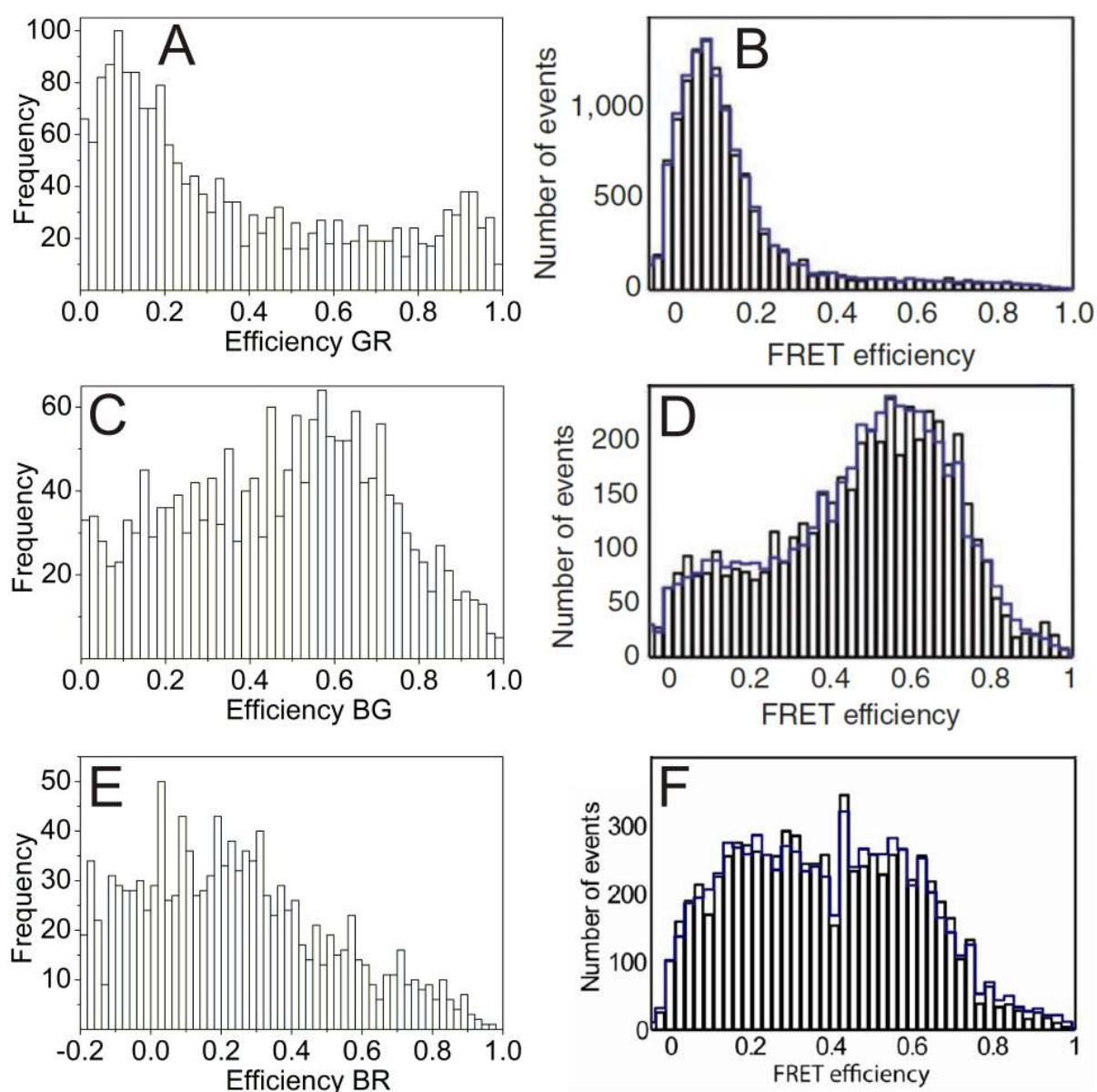


Figure 4.17: FRET analysis of BiP in the presence of the ATP analog AMP-PNP. Comparison of FRET efficiencies determined from three-color MFD (A, C, E) with spFRET efficiencies from Marcinowski et al. (2011) (B, D, F). B: Lid-SBD sensor. D: NBD-SBD sensor. F: Lid-NBD sensor.

4.3.3 Correlated motion in BiP

To investigate correlated motions of the different domains of BiP, two-dimensional efficiency plots are presented in figures 4.18 to 4.20. Again, data have to be interpreted carefully due to the artifacts discussed in the previous section: a) Nonsensical values of $E_{BR} > 1$ will occur for both high values of E_{GR} and E_{BG} . b) If E_{GR} is close to 1, also E_{BG} will converge to 1. These artificial correlations have to be distinguished from biological relevant correlations.

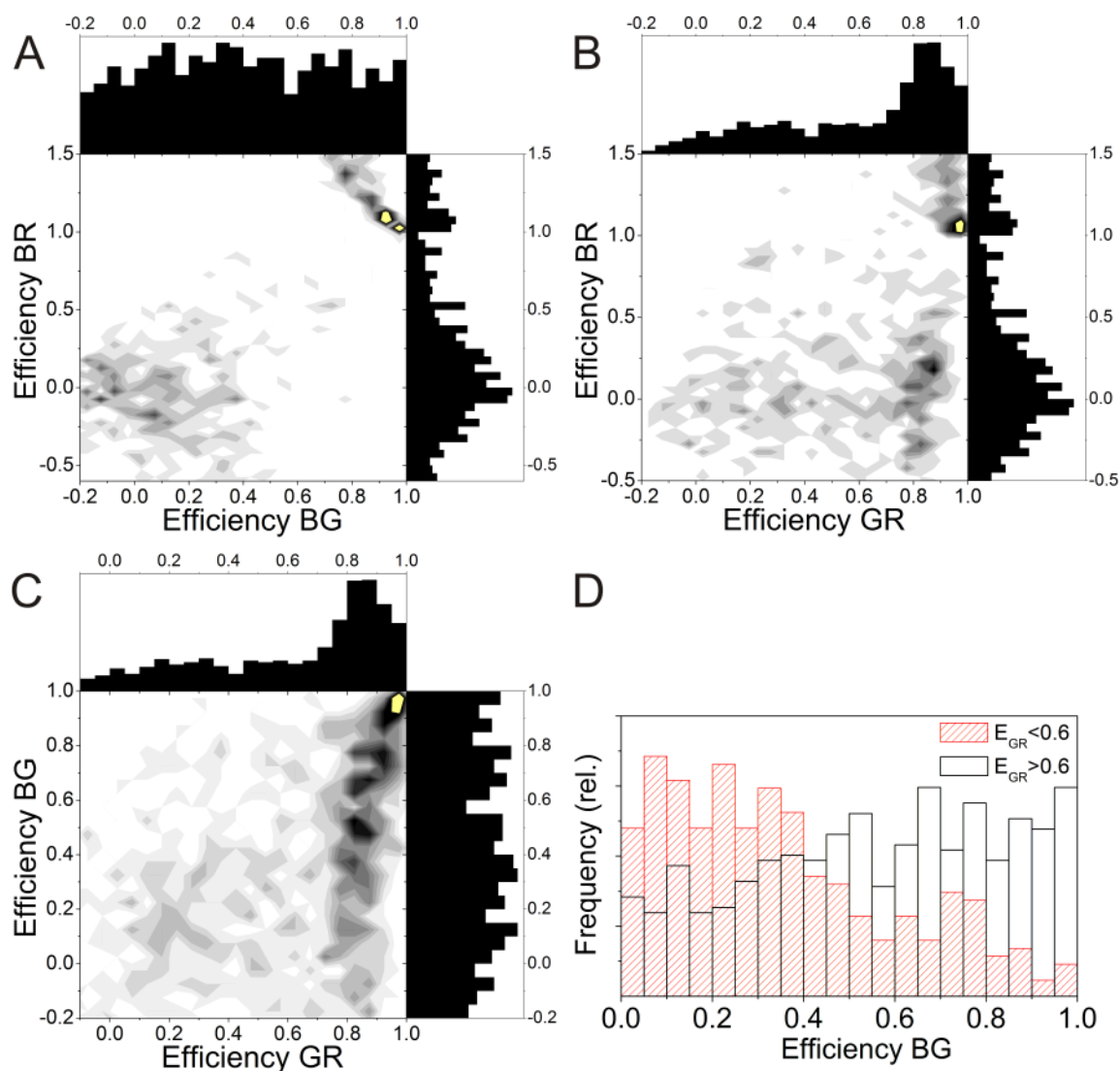


Figure 4.18: Two-dimensional efficiency plots for BiP in the apo-state (A-C). D: Efficiencies E_{BG} for the two populations observed in C, separated by E_{GR} .

For the apo-state, analysis of correlation for the efficiency E_{BR} proves difficult because it is close to 0 and suffers from the same complications as discussed for the two-step FRET DNA (see section 4.2.1). No correlation is observed for the interpretable part of the histogram for $E_{BG} < 0.5$. Similarly, for E_{GR} , no change in E_{BR} is observed for $E_{GR} < 0.6$. However, for $E_{GR} \approx 0.8$ the distribution of E_{BR} is shifted to slightly higher values centered at 0.2. Larger

changes are observed for E_{BG} with respect to E_{GR} . A clear shift of E_{BG} towards higher values is observed at larger E_{GR} . One dimensional histograms of E_{BG} are shown for E_{GR} smaller and larger than 0.6. E_{BG} changes from ~ 0.2 to values of 0.6-0.8. Again, the peak at $E_{GR} = E_{BG} = 1$ has to be considered an artifact. The correlated changes of the FRET efficiencies indicate correlated motion within the protein. The distance between lid and NBD is high for the apo-enzyme, resulting in a low sensitivity for the respective sensor E_{BR} . If the lid closes (high E_{GR}), also the lid and the NBD come in closer contact, indicated by the slight shift to higher E_{BR} . Moreover, the closed-lid state seems to go hand in hand with a smaller distance between the NBD and the SBD, as indicated by the increase in E_{BG} for high E_{GR} .

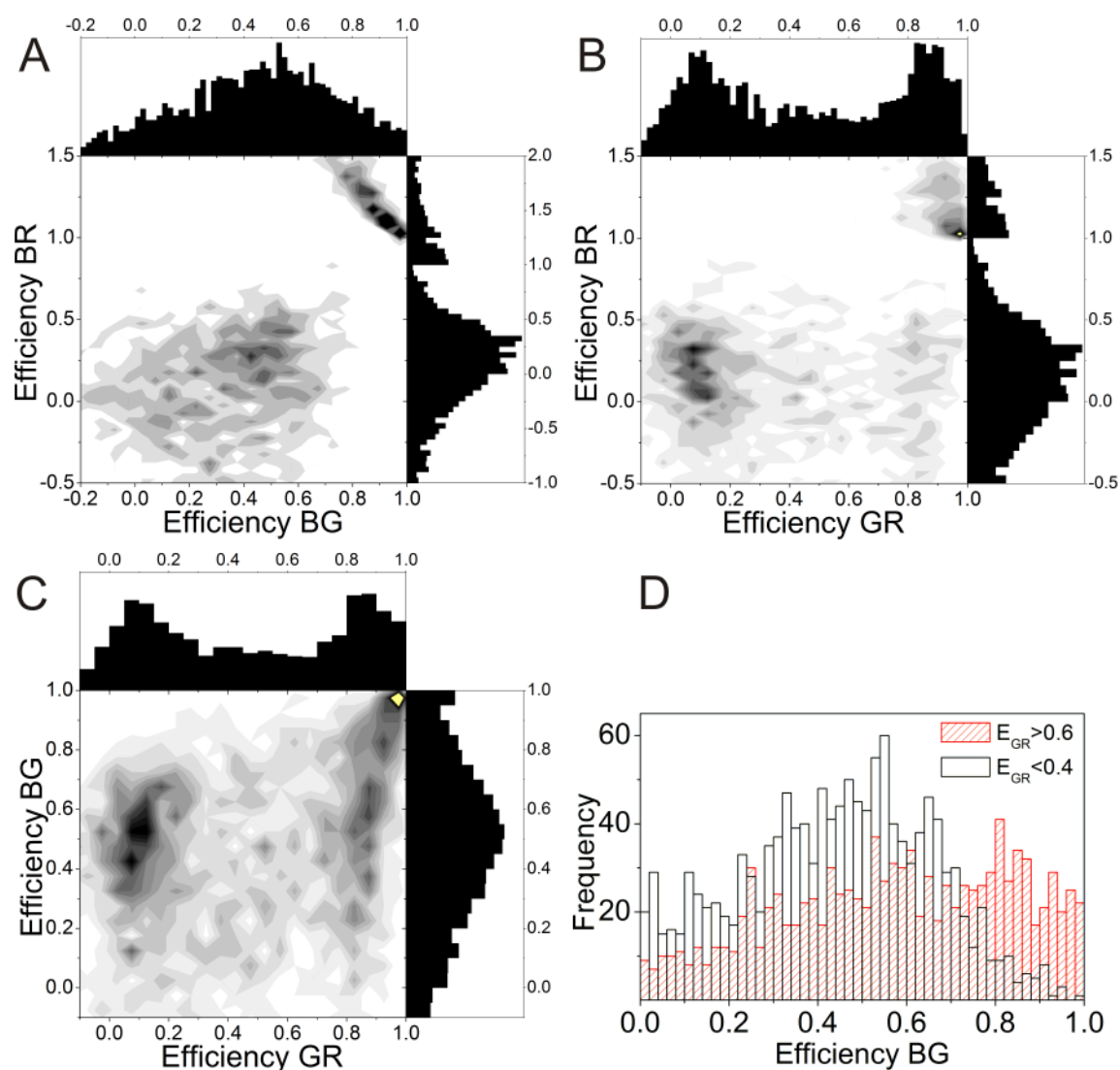


Figure 4.19: Two-dimensional efficiency plots for BiP in the presence of ADP (A-C). D: Efficiencies E_{BG} for the two populations observed in C, separated by E_{GR} .

Similar results are obtained for the ADP-bound state (figure 4.19). Correlation is observed between E_{BR} and E_{BG} . E_{BR} is centered around zero for low E_{BG} , but increases to ~ 0.3 for $E_{BG} > 0.4$. Interestingly, E_{BR} is independent of E_{GR} . For both states (E_{GR} at 0.2 and 0.9,

see figure 4.19, B), similar distributions for E_{BR} are observed. On the other hand, for E_{BG} a second peak at high FRET (>0.75) is found and overall a slight shift towards higher FRET efficiencies is evident, that remains relevant even if the artificial correlation at high values of E_{GR} is considered (see also the one dimensional histograms in 4.19, D). The smaller distance between the lid and the NBD in the ADP-state, as indicated by the higher efficiency E_{BR} , allows to monitor correlated motion between the NBD and lid, and the NBD and the SBD. Expectedly, if the interdomain distance shortens, the lid is also closer to the NBD. The distance between the lid and the NBD seems to be independent of the conformation of the lid, i.e. closed or open. Furthermore, as before the closed lid state coincides with a closer contact between the domains.

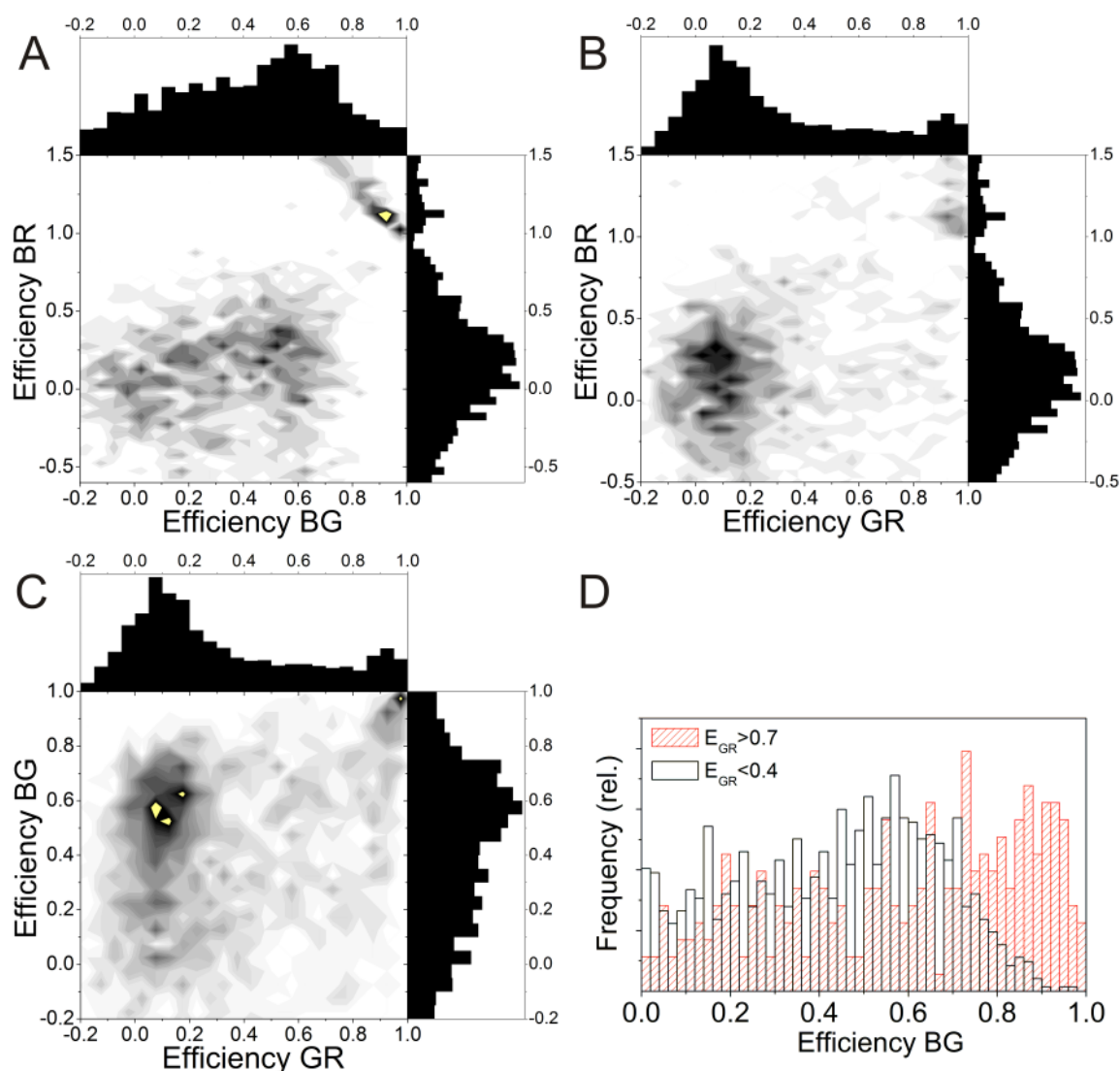


Figure 4.20: Two-dimensional efficiency plots for BiP in the presence of AMP-PNP (A-C). D: Efficiencies E_{BG} for the two populations observed in C, separated by E_{GR} .

In the ATP-bound state (figure 4.20), again correlation is observed between E_{BR} and E_{BG} . Low E_{BG} corresponds to low E_{BR} , shifting from ~ 0 at $E_{BG} < 0.2$ to 0.3 for $E_{BG} > 0.4$. No correlation is observed between E_{GR} and E_{BR} . For E_{BG} , a narrow high-FRET state is observed,

which, in this case, is solely attributed to the discussed artifact. The ATP-bound state is characterized by an open lid conformation and a smaller distance between the domains as indicated by an increase in E_{BG} in comparison to the ADP-bound state (see figure 4.22), consistent with the spFRET data. Only the expected correlation between the NBD-SBD and the NBD-lid distances is observed.

In all states, correlation is observed between E_{BR} and E_{BG} . Expectedly, if the two domains come in closer contact, also the distance between the NBD and the lid will shorten. No correlation is found for E_{BR} and E_{GR} in any of the states. In the plot E_{BG} versus E_{GR} , three states can be identified: The apo-state is characterized by high E_{GR} and a broad distribution of E_{BG} centered around 0.6. Addition of ADP reveals a second state, characterized by low E_{GR} and a shift of the broad distribution of E_{BG} to lower values centered at 0.5. Addition of ATP shifts this population to higher values of E_{BG} at ~ 0.6 . Interestingly, the closed-lid apo-state shows a similar distribution of E_{BG} as the open-lid ATP-state.

4.3.4 The conformational space of BiP

Following up on the results of the spFRET studies, the three-color FRET measurements presented here allow further investigation of the different conformational states of BiP. The discussion focuses on the interdomain sensor and the SBD-lid sensor, as given by E_{BG} and E_{GR} , respectively, as the NBD-lid sensor E_{BR} does not convey much additional information and is more difficult to interpret. Figure 4.21 shows the two-dimensional efficiency histograms for the three experimental conditions. The apo-state (green) is characterized by a closed lid and flexibility of the interdomain distance (see figure 4.18, D, for the one-dimensional histogram of E_{BG}). Additionally, opening of the lid coincides with an increase of the interdomain distance (dashed black line). In the presence of ADP, a second conformational state appears (blue), defined by an open lid and slightly increased separation of the domains (see figure 4.19, D, for a comparison of the distributions of E_{BG} of the two states). Furthermore, the ADP-state is more defined than the apo-state. The apo-state is still observed in the presence of ADP. This indicates either that BiP cycles between both states when ADP is bound (as shown for the Hsp70-chaperone Ssc1 by Sikor et al., 2013), or that BiP shows low affinity for ADP. In the presence of AMP-PNP, the apo-state is no longer populated. Rather, BiP assumes a well-defined ATP-state (red) with a closed lid and slightly closer contact between the domains. A comparison of the distributions of E_{BG} for the ADP- and the ATP-state is given in figure 4.22.

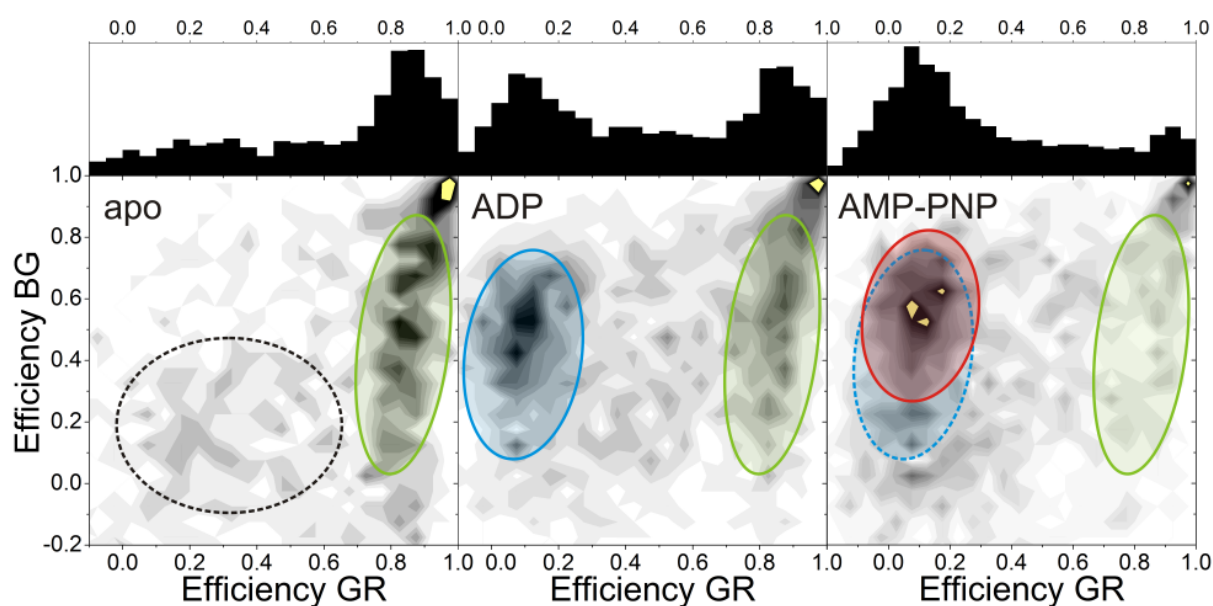


Figure 4.21: Two-dimensional efficiency histograms of E_{BG} versus E_{GR} for the the apo-, ADP- and ATP-state of BiP. Green: apo-state, blue: ADP state, red: ATP state.

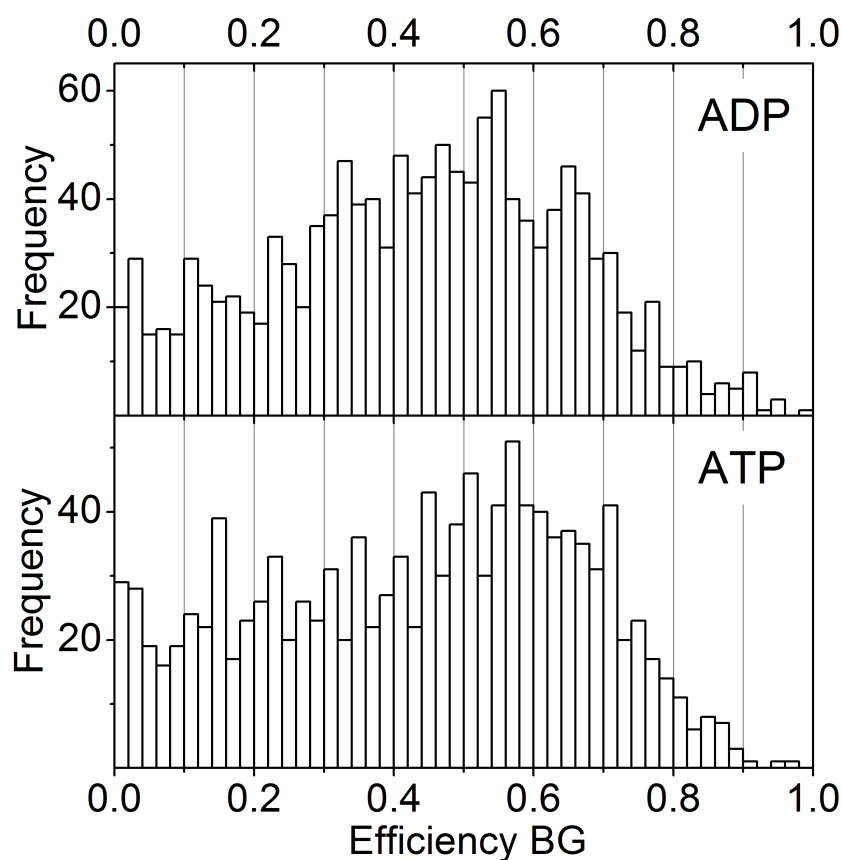


Figure 4.22: Comparison of the ADP- and ATP-state of BiP. For both histograms, selection was performed by thresholding $E_{GR} < 0.4$.

5 Conclusion and Outlook

5.1 Three-color MFD studies

The correctness of FRET efficiencies determined from three-color MFD is confirmed by comparison with efficiencies from sub-labeled species for the DNA measurements and by the reproduction of published FRET efficiency distributions by three-color FRET for the Hsp70 chaperone BiP. The discussed DNA measurements showcase that the quantity E_{BR} is prone to artifacts, especially if the number of photons detected in the channel BR is low. Apparent correlations between the three FRET efficiencies for the static DNA system are elucidated and characterized. With this knowledge, the biological relevant correlations observed for BiP are identified and the robustness of the analysis is increased.

Generally, three-color FRET experiments should be carefully designed with the application in mind. Examples for this are the two-donor one-acceptor scheme as applied by Milles et al. (2012a) or the approach by Hohng et al. (2004), where FRET from a donor dye occurs mutually exclusive to either one of two acceptor dyes. A full treatment of the three-color FRET system proves difficult. Of the two FRET efficiencies E_{BG} and E_{BR} , the former serves as a more accurate distance indicator. The large number of corrections applied to the photon counts in the red channel after blue excitation in conjunction with the already high crosstalk and direct excitation introduces uncertainty. Shot-noise broadening of the obtained efficiency distributions is severe for cases where the corrected value is close to zero, as seen for the cascade DNA. Thus, if two distances are of interest, it is recommended to use E_{GR} and E_{BG} . If three efficiencies are to be determined by three-color MFD, reasonable FRET between all dyes should be ensured to reduce this problem. Alternatively, proximity ratios or simple signal ratios can serve as more robust parameters to unspecifically monitor changes of the whole system or reveal structural heterogeneity. For the protein BiP as discussed here, biological relevant information of correlated domain motions is contained in the FRET efficiencies E_{BG} and E_{GR} , while the relative motion of the nucleotide binding domain and the lid as monitored by E_{BR} is of less interest. The artifacts discussed here for E_{BR} can thus be avoided by limiting the discussion to the relevant distances between the domains and within the substrate binding domain.

Shot-noise broadened parameter distributions can be accurately described if the statistics of photon counting are incorporated into the analysis, as is achieved by Probability Distribution Analysis (PDA, see section 5.3). A treatment of the three-color FRET system by PDA will enable a more accurate description of the underlying distance distributions based on the raw photon counts. Another approach to reduce shot-noise in MFD is to increase the observation time. This can be achieved by increasing the viscosity of the medium or by encapsulating the protein in lipid vesicles. Further information on the dynamic motions within BiP can be gathered by TIRF microscopy or confocal measurements on immobilized molecules, allowing longer observations of single molecules.

5.2 Duty-cycle optimized PIE

DCO-PIE has been implemented for the presented three-color PIE-MFD setup. The observed signal gain for the dyes discussed here is mostly related to the increase in laser intensity when applying optimized pulse sequences. Nonetheless, the application of DCO-PIE is recommended, because higher output powers for the blue lasers can be achieved for this setup. Additionally, DCO-PIE offers the possibility to adjust the duty-time of the lasers to the specific application at hand. Further studies on DCO-PIE should investigate the effects of saturation and photobleaching by means of higher laser power or by using faster saturating and less photostable dyes. The effect of photobleaching can be quantitatively studied using burst analysis by counting the number of bursts containing bleaching events at different pulse sequences (see Kong et al., 2007).

5.3 Accurate Distance Measurements by three-color MFD

Extracting accurate distance information from FRET measurements is not a trivial task. The detected FRET signal has to be corrected for crosstalk from the donor fluorophore, direct excitation of the acceptor dye by the donor excitation laser as well as differences in detection efficiencies and quantum yields of the fluorophores. Additionally, the orientation of the fluorophores can have a strong influence on the measured FRET efficiency, and precautions should always be taken. Even then, determining distances from the usual broad FRET efficiency distributions is not straight forward, as distance variations have to be distinguished from inherent shot noise broadening. The Probability Distribution Analysis (PDA), introduced by Antonik et al. (2006) and subsequently extended (Kalinin et al., 2008, 2010), overcomes this limitation by a rigorous treatment of the statistics of photon emission by means of probability distributions. This way, it is possible to extract the underlying distance distribution from an observed FRET efficiency distribution.

In two-color PDA the raw intensity ratio of donor and acceptor dye is fit by means of the apparent FRET efficiency or, if necessary, a distribution of FRET efficiencies, from which distance distributions are calculated. Extension of the theory to three colors allows the determination of three distances simultaneously. In essence, three intensity ratios are available, which are described by three apparent FRET efficiencies (or proximity ratios) representing probabilities for apparent transitions within the three dye system:

$$\epsilon_{BG,R} = \frac{F_{BG}}{F_{BB} + F_{BG}}; \quad \epsilon_{BR,G} = \frac{F_{BR}}{F_{BB} + F_R}; \quad \epsilon_{GR,B} = \frac{F_{BR}}{F_{BG} + F_{BR}}$$

Here, the subscript XY,Z means apparent transfer from X to Y in the presence of Z . Because the FRET efficiency is a ratiometric quantity, however, only two of the ratios are independent. Basically, the problem is extended from one intensity ratio/one distance to two intensity ratios/three distances. Additional information is necessary: 1) Application of PIE

allows treatment of the distance between the green and red dye by two-color PDA. 2) When labeling efficiencies are not too high, as usually the case, subpopulations with only active blue and green or blue and red dye can be separated from the triple-labeled molecules. This enables direct access to the intensity ratios in absence of the third dye and allows again treatment of these distances by two-color PDA. This approach is especially applicable if the labeling efficiency of the blue dye is close to 100% while labeling efficiencies for the other dyes are lower. Fitting of these, in total, five intensity ratio histograms by PDA while globally linking the three FRET efficiencies or distances, should enable simultaneous and accurate determination of three distances within a single molecule. The relation between apparent and correct FRET efficiencies becomes more complicated in the three-color case and certainly affects the robustness of the analysis when converting apparent FRET efficiency distributions to actual FRET efficiencies and distances. It remains to be seen if the additional information available in three-color FRET allows three-color PDA to exceed the accuracy of two-color PDA.

Two-dimensional PDA analysis for BiP

With regards to the three-color FRET data presented for the protein BiP, a first step towards a full description of the FRET system by PDA would be an analysis of the discussed two-dimensional efficiency histograms, limited to E_{BG} and E_{GR} . This way, the complexity of the system is reduced to two signal ratios, because E_{BG} is only dependent on the photon counts in the channels BB and BG, as well as the FRET efficiency E_{GR} , which is available independently by PIE. The theory for PDA can be extended to describe the two-dimensional histograms presented here, enabling a more accurate characterization of the conformational states observed for BiP.

5.4 Refinement of the burstwise lifetime fitting

As of now, the lifetime fitting algorithm is only applied to the photons in the donor channel assuming a simple mono-exponential decay. This approach works well for low and intermediate FRET efficiencies. However, if the donor is strongly quenched, the number of photons for the lifetime fitting will be low and the fit will not be accurate. A global lifetime fit of both the donor and fret channel would help in this situation. The FRET channel decay contains both the quenched donor lifetime as well as the acceptor lifetime. Thus, additionally linking the acceptor lifetime, the accuracy of the fit is increases, as shown by Kudryavtsev et al. (2012). This approach is especially necessary in the case of three-color FRET, where the blue dye is usually strongly quenched and accurate lifetime fitting is difficult. A complete time-resolved description of the photophysical system and global fitting of all six PIE channels (BB, BG, BR, GG, GR, RR) will help with this problem.

5.5 Dye choices for three-color FRET

The dyes used in this work (Atto488, Atto565 and Atto647N) have been chosen because of their fluorescent properties, that is high extinction coefficients, high quantum yield and good photostability. Especially Atto647N stands out as a dye that has an unusual high quantum yield for its spectral region. The dyes have good spectral overlap while their emission can still be well separated because their emission spectra are not too broad. Additionally, they show little to no blinking. One merit of the chosen dye/laser combination has already been discussed in detail: Raman scattering limits the detectable spectral region for the green and red dyes, so that a significant amount of signal is lost. What other dye/laser combinations are there?

In the original three-color ALEX publication Lee et al. (2007) use Alexa488, TMR and Alexa647 and excite them with 477, 532 and 633 nm lasers, respectively. Fluorescence is detected from 495-525 nm in the blue channel, from 580-620 nm in the green channel and upwards of 665 nm for the red channel. Raman scattering of the 477 nm excitation light appears in the range of 563-576 nm and is thus not an issue here. One drawback of the application of a 532 nm laser is the narrow detection band in the blue channel which only captures the lower part of the emission spectrum of Alexa488.

Lee et al. (2010b) report their realization of three-color single molecule FRET measurements both for confocal and TIRF microscopy, studying the correlated motions of the four arms of the Holliday junction. They extend the standard spFRET dye pair Cy3-Cy5, excited at 532 nm and 633 nm, respectively, by adding the near-infrared dye Cy7. With this they move away from their previous choice of Cy3-Cy5-Cy5.5 because this approach suffered from the large spectral overlap between Cy5 and Cy5.5 (Hohng et al., 2004). The new choice eliminates the problems encountered for the blue dyes, but the quantum yield for Cy7 is only 30%, while also the other dyes have relatively low quantum yield (16% for Cy3, 27% for Cy5). Since their focus is on measurements on immobilized molecules, this fact is not as crucial as it is for solution based burst analysis as described here. They do not specifically block the Raman scattering from the red laser occurring in the IR detection channel, however since the intensity of the Raman scattering is lower for higher wavelengths ($I \propto \frac{1}{\lambda^4}$) their background levels are not exceedingly high. Subsequently, they extended their dye-trio by a blue dye (Lee et al., 2010a). They discuss different choices in Cy2, Atto488 and Alexa488, whose properties are listed in table 5.1 Due to their choice for the green dye (Cy3 excited at 532 nm) they settle for Cy2 because of the three dyes it has the least spectral overlap with Cy3. Another photophysical property of blue dyes, that can be of relevance, is a photoinduced red-shift of the emission spectrum. The decision between Alexa488 and Atto488 is an issue of quantum yield versus photostability. While Alexa488 has the higher quantum yield, it is less stable with respect to bleaching. Also to consider is the fact that the emission spectrum of Alexa488 is at slightly lower wavelengths, which can be a factor if narrow emission filters are used. They detect the blue fluorescence in the range of 500-525 nm and green fluorescence from 550-610 nm. With

their blue excitation being at 473 nm the Raman peak occurs at 557-570 nm and is thus not blocked by their emission filter.

Dye	$\lambda_{\text{ex}}^{\text{max}}$ [nm]	$\lambda_{\text{em}}^{\text{max}}$ [nm]	$\epsilon(\lambda_{\text{ex}}^{\text{max}})$	QY	red shifted	Bleaching time
Cy2	489	506	150,000	0.12	5.2 %	3.8 s
Atto488	510	523	90,000	0.8	9.1 %	35.1 s
Alexa488	495	519	71,000	0.92	11.7 %	14.5 s

Table 5.1: Comparison of blue fluorophores. Extinction coefficients are given in $\text{cm}^{-1}\text{M}^{-1}$. Bleaching times are given for TIRF measurements with glucose oxidase. Data taken from Lee et al. (2010a), supporting information.

Zarrabi et al. (2009) use the fluorescent protein EGFP as the blue dye, because it can be genetically fused to a subunit of the protein (in their case the F_0F_1 -ATP synthase). They labeled a second subunit of the enzyme with Alexa532 and Cy5 and excite EGFP with a pulsed 488 nm laser and Alexa532 with an acousto-optical modulator (AOM) switched cw 532 nm laser. As expected they also encounter a large Raman scatter signal in the green channel (detected in the region 545-625 nm), which they remove by microtime gating. The detectable spectral region for the blue channel is severely limited by their excitation laser choices. In fact, they use an emission filter centered at 513 nm with a width of only 17 nm. However, due to the choice for the green and red laser, Raman scattering is not a problem and the detectable region for the red dye can be enlarged.

The lab of Philip Tinnefeld applied three-color FRET to study the correlated movement and bending of nucleic acid structures (Ross et al., 2007; Person et al., 2009). They use the same dyes as in this work and excite them with 488, 568 and 647 nm, respectively. An Ar^+Kr^+ mixed gas laser is operated in multi-line mode and the excitation wavelength is alternated by an acousto-optical tunable filter (AOTF) on the microsecond timescale in what they call triple alternating laser excitation (TrALEX). Interestingly, they note that usually the polychroic beamsplitter is limiting the achievable signal-to-noise ratio due to limited transmission ranges and broad reflective regions. They report an increase of 10%-30% for the individual detection channels by using an acousto-optical beamsplitter (AOBS) with freely definable reflective wavelengths and narrow reflection bands of < 5 nm. In fact the polychroic mirror used in this work limits the percentage of the spectra detected as seen in figure 3.5 on page 30, especially for the emission of Atto647N. The detected percentage for Atto647N is reduced by 14% due to the transmission characteristics of the dichroic, while the other two channels suffer a signal loss of about 8% with respect to amount detected if only the emission filters are considered. The Raman signal is avoided by appropriate filter choices which are similar to the solution presented in this work. The blue emission is detected in the range of 507-555 nm (here: 500-550 nm), the green emission from 604-634 nm (here: 589-625 nm) and the red emission is detected from 655-705 nm (here: 655-685 nm). The differences in filter choices are a consequence of the differences in the excitation wavelengths. For 488 nm excitation the Raman scatter occurs

at 578-592 nm (as opposed to 567-580 nm for 480 nm excitation as applied here), which is why the green fluorescence has to be collected in a higher wavelength region. Consequently, their green signal levels will be lower. For the green excitation the difference in the Raman peak is smaller (694-714 nm for 568 nm excitation versus 690-709 nm for 565 nm excitation), however the detected spectral region extends to longer wavelengths for their filter choice, up to 705 nm versus the 685 nm applied here. This has also been tested in the course of this work, but even for a filter ranging from 661-690 nm the Raman background still exceeded 5 kHz at 100 μ W green laser power. It is thus expected that background levels in the red channel after green excitation are still fairly high for them.

Milles et al. (2012a) present the first intramolecular three-color FRET study of a protein using a novel labeling strategy for specific labeling of the second acceptor dye (Milles et al., 2012b). They use the dyes Alexa488, Alexa594 and Alexa647 and excite them at 488, 570 and 660 nm, respectively, whereat they achieve pulsed excitation at 570 nm by filtering of a pulsed white light laser. Emission filters are not specified, but it is assumed that they deal with the Raman scattering in a similar fashion. Labeling of the intrinsically disordered yeast nucleoporin with a two-donor one-acceptor FRET scheme (with stochastic labeling for the two donor positions), they show that they can separate different species by stoichiometry and furthermore separate the two differently labeled donor positions by correlating the two FRET efficiencies.

All presented studies used either Alexa488, Atto488 or Cy2 as the blue dye. This dye choice, in combination with a green dye excited at 532 nm, severely limits the detectable region for the blue emission. Another option would be to use Atto425 at 445 nm excitation in combination with standard dye pairs such as Cy3-Cy5, Alexa532-Alexa647 or Atto532-Atto647N. This combinations is not limited by Raman scattering, which occurs at 520-530 nm for 445 nm excitation. However, fluorophores absorbing below 450 nm have only seldom been used in single molecule fluorescence studies, as they suffer from low absorption and higher photobleaching rates. Additionally, the background signal due to auto-fluorescence of the buffer increases markedly. A technical limitation is that the usual APDs have low sensitivity in the wavelength region below 500 nm. Fortunately, APDs optimized for this spectral region are now available.

5.6 Extension to four colors

Possibilities of four-color FRET

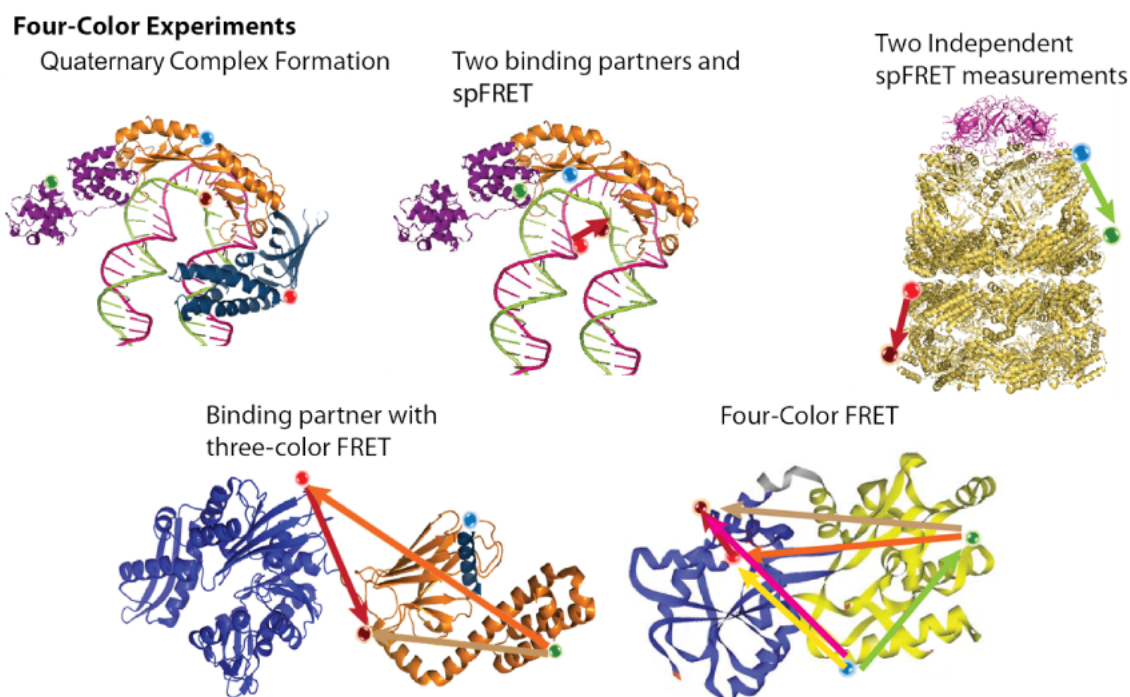


Figure 5.1: Applications for four-color FRET.

Four-color FRET enables a multitude of new experiments (see figure 5.1). The study of quaternary complex formation by labeling of each interaction partner with a different dye is possible by either FCS or by means of the stoichiometry in burst analysis. In the same manner that three-color MFD allows the observation of one distance in the presence or absence of an additional binding partner, four-color MFD opens the possibility to observe one distance with respect to the binding of two separate interaction partners, or to monitor changes of three distances at once upon binding of an interaction partner. Note that for these applications the reporter dyes should be chosen such that they don't interfere with the FRET system. Thus, the blue dye and the green dye should be used as reporters. The option to probe two separate, independent distances allows to gain insight on the correlation of movements of distant parts within a single molecule. Finally, full four-color FRET enables the simultaneous determination of six distances. For this, however, the requirements are even more stringent than for three-color FRET. The low quantum yield of near-infrared dyes increases the shot-noise of the obtained parameter distributions. As with three-color FRET, the calculation of accurate FRET efficiencies is dependent on the knowledge of FRET efficiencies of subsystems. To calculate the efficiencies from the blue dye to either of the other dyes, now the efficiencies of the three dye subsystem need to be known, which themselves are dependent on the efficiency of the red to the near-infrared dye. Additionally, the number of excitations of the blue dye are

now not only distributed on three, but on four channels, further lowering the obtained photon numbers. If the distances between the dyes are chosen poorly and the FRET efficiencies are too high, the quenching of e.g. the blue dye by a total of three acceptors will further lower the obtained number of photons. Thus, although the capabilities of full four-color FRET are tempting, experimental realization requires careful selection of the system to be studied and remains challenging.

Dye choices for four-color PIE-MFD

With the visible spectrum covered, the extension to four colors is best achieved by inclusion of a near-infrared (NIR) dye. Four-color FRET has been realized by Lee et al. (2010a) for TIRF microscopy and by Stein et al. (2011) for confocal microscopy. The instrumental realization has been discussed in detail in the previous section. The NIR dyes used are Cy7 and Alexa750, respectively. Fluorescence properties are listed for a number of dyes in table 5.2. The extinction coefficient for these dyes is usually very high ($>10^5 \text{ M}^{-1}\text{cm}^{-1}$), although this property is not a deciding factor since direct excitation will only be used to probe the presence of the dye. Three spectral regions are accessible. Atto700 and Alexa700 emit in the region from 700-750 nm. The emission of the dyes Cy7 and Alexa750 peaks in the region from 750-800 nm. Lastly, Alexa790 emits from 780-830 nm. The emission spectra of the dyes, together with the red dye used in this work (Atto647N), are shown in figure 5.2, bottom. Four factors influence the decision for a dye: 1) The crosstalk from the red dye into the IR detection channel should be minimal. 2) The direct excitation of the NIR dye by the red laser should be minimal. 3) For sensitive FRET measurements, reasonable spectral overlap between the NIR dye and all other dyes is required. 4) Raman scattering from the red laser should not be detected in the IR detection channel.

As before, large spectral overlap goes hand in hand with increased crosstalk. The excitation spectra of the discussed dyes are shown in figure 5.2, top, together with the emission spectrum of Atto647N. Expectedly, Atto700 and Alexa700 exhibit the largest spectral overlap. Indeed, the Förster radius for the pair Atto647N-Atto700 is 74 Å. However, due to the characteristics of the emission spectrum of Atto647N, which shows a long tail towards higher wavelengths, the crosstalk is very high. Additionally, direct excitation by the red laser (indicated by the dashed line at 641 nm in figure 5.2, top) is high for these dyes (48.6% for Alexa700, 39.7% for Atto700). For the dyes Cy7 and Alexa750, the spectral overlap with Atto647N is still large. The crosstalk will be minimal if emission is detected in the region from 750-800 nm. This filter choice also blocks possible Raman scattering. The direct excitation of these dyes is still not negligible, but reduced to 18.0% for Cy7 and 19.6% for Alexa750. The choice between Cy7 and Alexa750 seems to be decided by the higher quantum yield of Cy7 of 30%, as opposed to 12% for Alexa750. It is not clear why Stein et al. use Alexa750, although other properties such as blinking, photobleaching or the population of dark states may have been the deciding factor.

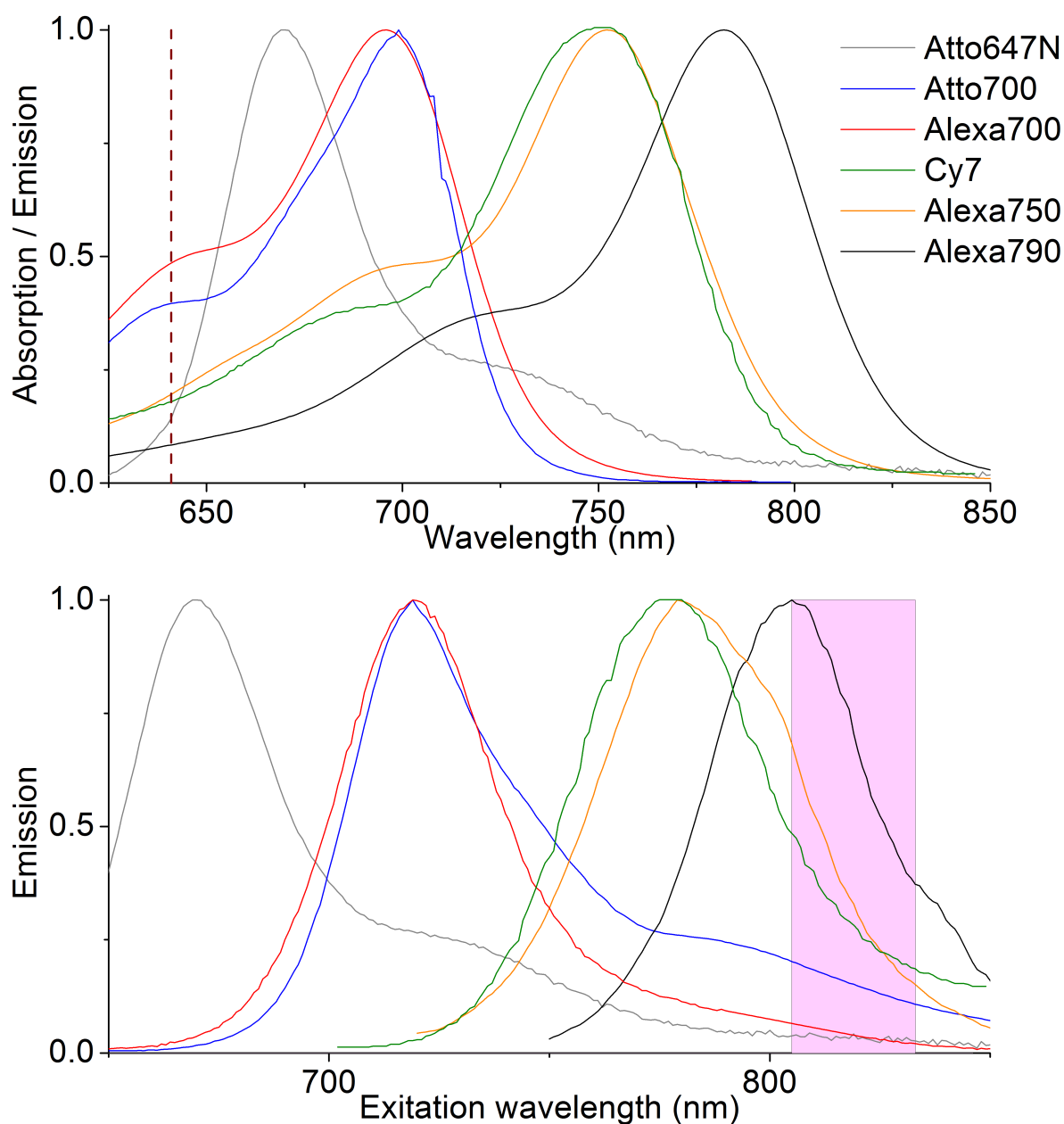


Figure 5.2: Absorption (top) and emission (bottom) spectra of near-IR dyes. Additionally, the emission spectrum of the far-red dye Atto647N is shown (gray). The dashed line in the top graph corresponds to the red excitation laser at 641 nm. The shaded region in the bottom graph indicates the Raman scattering from the red laser.

The dye Alexa790 shows the least crosstalk and direct excitation, but also has the least spectral overlap of the dyes discussed. Additionally, the Raman signal of the red laser will limit the detectable spectral region and the quantum yield of the dye is not known.

All in all, it is evident why the published four-color FRET studies used either Cy7 or Alexa750 as the NIR dye. It is proposed here to use Cy7.

Dye	τ	QY	$\epsilon(\lambda_{max}^{ex})$	λ_{max}^{em}
Atto700	1.6 ns	25%	$1.2 \cdot 10^5 \text{ M}^{-1} \text{ cm}^{-1}$	719 nm
Alexa700	1.0 ns	25%	/	719 nm
Cy7	/	30%	/	775 nm
Alexa750	0.7 ns	12%	/	779 nm
Alexa790	/	/	/	805 nm

Table 5.2: Properties of near-IR dyes for single-molecule fluorescence applications. τ : Lifetime, QY: Quantum yield, $\epsilon(\lambda_{max}^{ex})$: Maximum extinction coefficient, λ_{max}^{em} : Wavelength at maximum emission.

Extension of the setup to four colors

The extension of the presented setup for the inclusion of a NIR dye is best achieved as described here in analogy to the approach used by Stein et al. (2011). The excitation of the NIR dye can be achieved by a picosecond pulsed diode laser (e.g. LDH-P-730, PicoQuant, at 735 nm). The excitation polychroic used in this work is transmittent for IR light and has thus to be replaced. An optimal choice would be an AOBS as discussed in section 5.5. The optical path is equipped with an additional mirror after the excitation polychroic that guides the light into the microscope body. Replacement of this mirror by a dichroic mirror that is transparent for the fluorescence of the NIR dye, but reflects all excitation wavelengths (e.g. 740DCXXR, AHF Analysentechnik), leaves the detection pathway for the other three channels unaltered. The IR detection channel is then equipped with a separate pinhole and PBS. The prior separation of the IR fluorescence lowers the requirements for the excitation polychroic, which are given by a good reflectivity for the IR laser and good transmission for the spectral region of the red detection channel. Emission filters for the IR detection channel should span the spectral range from 750 to 800 nm. Although the detection efficiency of the APDs used in this work is still reasonable in this wavelength region (50-60%, see section 3.4 on page 31), optimized modules for NIR detection are also available that increase the detection efficiency to 65-75% (COUNT NIR, LaserComponents).

A Appendix

A.1 Useful relations of FRET related quantities

For sake of completeness, useful relations between FRET efficiencies, FRET efficiency related quantities and intensity ratios shall be listed here. Especially the relations between the proximity ratios and the correct FRET efficiencies can be relevant, as given by equations A.4 and A.5.

$$E_{12,3} = \frac{F_{2,1}}{(1 - E_{23})(F_{1,1} + F_{2,1} + F_{3,1})} \quad (\text{A.1})$$

$$E_{13,2} = \frac{F_{3,1} - E_{23}(F_{2,1} + F_{3,1})}{(1 - E_{23})(F_{1,1} + F_{2,1} + F_{3,1})} \quad (\text{A.2})$$

$$E_{1A} = \frac{F_{2,1} + F_{3,1}}{F_{1,1} + F_{2,1} + F_{3,1}} \quad (\text{A.3})$$

$$\epsilon_{12} = \frac{F_{2,1}}{F_{1,1} + F_{2,1}} = E_{12} \left(\frac{1 - E_{23}}{1 - E_{23}E_{12}} \right) \quad (\text{A.4})$$

$$\epsilon_{13} = \frac{F_{3,1}}{F_{1,1} + F_{3,1}} = \frac{1}{1 + \left(\frac{E_{13}}{1 - E_{13}} + E_{23} \frac{E_{12}}{1 - E_{12}} \right)^{-1}} \quad (\text{A.5})$$

$$\frac{F_{2,1}}{F_{1,1} + F_{2,1} + F_{3,1}} = (1 - E_{23})E_{12,3} \quad (\text{A.6})$$

$$\frac{F_{3,1}}{F_{1,1} + F_{2,1} + F_{3,1}} = E_{13,2} + E_{23}E_{12,3} \quad (\text{A.7})$$

$$E_{1A} = \frac{E_{12}(1 - E_{13}) + E_{13}(1 - E_{12})}{1 - E_{12}E_{13}} \quad (\text{A.8})$$

$$E_{13} = \frac{E_{13,2}}{1 - E_{12,3}} \quad (\text{A.9})$$

$$E_{12} = \frac{E_{12,3}}{1 - E_{13,2}} \quad (\text{A.10})$$

$$E_{12,3} = \frac{E_{12}(1 - E_{13})}{1 - E_{12}E_{13}} \quad (\text{A.11})$$

$$E_{13,2} = \frac{E_{13}(1 - E_{12})}{1 - E_{12}E_{13}} \quad (\text{A.12})$$

$$E_{12,3} = 1 - \frac{\tau_{D,23}}{\tau_{D,3}} \quad (\text{A.13})$$

$$E_{13,2} = 1 - \frac{\tau_{D,23}}{\tau_{D,2}} \quad (\text{A.14})$$

A.2 Correction factors for three-color PIE-MFD

A.2.1 Direct excitation and crosstalk

BR

For a blue only labeled species, the raw proximity ratio $\epsilon_{BR,raw}^{B-only}$ is given by:

$$\epsilon_{BR,raw}^{B-only} = \frac{BR^{B-only}}{BB^{B-only} + BR^{B-only}} = \left(1 + \frac{BB^{B-only}}{BR^{B-only}}\right)^{-1} \quad (\text{A.15})$$

Thus it follows:

$$\beta_{BR} = \frac{\epsilon_{BR,raw}^{B-only}}{1 - \epsilon_{BR,raw}^{B-only}} \quad (\text{A.16})$$

For a red only labeled species, the raw stoichiometry $S_{BR,raw}^{R-only}$ is given by:

$$S_{BR,raw}^{R-only} = \frac{BR^{R-only}}{BR^{R-only} + RR^{R-only}} = \left(1 + \frac{RR^{R-only}}{BR^{R-only}}\right)^{-1} \quad (\text{A.17})$$

Thus it follows:

$$\alpha_{BR} = \frac{S_{BR,raw}^{R-only}}{1 - S_{BR,raw}^{R-only}} \quad (\text{A.18})$$

BG

For a blue only labeled species, the raw proximity ratio $\epsilon_{BG,raw}^{B-only}$ is given by:

$$\epsilon_{BG,raw}^{B-only} = \frac{BG^{B-only}}{BB^{B-only} + BG^{B-only}} = \left(1 + \frac{BB^{B-only}}{BG^{B-only}}\right)^{-1} \quad (\text{A.19})$$

Thus it follows:

$$\beta_{BG} = \frac{\epsilon_{BG,raw}^{B-only}}{1 - \epsilon_{BG,raw}^{B-only}} \quad (\text{A.20})$$

For a green only labeled species one has to additionally consider the crosstalk from the green to the red channel. The raw stoichiometry $S_{BG,raw}^{R-only}$ is given by:

$$\begin{aligned}
S_{BG,raw}^{G-only} &= \frac{BG^{G-only} + \beta_{GR}BG^{G-only}}{BG^{G-only} + \beta_{GR}BG^{G-only} + GG^{G-only} + \beta_{GR}GG^{G-only}} \\
&= \frac{(1 + \beta_{GR})BG^{G-only}}{(1 + \beta_{GR})BG^{G-only} + (1 + \beta_{GR})GG^{G-only}} = \left(1 + \frac{GG^{G-only}}{BG^{G-only}}\right)^{-1} \quad (A.21)
\end{aligned}$$

Thus it follows again:

$$\alpha_{BG} = \frac{S_{BG,raw}^{G-only}}{1 - S_{BG,raw}^{G-only}} \quad (A.22)$$

A.2.2 Correction factors for the presented measurements

The correction factors for direct excitation are dependent on the applied laser powers and used pulse sequence. The correction factors used in this work are listed in table .

Sample	Pulse seq.	I_B	I_G	I_R	α_{BG}	α_{BR}	α_{GR}	β_{BG}	β_{BR}	β_{GR}
DNA2(a)	[(bg) ₂ rg] _n	93	100	67	0.11	0.08	0.193	0.11	0	0.17
DNA1	[(bg) ₃ rg] _n	115	80	100	0.14	0.10	0.16	0.10	0	0.13
DNA2(b)	[(bg) ₃ rg] _n	115	80	100	0.14	0.10	0.15	0.10	0	0.15
BiP	[(bg) ₃ rg] _n	110	80	100	0.140	0.102	0.155	0.102	0.005	0.153

Table A.1: Correction factors used in this work. Laser intensities I_X are given in μW . DNA2(a) and (b) correspond to the measurements discussed in section 3.8.4 and 4.2.2, respectively.

A.3 Two-dimensional PDA

The key quantity to be computed for two-dimensional PDA is the joint probability to observe a signal ratio $(S_{GG}/S_{GR})_i$ and a signal ratio $(S_{BB}/S_{BG})_j$ at the same time, that is $P((\frac{S_{GG}}{S_{GR}})_i \cap (\frac{S_{BB}}{S_{BG}})_j)$. Using the definition of conditional probabilities, this quantity is obtained as:

$$P((\frac{S_{GG}}{S_{GR}})_j \cap (\frac{S_{BB}}{S_{BG}})_i) = P((\frac{S_{BB}}{S_{BG}})_j | (\frac{S_{GG}}{S_{GR}})_i) P(\frac{S_{GG}}{S_{GR}})_i \quad (A.23)$$

In other words, the joint probability is given by the probability to observe a signal ratio $(S_{BB}/S_{BG})_j$ if $(S_{GG}/S_{GR})_i$ has been observed, times to probability to observe $(S_{GG}/S_{GR})_i$. $P(\frac{S_{GG}}{S_{GR}})_i$ is obtained by one-dimensional PDA as described by Antonik et al. (2006), treating the background contribution by Poissonian statistics and the FRET process by a binomial distribution with parameter ϵ_{GR} :

$$\epsilon_{GR} = 1 - \frac{1}{1 + \frac{g_R \Phi_R}{g_G \Phi_G} \left(\frac{E_{GR}}{1 - E_{GR}} \right) + \beta_{GR}} \quad (A.24)$$

Simulation of a distance distribution is then performed by assuming a distribution for the efficiency, $P(E_{GR}(R_{GR}))$, leading to a distribution of $P(\epsilon_{GR}(R_{GR}))$.

Description of the signal ratio $(S_{BB}/S_{BG})_j$ is performed analogously, whereat the apparent FRET probability ε_{BG} is now given by:

$$\varepsilon_{BG} = 1 - \frac{1}{1 + \frac{g_G \Phi_G}{g_B \Phi_B} \left(\frac{E_{BG}}{1 - E_{BG}} \right) (1 - E_{GR}) + \beta_{BG}} \quad (\text{A.25})$$

In addition to an assumed distance distribution $P(R_{BG})$, the distribution of ε_{BG} is now also dependent on the distribution $P(E_{GR})$ obtained from one-dimensional PDA: $P(\varepsilon_{BG}(R_{BG}, E_{GR}))$.

The conditional probability $P((\frac{S_{BB}}{S_{BG}})_j | (\frac{S_{GG}}{S_{GR}})_i)$ is computed as follows: The observation of a certian signal ratio $(S_{GG}/S_{GR})_i$ corresponds to a distribution of FRET efficiencies $P(E_{GR})$, that is used then used in formula A.25.

References

- Antonik, M., Felekyan, S., and Gaiduk, A. (2006). Separating structural heterogeneities from stochastic variations in fluorescence resonance energy transfer distributions via photon distribution analysis. *The Journal of Physical Chemistry B*.
- Clamme, J.P. and Deniz, A.A. (2005). Three-color single-molecule fluorescence resonance energy transfer. *ChemPhysChem*.
- Cross, P.C., Burnham, J., and Leighton, P.A. (1937). The Raman Spectrum and the Structure of Water. *J. Am. Chem. Soc.*
- Deniz, A., Laurence, T., Dahan, M., Chemla, D., Schultz, P., and Weiss, S. (2001). Ratiometric single-molecule studies of freely diffusing biomolecules. *Annual Review of Physical Chemistry*.
- Eggeling, C., Berger, S., Brand, L., Fries, J.R., Schaffer, J., Volkmer, A., and Seidel, C.A. (2001). Data registration and selective single-molecule analysis using multi-parameter fluorescence detection. *Journal of Biotechnology*.
- Eggeling, C., Widengren, J., Brand, L., Schaffer, J., Felekyan, S., and Seidel, C.A. (2006). Analysis of Photobleaching in Single-Molecule Multicolor Excitation and Förster Resonance Energy Transfer Measurements. *The Journal of Physical Chemistry A*.
- Enderlein, J., Robbins, D., and Ambrose, W. (1997). The statistics of single molecule detection: an overview. *Bioimaging*.
- Ernst, S., Düser, M., and Zarrabi, N. (2012a). Monitoring transient elastic energy storage within the rotary motors of single FoF1-ATP synthase by DCO-ALEX FRET. *SPIE*.
- Ernst, S., Düser, M.G., Zarrabi, N., and Börsch, M. (2012b). Three-color Foerster resonance energy transfer within single FOF1-ATP synthases: monitoring elastic deformations of the rotary double motor in real time. *Journal of Biomedical Optics*.
- ExcelitasTechnologies (2005). SPCM-AQRH Single Photon Counting Module. URL http://www.excelitas.com/Downloads/DTS_SPCM-AQRH.pdf.
- Förster, T. (1948). Zwischenmolekulare Energiewanderung und Fluoreszenz. *Annalen der Physik*.
- Fries, J., Br, L., Eggeling, C., Köllner, and Seidel, C. (1998). Quantitative Identification of Different Single Molecules by Selective Time-Resolved Confocal Fluorescence Spectroscopy. *The Journal of Physical Chemistry A*.

- Galperin, E., Verkhusha, V., Alex, and Sorkin, e. (2004). Three-chromophore FRET microscopy to analyze multiprotein interactions in living cells. *Nature Methods*.
- Gansen, A., Valeri, A., Hauger, F., Felekyan, S., Kalinin, S., Toth, K., Langowski, J., and Seidel, C.A. (2009). Nucleosome disassembly intermediates characterized by single-molecule FRET. *PNAS*.
- Gregor, I., Patra, D., and Enderlein, J. (2005). Optical saturation in fluorescence correlation spectroscopy under continuous-wave and pulsed excitation. *ChemPhysChem*.
- Ha, T., Enderle, T., Ogletree, D.F., Chemla, D.S., Selvin, P.R., and Weiss, S. (1996). Probing the interaction between two single molecules: fluorescence resonance energy transfer between a single donor and a single acceptor. *PNAS*.
- Haustein, E., Jahnz, M., and Schwille, P. (2003). Triple FRET: A tool for Studying Long-Range Molecular Interactions. *ChemPhysChem*.
- Heilemann, M., Tinnefeld, P., Mosteiro, G.S., Parajo, M.G., van Hulst, N.F., and Sauer, M. (2004). Multistep energy transfer in single molecular photonic wires. *J. Am. Chem. Soc.*
- Heinze, K.G., Jahnz, M., and Schwille, P. (2004). Triple-Color Coincidence Analysis: One Step Further in Following Higher Order Molecular Complex Formation. *Biophysical Journal*.
- Hendrix, J. and Lamb, D.C. (2013). *Pulsed Interleaved Excitation: Principles and Applications*.
- Hohng, S., Joo, C., and Ha, T. (2004). Single-Molecule Three-Color FRET. *Biophysical Journal*.
- Kalinin, S., Felekyan, S., Valeri, A., and Seidel, C.A. (2008). Characterizing Multiple Molecular States in Single-Molecule Multiparameter Fluorescence Detection by Probability Distribution Analysis. *The Journal of Physical Chemistry B*.
- Kalinin, S., Valeri, A., Antonik, M., Felekyan, S., and Seidel, C.A. (2010). Detection of Structural Dynamics by FRET: A Photon Distribution and Fluorescence Lifetime Analysis of Systems with Multiple States. *The Journal of Physical Chemistry B*.
- Kapanidis, A.N., Laurence, T.A., Lee, N.K., Margeat, E., Kong, X., and Weiss, S. (2005). Alternating-Laser Excitation of Single Molecules. *Accounts of Chemical Research*.
- Kapanidis, A.N., Lee, N.K., Laurence, T.A., Doose, S., Margeat, E., and Weiss, S. (2004). Fluorescence-aided molecule sorting: analysis of structure and interactions by alternating-laser excitation of single molecules. *PNAS*.

- Kong, X., Nir, E., Hamadani, K., and Weiss, S. (2007). Photobleaching Pathways in Single-Molecule FRET Experiments. *Journal of the American Chemical Society*.
- Koshioka, M., Sasaki, K., and Masuhara, H. (1995). Time-dependent fluorescence depolarization analysis in three-dimensional microspectroscopy. *Applied spectroscopy*.
- Kudryavtsev, V., Sikor, M., Kalinin, S., Mokranjac, D., Seidel, C.A., and Lamb, D.C. (2012). Combining MFD and PIE for Accurate Single-Pair Förster Resonance Energy Transfer Measurements. *ChemPhysChem*.
- Lakowicz, J. (2009). *Principles of fluorescence spectroscopy*.
- LaserComponents (2013). Single Photon Counting Module COUNTblue-Series. URL http://www.lasercomponents.com/fileadmin/user_upload/home/Datasheets/lcp/count-blue-series.pdf.
- Lee, J., Lee, S., Rangunathan, K., Joo, C., Ha, T., and Hohng, S. (2010a). Single-Molecule Four-Color FRET. *Angewandte Chemie International Edition*.
- Lee, N.K., Kapanidis, A.N., Koh, H.R., Korlann, Y., Ho, S.O., Kim, Y., Gassman, N., Kim, S.K., and Weiss, S. (2007). Three-Color Alternating-Laser Excitation of Single Molecules: Monitoring Multiple Interactions and Distances. *Biophysical Journal*.
- Lee, N.K., Kapanidis, A.N., Wang, Y., Michalet, X., Mukhopadhyay, J., Ebright, R.H., and Weiss, S. (2005). Accurate FRET Measurements within Single Diffusing Biomolecules Using Alternating-Laser Excitation. *Biophysical Journal*.
- Lee, S., Lee, J., and Hohng, S. (2010b). Single-Molecule Three-Color FRET with Both Negligible Spectral Overlap and Long Observation Time. *PloS one*.
- Liu, J. and Lu, Y. (2002). FRET Study of a Trifluorophore-Labeled DNAzyme. *Journal of the American Chemical Society*.
- Magde, D., Elson, E., and Webb, W.W. (1972). Thermodynamic Fluctuations in a Reacting System -Measurement by Fluorescence Correlation Spectroscopy. *Physical Review Letters*.
- Marcinowski, M., Höller, M., Feige, M.J., Baerend, D., Lamb, D.C., and Buchner, J. (2011). Substrate discrimination of the chaperone BiP by autonomous and cochaperone-regulated conformational transitions. *Nature Structural & Molecular Biology*.
- Maus, M., Cotlet, M., Hofkens, J., Gensch, T., de Schryver, F.C., Schaffer, J., and Seidel, C.A. (2001). An Experimental Comparison of the Maximum Likelihood Estimation and Nonlinear Least-Squares Fluorescence Lifetime Analysis of Single Molecules. *Analytical chemistry*.

- Milles, S., Koehler, C., Gambin, Y., Deniz, A.A., and Lemke, E.A. (2012a). Intramolecular three-colour single pair FRET of intrinsically disordered proteins with increased dynamic range. *Molecular BioSystems*.
- Milles, S., Tyagi, S., Banterle, N., Koehler, C., VanDelinder, V., Plass, T., Neal, A.P., and Lemke, E.A. (2012b). Click Strategies for Single-Molecule Protein Fluorescence. *Journal of the American Chemical Society*.
- Minsky, M. (1957). MICROSCOPY APPARATUS.
- Müller, B.K., Zaychikov, E., Bräuchle, C., and Lamb, D.C. (2005). Pulsed Interleaved Excitation. *Biophysical Journal*.
- Nir, E., Michalet, X., Hamadani, K.M., Laurence, T.A., Neuhauser, D., Kovchegov, Y., and Weiss, S. (2006). Shot-Noise Limited Single-Molecule FRET Histograms: Comparison between Theory and Experiments. *The Journal of Physical Chemistry B*.
- PerkinElmer (2005). SPCM-AQR Single Photon Counting Module. URL <http://www.scitecinstruments.pl/detektory/pcm/pdf/SPCMAQR.pdf>.
- Person, B., Stein, I.H., Steinhauer, C., Vogelsang, J., and Tinnefeld, P. (2009). Correlated Movement and Bending of Nucleic Acid Structures Visualized by Multicolor Single-Molecule Spectroscopy. *ChemPhysChem*.
- Ramirez-Carrozzi, V. and Kerppola, T. (2001). Gel-Based Fluorescence Resonance Energy Transfer (gelFRET) Analysis of Nucleoprotein Complex Architecture. *Methods*.
- Ross, J., Buschkamp, P., Fetting, D., Donnermeyer, A., Roth, C.M., and Tinnefeld, P. (2007). Multicolor Single-Molecule Spectroscopy with Alternating Laser Excitation for the Investigation of Interactions and Dynamics. *The Journal of Physical Chemistry B*.
- Schaffer, J., Volkmer, A., Eggeling, C., Subramaniam, V., Striker, G., and Seidel, C.A. (1999). Identification of Single Molecules in Aqueous Solution by Time-Resolved Fluorescence Anisotropy. *The Journal of Physical Chemistry A*.
- Schuler, B., Lipman, E.A., Steinbach, P.J., Kumke, M., and Eaton, W.A. (2005). Polyproline and the "spectroscopic ruler" revisited with single-molecule fluorescence. *PNAS*.
- Sikor, M., Mapa, K., Voithenberg, L.V., Mokranjac, D., Lamb, D.C., and von Voithenberg, L.V. (2013). Real-time observation of the conformational dynamics of mitochondrial Hsp70 by spFRET. *The EMBO Journal*.
- Stein, I., Steinhauer, C., and Tinnefeld, P. (2011). Single-molecule four-color FRET visualizes energy-transfer paths on DNA origami. *Journal of the American Chemical Society*.

- Stryer, L. and Haugland, R. (1967). Energy transfer: a spectroscopic ruler. In *PNAS*.
- Tomov, T.E., Tsukanov, R., Masoud, R., Liber, M., Plavner, N., and Nir, E. (2012). Disentangling Subpopulations in Single-Molecule FRET and ALEX Experiments with Photon Distribution Analysis. *Biophysical Journal*.
- Tyagi, S. and Lemke, E. (2013). Genetically encoded click chemistry for single-molecule FRET of proteins. *Laboratory Methods in Cell Biology - Imaging*.
- Uphoff, S., Holden, S.J., Le Reste, L.L., Periz, J., van de Linde, S., Heilemann, M., Kapanidis, A.N., and Le Reste, L.L. (2010). Monitoring multiple distances within a single molecule using switchable FRET. *Nature Methods*.
- Watrob, H.M., Pan, C.P., and Barkley, M.D. (2003). Two-Step FRET as a Structural Tool. *Journal of the American Chemical Society*.
- Widengren, J., Kudryavtsev, V., Antonik, M., Berger, S., Gerken, M., and Seidel, C.A. (2006). Single-Molecule Detection and Identification of Multiple Species by Multiparameter Fluorescence Detection. *Analytical chemistry*.
- Wikipedia (2013). Frank-Condon principle. URL http://en.wikipedia.org/wiki/Franck-Condon_principle.
- Wobma, H.M., Blades, M.L., Grekova, E., McGuire, D.L., Chen, K., Chan, W.C., and Cramb, D.T. (2012). The development of direct multicolour fluorescence cross-correlation spectroscopy: towards a new tool for tracking complex biomolecular events in real-time. *Physical Chemistry Chemical Physics*.
- Zander, C., Sauer, M., Drexhage, K., Ko, D., and Schulz, A. (1996). Detection and characterization of single molecules in aqueous solution. *Applied Physics B*.
- Zarrabi, N., Ernst, S., and Düser, M. (2009). Simultaneous monitoring of the two coupled motors of a single FOF1-ATP synthase by three-color FRET using duty cycle-optimized triple-ALEX. *SPIE*.

Acknowledgments

This work would not have been possible if it weren't for a lot of people. I would like to thank everybody that supported me in reaching this point.

First and foremost, I thank Prof. Don C. Lamb for giving me the opportunity to work in his lab, for his advice and trust and for always having an open ear, even if things get busy.

I thank Prof. Jens Michaelis for getting me interested in the field of single-molecule spectroscopy in the first place, and specifically for agreeing to grade this work as second corrector.

I thank Jelle Hendrix, PhD, for countless interesting, sometimes nonsensical, but almost always fruitful discussions. Thanks for all the help, advice and experience you gave me, and for keeping your temper when I screwed up (that one time).

Waldi, thank you for all the theoretical discussions and programming help, and for the practical help in assembling the setup.

Lena, thank you for all the hard work in labeling of the protein BiP and for performing the corresponding measurements.

Niko, thank you for helping me out with all kinds of stuff in the beginning and specifically for your help and advice in building the setup.

Wolfi, thank you for the nice time during my bachelor's thesis, and the ongoing help and cooperation throughout my master's thesis. It is much appreciated that I could build upon your well-done programs for data analysis.

I thank all the people in the groups of Prof. Lamb and Prof. Bräuchle for creating a pleasant, relaxed and productive work environment and for all the fun times inside and outside the lab. Thanks especially to the boulder crew for providing much needed balance after a long day of work.

Finally, I would like to thank my parents. Without their support none of this would have been possible.

Abbreviations

2CDE	Two-Channel Kernel-Density Estimator
AL	Achromatic Lens
ALEX	Alternating Laser Excitation
AMP-PNP	Adenylyl imidodiphosphate
AOBS	Accousto-Optical Beamsplitter
AOM	Acousto-Optical Modulator
AOTF	Acousto-Optical Tunable Filter
APBS	All-Photon Burst Search
APD	Avalanche Photodiode
ATP	Adenosine Triphosphate
BiP	Binding Immunoglobulin Protein
cw	continuous-wave
DCBS	Dual-Channel Burst Search
DCO-ALEX	Duty-Cycle Optimized Alternating Laser Excitation
DM	Dichroic Mirror
DNA	Deoxyribonucleic Acid
EF	Emission Filter
EGFP	Enhanced Green Fluorescent Protein
FCCS	Fluorescence Cross-Correlation Spectroscopy
FCS	Fluorescence Correlation Spectroscopy
FRET	Förster Resonance Energy Transfer
FWHM	Full-Width at Half Maximum
Hsp70	Heat Shock Protein 70
MFD	Multiparameter Fluorescence Detection

NA	Numerical Apertur
NIM	Nuclear Instrumentation Module
NIR	Near-Infrared
OD	Optical Density
PBS	Polarizing Beamsplitter
PDA	Probability Distribution Analysis
PIE	Pulsed-Interleaved Excitation
PM	Polychroic Mirror
PSF	Point-Spread Function
QY	Quantum Yield
SM	Single-Molecule
SMF	Single-Mode Fiber
spFRET	Single-Pair Förster Resonance Energy Transfer
TAC	Time-to-Amplitude Converter
TCBS	Triple-Channel Burst Search
TCSPC	Time-Correlated Single Photon Counting
TIRFM	Total Internal Reflection Fluorescence Microscopy
TTL	Transistor-Transistor Logic